AEROELASTIC MODELING AND FLUTTER CONTROL IN AIRCRAFT WITH LOW ASPECT RATIO COMPOSITE WINGS

by

Russell A. Morris

Dissertation submitted to the faculty of the
Virginia Polytechnic Institute and State University
in partial fulfillment of the requirements for the degree of

Doctor of Philosophy
in
Engineering Mechanics

APPROVED:

L. Meirovitch
Dr. L. Meirovitch, Chairman

Scott L. Hendricks
Dr. S. Hendricks

H. VanLandingham
Dr. H. VanLandingham

S. Thangjitham
Dr. S. Thangjitham

L. Librescu
Dr. L. Librescu

September 19, 1996
Blacksburg, Virginia

Keywords: Aeroelasticity, Flutter, Active Control, Piezoelectric

AEROELASTIC MODELING AND FLUTTER CONTROL IN AIRCRAFT WITH LOW ASPECT RATIO COMPOSITE WINGS

by

Russell A. Morris

Dr. L. Meirovitch, Committee Chairman
Department of Engineering Science and Mechanics

(ABSTRACT)

A comprehensive study including modeling and control of aeroelastic instabilities in free flying aircraft with flexible wings has been completed. The structural model of the wing consists of a trapezoidal composite plate rigidly attached to a fuselage with rigid-body degrees of freedom. Both quasi-steady and quasi-static aerodynamic strip theories were used to analyze several different flutter mechanisms for a variety of low aspect ratio wing configurations. The most critical flutter mechanism was found to be body-freedom flutter, a coupling of aircraft pitching and wing bending motions, for wings in a forward-sweep configuration. In addition, a modal approximation to the flutter eigenvalue problem was used to substantially reduce computation cost, making the resulting model very attractive for use in larger multiobjective design packages.

Composite ply angle tailoring was investigated as a passive method of increasing the body-freedom flutter airspeed of an aircraft model. In addition, wing mounted piezoelectric sensor and induced-strain actuator patches were used in conjunction with active feedback control laws to increase the airspeed at which body-freedom flutter occurs. Two control laws were tested, coupled and independent modal position feedback, to delay frequency coalescence and thus increase the flutter airspeed.

ACKNOWLEDGMENTS

The author would like to express his sincere appreciation for the guidance and leadership provided by his advisor and graduate committee chairman, Dr. Leonard Meirovitch. Our many discussions provided invaluable insight into the technical challenges faced throughout this research. Thanks are due also to the distinguished members of his graduate advisory committee, Dr. Scott Hendricks, Dr. Liviu Librescu, Dr. Surot Thangjitham and Dr. Hugh VanLandingham for overseeing this project from start to conclusion. He has learned a great deal from them, both in the classroom and through informal discussions. Finally, the author would like to thank his wife, Christina Morris, and parents, Bonnie and Wayne Morris, for their continued support and encouragement throughout his academic career. Without their love and support, none of this would have been possible.

TABLE OF CONTENTS

LIST OF FIGURES

LIST OF TABLES

CHAPTER 1

LITERATURE SURVEY AND MODELING DECISIONS

1.1 Introduction

Aeroelasticity is the study of the dynamic interaction between elastic restoring forces, inertial forces and aerodynamic loading of a particular system. In the case of aircraft wings constructed of materials with inherent flexibility, the potential exists for interaction of aerodynamic, inertial and elastic forces in an adverse manner. At certain airspeeds it is possible for a vibrating flexible wing to begin extracting energy from the surrounding airflow, thus creating an unstable condition in which the wing oscillations grow without bounds. Such self-excited oscillation is known as flutter, and the airspeed at which it occurs is referred to as the flutter airspeed. If an aircraft is flown at or above the flutter airspeed, the results are usually catastrophic, including severe damage or destruction of the aircraft and very often pilot fatality.

There are many applications other than aircraft design in which aeroelastic effects are paramount. In nature, insects, birds and fish all make beneficial use of their inherent flexibility in order to fly or swim efficiently. Also, in the field of civil engineering, aeroelastic effects such as wind loading on buildings and bridges must be taken into account during structural design as demonstrated by the collapse of the Tacoma Narrows bridge in 1940. Unstable interaction between wind loading and the vibration of the bridge caused the oscillations to grow until the structure was eventually torn apart. The bridge destruction, captured on film, is a good example of the type of phenomena that can destroy an aircraft wing or empennage during flight.

1.2 Historical Discussion of Flutter

The effects of elastic materials used to build aircraft structures have influenced the design and evolution of aircraft ever since the very first experiments with flight. In early experiments with wooden propellers, Orville and Wilbur Wright noticed that the flexible shaft tended to twist in an effort to partially unload itself. As a result, the performance of the propellers in flight did not agree well with their calculations (Ref. 2).

Although it was not realized at the time, aeroelastic phenomena were probably responsible for the destruction of Samuel P. Langley's monoplane, the aerodrome, nine days before the historical first powered flight of the Wright brothers (Ref. 3). The rear wing and tail of the monoplane collapsed during launch from a houseboat on the Potomac river. The general consensus is that the failure can be attributed to wing torsional divergence, a special case of flutter which occurs at zero frequency. Thus, it seems that aeroelastic problems have been plaguing designers since and even before the first recorded powered flight.

One of the main factors driving both early and present aircraft design is the desire for faster, lighter and more maneuverable aircraft. Naturally, both world wars provided a great impetus for vast improvements in both speed and maneuverability. During World War I, many aircraft structural failures on both sides occurred as a result of aeroelastic instabilities. Biplanes including the Haviland DH-9 and Handley Page 0/400 on the British side and the German Albatross D-III experienced violent vibrations and wing twisting during high speed dives, often resulting in wings being torn from the aircraft structure and pilot death (Ref. 2). Germany's Baron Manfred von Richtofen, "The Red Baron," was reportedly one of the few pilots to successfully land after large cracks had

formed in the lower wing. In civil aviation, the great air races during the period between the wars provided a testing ground for aircraft designs. As a result some of the best documented flutter occurrences came from these trials, where pilots typically pushed their aircraft to the limits of the flight envelope. During the 1924 Pulitzer race in Dayton, Ohio, the Army Curtis R-6 monoplane developed sudden vibrations and then lost both wings during a high speed dive, killing the pilot (Ref. 2). In 1925, during a practice flight for the International Schneider Marine Trophy race, a British Supermarine S-4 experienced wing flutter and crashed into the Chesapeake Bay. The pilot said later that just before the crash the wings began to "flutter like a moth's wings" (Ref. 2). A 1936 report by the British Aeronautical Research Committee (ARC) Accidents Subcommittee detailed more than fifty separate accidents involving wing, aileron and rudder flutter (Ref. 4). Likewise, Ref. 2 lists eleven documented flutter problems in U.S. military and civil aircraft during 1932 - 1934, while a 1956 survey by the NACA Subcommittee on Vibration and Flutter documented a total of fifty-four flutter difficulties experienced by military aircraft during the ten years following World War II (Ref. 5).

Progress in aircraft engine design, in particular the development of jet engines, pushed aircraft design quickly towards the supersonic flight regime. Typical wing designs for supersonic flight were low aspect ratio, slender swept wings. The resulting wing structures had a high degree of flexibility which together with the increased aerodynamic loads and frictional heating compounded the potential for aeroelastic problems (Refs. 6,7).

Clearly, aeroelastic instabilities have plagued designers and pilots of all types of flight vehicles. The severity of these occurrences prompted a great deal

of research into ways of either eliminating flutter or, at the very least, increasing the airspeed at which it occurs. We now turn to a discussion of techniques used in the past to control flutter.

1.3 Passive Flutter Suppression

All of the early "cures" for flutter were passive, often *ad hoc* in nature, generally involving redesign for increased wing stiffness. In his early studies of tail flutter in the HP 0/400 and DH-9 aircraft, British aeroelastician, F. W. Lanchester, suggested increasing the torsional stiffness of the connection between the aircraft's right and left elevators (Ref. 2). Many of the early design manuals simply listed minimum stiffness requirements for the avoidance of instabilities. In 1923, the concept of *mass-balancing* was introduced for aileron flutter suppression (Ref. 8). A mass was added to the aileron in an effort to lower the frequency of vibration and thus avoid flutter, which in this case involved interaction of wing bending and aileron motion. The concept of mode decoupling was applied again in 1927 by Zahm and Bear to the problem of tail flutter in a US Navy MO-1 aircraft (Ref. 9). The instability in this aircraft was traced to coupling of the bending and torsion degrees of freedom, bending-torsion flutter, in the tail sections. The recommended solution to the problem included increased torsional stiffness in an attempt to decouple the bending and torsional modes.

1.4 Active Flutter Suppression

Passive concepts of increasing wing stiffness or adding mass ballast to a wing in order to increase the flutter speed are not desirable solutions as they tend to offset the goal of minimum weight design necessary for fuel economy and efficiency. Active control theory offers the possibility of altering the

dynamic characteristics of a wing without significant increase in structural weight. Also, controls may be applied to different configurations or flight regimes simply by reprogramming the control law. For these reasons, the emphasis has shifted from the early passive methods to the use of active controls for flutter suppression.

A large percentage of work using active controls to avoid wing flutter involved the use of hydraulic actuators to drive wing lifting surfaces such as ailerons or flaperons. The earliest successful flight test of an active flutter suppression system occurred in 1972 when engineers at Boeing in Wichita, Kansas flew a control configured B-52 test aircraft 10 knots above its open-loop flutter speed (Ref. 10). The control design was based on classical theory, utilizing a combination of accelerometer measurements and feedback filters to drive outboard ailerons. The primary goal in the filter design was to increase damping in the wing bending and torsion modes, thus delaying the onset of bending-torsion flutter to higher airspeeds. Shortly after this historic accomplishment, similar results were reported for bending-torsion flutter control systems on another commercial transport, the Lockheed L-1011 (Ref. 11), as well as a German Air Force F4-F (Ref. 14) and a scale model of the U.S. Air Force YF-17 aircraft (Ref. 15). The latter two studies included not only bending and torsional modes, but also effects of external wing stores such as engines, fuel tanks and ordinance.

Control law design methodology ranges from classical theory, relying essentially on trial and error, to modern optimal control, in which a control law is derived systematically through minimization of a cost function. Many examples of both types of control designs for flutter suppression are readily available in

the literature (Refs. 10-31). One common theme in nearly all designs to date is the use of conventional control surfaces to alter the aerodynamic loads acting on the wing, thus avoiding unstable interaction between the structure and the airstream.

References 16 through 25 represent the first major analytical and experimental studies of active flutter suppression. All of these papers represent control law designs for flutter suppression on a wind tunnel model of NASA's Drones for Aerodynamic Testing (DAST) wing. Important characteristics of the wing, which was designed to exhibit bending-torsion flutter within the operational limits of the NASA Langley Transonic Dynamics wind tunnel, include aft sweep, a thin supercritical airfoil, moderate aspect ratio and hydraulically activated leading edge (LE) and trailing edge (TE) control surfaces. A wide variety of flutter control laws were synthesized and compared for the DAST wing. Nissim (Ref. 17) developed a control scheme known as the *aerodynamic energy method*, in which a feedback control law was used to suppress flutter in conjunction with a separate optimization procedure for minimizing control surface activity. An analytical comparison of two such control laws, one using only TE control surfaces and one using both LE and TE control surfaces, is made in Ref. 17. Among the results presented in this paper is the indication that the LE control surface could become unstable at high frequencies.

Modern optimal control methods were also used to design flutter suppression systems for the DAST wing. Newsom (Ref. 18) used Linear Quadratic Regulator (LQR) theory to design a full state feedback flutter control law. Minimization of a quadratic cost function allowed penalties to be placed on the amount of control surface activity. Mahesh *et al.* (Ref. 19) developed two full-

state feedback designs based on Linear Quadratic Gaussian (LQG) theory, using an input noise adjustment procedure in an effort to improve the resulting controller robustness. Both of the aforementioned optimal control designs resulted in controllers of the same high order as the original wing model and were too complex to be implemented with flight computers in the late 1970's. Mukhopadhyay, Newsom, and Abel (Refs. 20-22) extended the LQG approach to the design of reduced-order optimal controllers.

Analytical and experimental comparisons of the optimal control method of Newsom (Ref. 18) and the aerodynamic energy method of Nissim are presented in Refs. 23 and 24. Analytically, both control methods predicted a 44% increase in the flutter dynamic pressure over the open-loop value. However, in the wind tunnel the maximum increases in dynamic pressure were 35% and 27% for the optimal control law and the energy control law, respectively (Ref. 24). The main problem encountered during the experimental tests was excessive control surface activity. With the optimal control law in effect the control surfaces reached maximum deflection, resulting in system instability, before the expected 44% increase was achieved. With the aerodynamic energy control law, the problem was excessive control surface deflection rates. Classical control results for the same wing generally predict larger amounts of control surface activity than both the optimal control and aerodynamic energy methods (Ref. 16).

In 1985 a second major analytical and experimental study, known as the Active Flexible Wing (AFW) program, was undertaken jointly by Rockwell International, NASA and the U. S. Air Force (Refs. 26-31). The main goal of the AFW program was to demonstrate possible weight savings of a highly flexible

wing configuration, while offsetting the detrimental effects on aeroelastic performance through the use of active controls for flutter suppression and gust load alleviation. The AFW model was a scaled wind tunnel model of an advanced fighter configuration, with thin, low aspect ratio, swept-back wings equipped with LE and TE control surfaces. The wings were designed to exhibit classical bending-torsion flutter within the range of dynamic pressures of the NASA-Langley Transonic Dynamics Tunnel.

Four teams of engineers designed flutter suppression control laws for the AFW model with the goal of increasing the lowest open-loop flutter dynamic pressure by 30% subject to constraints on control surface deflections and rates. These control laws included: a reduced-order LQG design based on techniques developed during the DAST program (Ref. 28), a classical pole/zero design, relying mainly on root-locus and Nyquist analysis (Ref. 29), a multi-input, multi-output (MIMO) design developed using a constrained optimization routine (Ref. 30) and a classical design with strain gauge feedback instead of accelerometer measurements used in the previous three designs (Ref. 31). Wind tunnel tests of all four control laws demonstrated maximum increases in the flutter dynamic pressure ranging from 17% to 23%. As in the DAST program, the increases in dynamic pressure achieved experimentally were limited by excessive dynamic response of the wing surfaces (Ref. 26).

1.5 Swept Wing Aircraft

With the advent of flight at high subsonic, transonic and supersonic speeds, aircraft designers began to investigate wings with low thickness ratios and either forward or aft sweep, both of which help reduce the adverse drag effects of compressibility. Unfortunately, added flexibility and sweep tend to

increase the significance of aeroelastic effects such as divergence and flutter. Diederick and Budiansky (Ref. 32) reported on the drastic drop in divergence speed associated with forward sweep angles. They demonstrated that increasing forward sweep from 0 to 28 degrees can reduce the divergence speed by as much as 90%.

The low divergence speed associated with forward-swept wings is due to *wash-in*, an increase in the effective angle of attack due to adverse bending-torsion coupling (Ref. 33). Wash-in leads to higher aerodynamic loading on the wing and large deflections at low airspeeds, thus a low divergence speed. The opposite effect, *wash-out*, occurs on aft-swept wings, reducing the effective angle of attack, attenuating the aerodynamic loading and delaying the onset of divergence to higher airspeeds.

Forward-swept wings offer many advantages over their aft-swept counterparts, including (Refs. 35 & 36):

- Significantly Higher Maneuver Lift-to-Drag Ratios
- Lower Trim Drag resulting in increased supersonic range
- Lower Stall Speed resulting in slower landings
- Better Low-Speed Handling
- Reduced Wave Drag

Despite these advantages, the severe divergence problems associated with forward sweep virtually eliminated the possibility of utilizing forward-swept metallic wings in practice. Prior to the mid-1970's the only feasible way to increase the divergence speed of a wing was through increased torsional stiffness, implying increased structural weight. With the advent of modern filamentary composite materials it became possible to alter the aeroelastic properties of wing structures without a significant weight penalty Composite materials have lower specific weights and higher specific strengths than

conventional metallic aircraft materials. In addition, composite structures have directional stiffness properties that may be tailored to meet specific loading conditions. Krone (Ref. 34) was the first to demonstrate that proper fiber orientation and laminate thickness distribution could be used to reduce the wash-in effect on a forward-swept composite wing.

Following Krone's initial paper on the subject, a great deal of research was carried out with the goal of determining proper orientation angles for increased divergence speed of forward-swept wings (Refs. 37-40). This practice, known as aeroelastic tailoring, cleared the way for practical forward-swept wing designs. Wind-tunnel testing verified that lightweight forward-swept wing designs were feasible (Refs. 41-44). Excellent surveys on aeroelastic tailoring for divergence suppression are presented in Refs. 40 and 42.

Flutter of composite wings was investigated for straight wings by Hollowell and Dugundji (Ref. 43) and for swept designs by Lottati (Ref. 44). Both models were cantilever wings which exhibited divergence and classical bending-torsion flutter. Lottati demonstrated analytically and experimentally that aeroelastic tailoring for increased divergence speed may actually cause a decrease in the flutter speed, implying that divergence may not be the critical instability for certain wing configurations.

1.6 Body-Freedom Flutter

With forward-swept wing divergence problems apparently solved, attention shifted to modeling a free-flying forward-swept wing aircraft. In actual flight a wing is not fixed in space, but instead fixed to a fuselage free to undergo rigid-body motions, such as pitch (rotation about the center of mass) and plunge (translation in the vertical direction). The importance of including rigid-body

motions in flutter analysis was first reported by Frazer and Duncan (Ref. 47). Rigid-body effects were also included in studies of aft-swept wings (Refs. 48-49), delta wings (Ref. 50) and sounding rockets with unswept wings (Ref. 52). All of these studies indicated that rigid-body degrees of freedom play an important role in determining not only the type of instability, but also the airspeed at which the system becomes unstable.

A detailed discussion of the aeroelastic effects of rigid-body motions is given in Ref. 51. With rigid-body freedom, a new type of dynamic instability, known as body-freedom flutter (BFF), may be more critical (*i.e.* occur at a lower airspeed) than both divergence and classical bending-torsion flutter experienced by a cantilever wing. The BFF mechanism is a coalescence of the rigid-body pitch mode and a span-wise wing bending mode. As airspeed increases, the frequency of the pitch mode increases while the frequency of the bending mode decreases. When the frequencies merge one of the modes becomes unstable.

Miller *et al.* (Ref. 45) demonstrated that BFF replaced clamped divergence as the critical instability for several free-flying forward-swept wing configurations. Weisshaar *et al.* (Ref. 46) produced similar results using an idealized three-degree-of-freedom model including rigid-body pitch and plunge and one wing bending mode. Analytical trends were verified experimentally through a series of wind tunnel experiments at the Air Force Flight Dynamics Laboratory (AFFDL). Weisshaar and Zeiler (Ref. 53) then extended the model of Ref. 46 to include forward-swept wing aircraft designs with tails or canards to help increase the aircraft's longitudinal stability characteristics. Important results common to the three studies above are summarized below:

- Body-freedom flutter of forward-swept wing aircraft may occur in flight at airspeeds significantly lower than both the wing clamped divergence and bending-torsion flutter airspeeds.

- Decreasing the distance between the aircraft and wing centers of mass tends to increase the body-freedom flutter speed but decrease the divergence speed.

- One cannot expect to avoid body-freedom flutter simply by increasing the divergence speed of a forward-swept wing through aeroelastic tailoring.

In light of the fact that body-freedom flutter cannot be avoided through passive means alone, a more recent technique for suppressing divergence and body-freedom flutter on forward-swept wings involved the use of active feedback control systems. Initial studies demonstrated that separate control of static divergence and bending-torsion flutter on a clamped forward-swept wing was feasible (Ref. 54). Active suppression of body-freedom flutter was also achieved (Refs. 45,55). Simultaneous prevention of both divergence and bending-torsion flutter (for a clamped model) or body-freedom flutter and bending-torsion flutter (for a model free in pitch) was demonstrated by Noll *et al.* (Ref. 56). In all of these studies, classical control laws were designed for feedback of accelerometer signals to control surface actuators.

Zeiler and Weisshaar applied optimal control theory to the problem of body-freedom flutter suppression on forward-swept wings (Ref. 57). However, for certain model configurations the resulting control laws were not effective. As a result, they proposed a method of simultaneously designing a structure and control law which were effective together, known as aeroservoelastic tailoring. By combining structural optimization (composite tailoring) and control optimization into a single design problem, they were able to produce more effective control laws for flutter suppression. Zeiler and Weisshaar attribute the

better performance of aeroservoelastic flutter suppression to an added degree of passive stabilization and/or enhanced controllability of certain modes.

1.7 Adaptive Wing Design

As indicated previously, nearly all of the active control designs for flutter suppression to date utilize control surface deflections to alter the aerodynamic loading on the wing. The addition of LE or TE control surfaces and associated subsystems to an existing wing structure involves a costly configuration change as well as a substantial weight penalty. In modern high-speed aircraft, control surfaces are generally dedicated to maximizing aircraft maneuver performance and cruise efficiency. For example, the Grumman X-29A forward-swept wing demonstrator uses a digital fly-by-wire flight control system in which the flaperons, canards and strake flaps are programmed to optimize the lift-to-drag ratio (Ref. 58). Degraded flight performance, or even instability, as a result of interaction between existing flight control systems and added flutter control systems is therefore a concern (Refs. 58,59). The excessive control surface deflection and/or deflection rate experienced during validation of some flutter suppression designs could increase drag and degrade overall flight efficiency. In light of the above concerns, active flutter suppression systems have not yet gained widespread acceptance in the commercial and military aircraft industries (Ref. 60).

One alternative to conventional lifting surfaces for wing aeroelastic control is the use of adaptive materials such as piezoelectric ceramics and films, magnetostrictive metals and fiber optics. Adaptive materials provide the control designer with a means of inducing strain within the host structure and thereby altering its dynamic characteristics. In particular, piezoelectric materials deform

under application of an external electric field. When mounted symmetrically about the midplane of a plate, piezoelectric actuators can be used to generate controllable bending moments or in-plane loads. In the design of an adaptive wing, piezoelectric actuators provide a unique approach to altering aerodynamic loading by inducing deformations in the wing itself. A logical conclusion is that piezoelectric actuation represents a viable alternative to conventional control surface actuation for flutter or divergence suppression.

The basic premise behind adaptive structure design is that adaptive materials are incorporated into the structure itself, thus giving the structure the ability to sense and react to changes in its dynamic state according to an appropriate control law. During the past decade, the design of adaptive structures has gained widespread acceptance in the field of large space structure design, with the early work concentrating on accurately modeling the relationship between applied voltage and induced strain. Simple models of resultant static forces and moments on one-dimensional structures were developed by Bailey and Hubbard (Ref. 79), Crawley and de Luis (Refs. 61-63), Fanson and Caughey (Ref. 64) and extended to two-dimensional structures by Dimitriadis *et al.* (Ref. 65). For dynamic analysis, these static resultant forces were used in the system equations of motion in an approximate fashion.

A more realistic model of piezoelectric actuator/structure interaction was developed by treating actuators as plies in a composite laminate (Refs. 66-68). In this manner actuation strain energy expressions follow directly from classical laminated plate theory (CLPT). Experimental results have verified that piezoelectric plies are capable of exciting bending and torsional modes independently or simultaneously in composite laminates.

Piezoelectric materials have also been utilized as effective sensors for control purposes (Refs. 66,69,70). When subjected to a mechanical deformation, a piezoelectric material accumulates a measurable output voltage. This property, together with their light weight and high strength, makes piezoelectrics ideal for use as sensing materials in modern aircraft structures. Experiments have demonstrated the possibility of using piezoelectric films to sense independent modes of beam vibration (Ref. 66) as well as measuring strain and strain rate (Refs. 69-70). One advantage of using piezoelectric sensor/actuator combinations is the possibility of sensor/actuator collocation, which tends to reduce the likelihood of control spillover into uncontrolled or unmodeled system modes (Ref. 71). Piezoelectric patches mounted symmetrically about a plate midplane amount to a collocated sensor/actuator pair. Alternatively, Dosch *et al.* describe a technique by which a single piezoelectric patch may be used as a self-sensing actuator (Ref. 72).

A large amount of research has demonstrated the feasibility of using piezoelectric sensors and actuators for vibration and shape control of beams, plates and truss members (Refs. 69,72-81). In fact, adaptive structure designs have shown promising results for a wide variety of control laws, including full-state LQR design (Refs. 73,74), positive position feedback (Refs. 72,75,76), independent modal space control (Refs. 77,78) and nonlinear distributed parameter control theory (Refs. 79,80). Only recently has attention been focused on the use of adaptive materials for aeroelastic control.

Static aeroelastic control has been the subject of investigations by Librescu, Meirovitch and Song (Ref. 81), Lazarus and Crawley (Ref. 82) and Ehlers and Weisshaar (Refs. 83,84). Lazarus and Crawley (Ref. 82) and Librescu

et al. (Ref. 81) demonstrated the possibility of altering natural frequencies and inducing bending and twist via piezoelectric actuation in composite cantilever plate and thin-walled beam wing models, respectively. Ehlers and Weisshaar reported that feedback produced by embedded piezoelectric actuators was sufficient to alter the divergence speeds of straight and swept cantilever beam models (Refs. 83,84). Typical section analysis of adaptive composite beam models was the basis of studies conducted by Lazarus, Crawley and Bohlmann (Ref. 85) and Lazarus, Crawley and Lin (Ref. 86). In both studies, adaptive wings with piezoelectric actuators were compared to conventional articulated lifting surfaces for a variety of aeroelastic tasks, including divergence and flutter suppression. The important result from these studies is that adaptive actuators can provide greater control authority and lower weight penalties than conventional lifting surfaces for a variety of wing configurations.

Results from applications of piezoelectric materials to dynamic aeroelastic problems, such as flutter suppression, are very limited. Experimental results reported by Heeg (Ref. 60) represent the first use of piezoelectric devices to suppress flutter. The idealized wing model used for this study consisted of a rigid metallic wing with a flexible mount system allowing translation and twist. Piezoelectric actuators were attached to leaf springs in the mount system and used with a simple state feedback control law to stabilize the system at wind-tunnel conditions up to 20% above the open-loop flutter speed. More recently, adaptive materials have been used as plies in composite laminates for flutter suppression in simply-supported rectangular panels (Refs. 87,88) and cantilevered rectangular plates (Ref. 89). At this point, no attempt has been made to investigate the effectiveness of using adaptive materials for flutter

suppression in a free-flying aircraft configuration. This is the focus of the present research effort.

1.8 Modeling Considerations

The goal of this research is the development of a modern adaptive aircraft wing capable of sensing its current dynamic state and responding in such a manner as to avoid the occurrence of aeroelastic instabilities. The basic premise is that optimal wing designs of the future will be lightweight, highly flexible and capable of taking advantage of a combination of structural and control optimization to alleviate aeroelastic problems arising from flexibility. The emphasis is on wing design through a combination of passive composite tailoring and active feedback control via piezoelectric actuation. As mentioned earlier, the body-freedom flutter mechanism involves a coalescence of two wing aeroelastic modes which originate from the first wing flexible bending and rigid-body pitch modes. The hypothesis to be investigated in this study is that BFF control can be realized by altering the dynamics of only the predominately flexible mode. A review of technical literature has revealed that the problem of using adaptive materials for suppression of wing flutter on a free-flying aircraft configuration has not been studied. Thus, this research represents a unique application of piezoelectric materials to the solution of a realistic problem.

Any control design must be based on a sound mathematical model of the system behavior. In the present application, the interest lies in a structural model incorporating the physical characteristics essential to a flutter analysis of aircraft with low aspect ratio composite wings suitable for flight in the supersonic regime. The aspect ratios of practical wings for supersonic flight tend to be too low to be approximated by a beam model. Drag considerations require an

efficient supersonic wing with a low thickness ratio. Also, it has been shown that realistic amounts of airfoil camber have little effect on displacements due to unsteady pressure loading, so that camber may be omitted without loss of generality (Ref. 96). In view of these physical requirements, a two-dimensional trapezoidal anisotropic plate wing model is suggested. Piezoelectric sensors and actuators are included as plies in the laminate for the purpose of aeroelastic control. Additionally, fuselage rigid-body degrees of freedom are included for accurate modeling of flutter under free-flight conditions.

It is a well known fact that composite materials exhibit large flexibility in transverse shear, invalidating the classical Kirchoff assumption of infinite rigidity (Refs. 90-92). In fact, neglecting shear deformability can result in serious errors in modeling static and dynamic response of composite structures. Kirchoff theory results in overestimation of natural frequencies (Refs. 92,93) and flutter airspeeds (Refs. 94,95) and underestimation of transverse deflection (Ref. 92). For these reasons, the effects of shear deformation are considered in the present model.

In the interest of structural optimization, the structural model must be general enough to represent a variety of general wing planforms. To this end, we consider a wing with variable midchord sweep angle, so that forward- or aft-swept designs are possible. Furthermore, the anisotropic plate is assumed to consist of several variable-thickness, generally orthotropic layers with varying fiber orientation angles.

The following chapters contain the details of a comprehensive research effort, including development of a mathematical model of an aircraft in straight and level flight, aeroelastic analysis of the model and an investigation of the

feasibility of controlling flutter in a free-flying aircraft with piezoelectric sensors and actuators mounted on the wing surfaces. The kinetic and potential energy expressions and the virtual work due to aerodynamic loading are developed in Chapters 2 and 3, respectively. Then they are used in conjunction with a variational principle to derive the governing equations of motion in Chapter 3. In Chapter 4, an approximation to the free vibration and flutter eigenvalue problems is derived through spatial discretization in terms of admissible functions. Flutter analysis is carried out for various aircraft configurations and two aerodynamic theories, quasi-steady and quasi-static piston theory. In addition, a modal approximation to the flutter eigenvalue problem is presented, resulting in drastically reduced computation time without significant loss in accuracy. The aeroelastic model developed in Chapter 4 is used in Chapter 5 for controlling body-freedom flutter. The effects of aeroelastic tailoring are investigated, and two output feedback active control laws are derived, using wing-mounted piezoelectric elements as sensors and actuators. Numerical results for an example configuration are presented in the form of closed-loop flutter analysis and closed-loop gust response. Finally, based on the simulations, some conclusions are drawn and suggestions made for future areas of study.

CHAPTER 2

SYSTEM KINETIC AND STRAIN ENERGY FORMULATION

2.1 Model Overview

A fundamental objective is to develop a structural model as simple as possible so as to keep the computation time reasonable. To this end, we choose a symmetric laminate model of the elastic wing since there is no coupling between bending and stretching displacements, drastically simplifying the strain energy expression. Furthermore, the aircraft mass distribution is assumed to be symmetric about the fuselage centerline, so that it is only necessary to model half of the aircraft.

A view of the aircraft model is shown in Fig. 2.1. The wing is modeled as a trapezoidal, shear deformable, composite plate with root and tip chords parallel to the flow. Fuselage mass and inertia are included and the model is assumed to undergo rigid-body plunge and pitch motions. There are $2k$ symmetrically stacked, variable thickness, generally orthotropic plies in the laminate (Fig. 2.2). The piezoelectric patches are mounted symmetrically on both the upper and lower surfaces of the wing.

The following sections describe a rigorous derivation of the system kinetic and strain energy expressions based on the principles of analytical dynamics and the theory of elasticity. In the following chapter, these expressions will be used in the extended Hamilton's principle to derive the system equations of motion. We begin with a definition of the planform nomenclature and the system displacements.

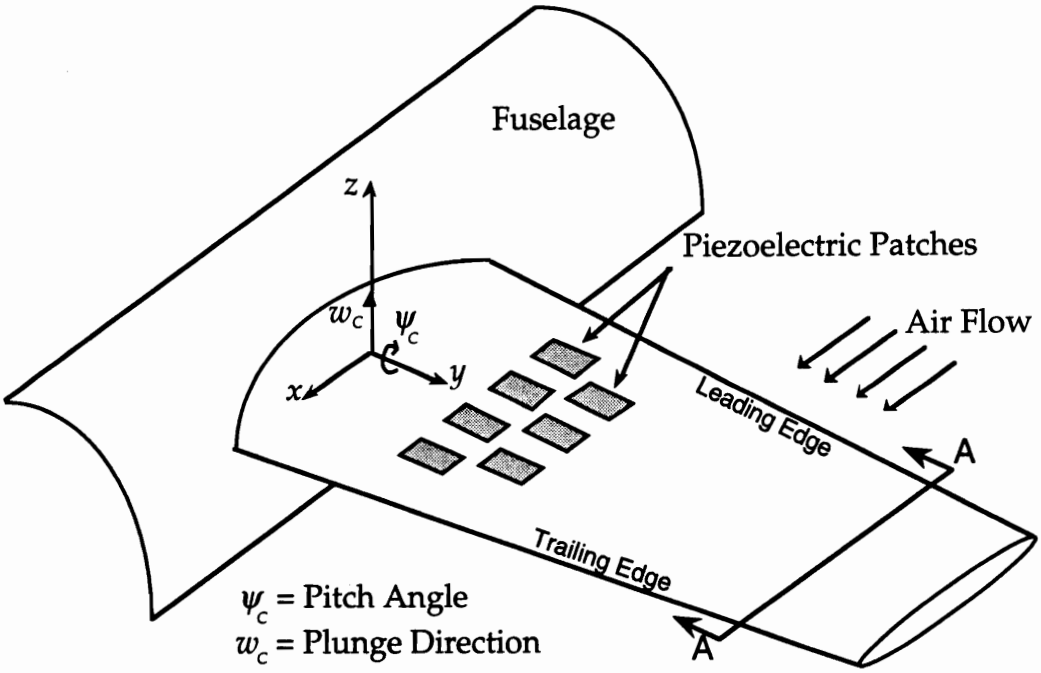

Fig. 2.1 - Aircraft Wing with Surface-Mounted Piezoelectric Patches

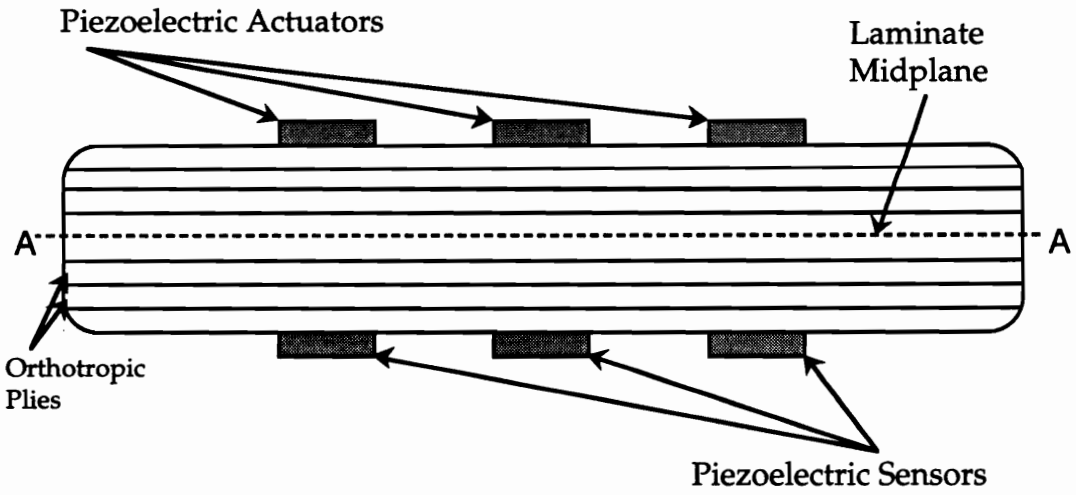

Fig. 2.2 - Laminate Cross Section

2.2 Definition of Displacements and Boundary Conditions

The mathematical model consists of an elastic plate attached to a rigid fuselage. The fuselage is assumed to undergo rigid-body rotation about an axis parallel to the y-axis through the system center of mass (point C) and rigid-body displacement of the center of mass in the vertical direction (Fig. 2.1). The absolute displacement of a point on the fuselage is given by

$$w_f(x,t) = w_C(t) + (x - x_C)\psi_C(t) \tag{2.1}$$

where x_C is the position of the system center of mass, w_C is the rigid-body plunge and ψ_C the rigid-body pitch angle.

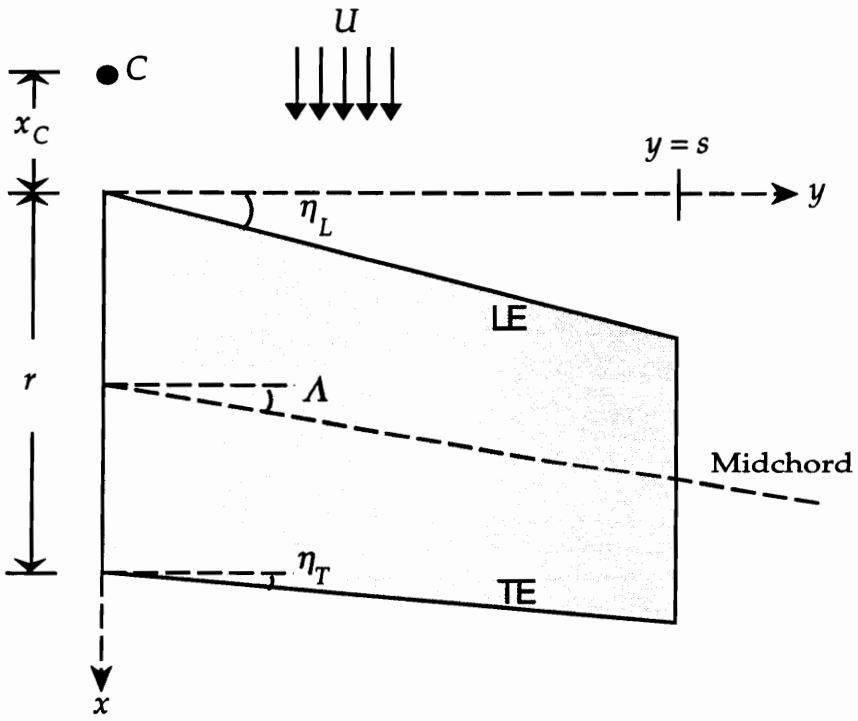

Fig. 2.3 - General Swept-Wing Planform

A top view of the flexible wing with mid-chord sweep angle, Λ, is shown in Fig. 2.3. Both the leading edge (LE) and trailing edge (TE) are functions of the y coordinate, η_L and η_T are the LE and TE sweep angles, r is the wing root length

and s is the semispan. Following the usual conventions for aeroelastic analysis, x is considered positive towards the TE and all sweep angles are positive for aft-swept configurations. The absolute displacement of a point on the flexible wing is given by

$$u(x,y,z,t) = z\psi_x(x,y,t), \quad v(x,y,z,t) = -z\psi_y(x,y,t)$$
$$w_p(x,y,t) = w_C(t) + (x - x_C)\psi_C(t) + w(x,y,t) \tag{2.2a,b,c}$$

in which u and v are elastic displacements in the x and y directions, ψ_x and ψ_y are rotations about the y and x axes, respectively, of a line originally normal to the mid-plane of the undeformed plate and w is the transverse elastic displacement of the plate. In accordance with first-order shear deformation theory (Ref. 98), the Kirchoff assumption that line segments remain normal to the plate midplane has been dropped. The resulting shear deformation is linear through the thickness and w, ψ_x and ψ_y are independent displacement variables. The rigid attachment of the plate to the fuselage is represented mathematically by the geometric boundary conditions, $w = \psi_x = \psi_y = 0$ along $y = 0$. The remaining three plate edges are free and thus the corresponding displacements are governed by natural boundary conditions.

2.3 System Kinetic Energy

The total kinetic energy of the aircraft model includes contributions from both rigid-body motions and elastic plate deformations. With the fuselage and wing displacements given by Eqs. (2.1) and (2.2), the system kinetic energy takes the form

$$
\begin{aligned}
T &= \tfrac{1}{2}\int_{M_f} \dot{w}_f^2 dM_f + \tfrac{1}{2}\int_{M_p} \left(\dot{u}^2 + \dot{v}^2 + \dot{w}_p^2\right) dM_p \\
&= \tfrac{1}{2}\int_{M_f} \left[\dot{w}_C + (x - x_C)\dot{\psi}_C\right]^2 dM_f + \tfrac{1}{2}\int_{M_p} \left\{z^2\left(\dot{\psi}_x^2 + \dot{\psi}_y^2\right) + \left[\dot{w}_C + (x - x_C)\dot{\psi}_C + \dot{w}\right]^2\right\} dM_p \\
&= \tfrac{1}{2}\left(M_C \dot{w}_C^2 + I_C \dot{\psi}_C^2\right) + \tfrac{1}{2}\int_{A_p} \left[m_p \dot{w}^2 + I_p\left(\dot{\psi}_x^2 + \dot{\psi}_y^2\right)\right] dA_p \\
&\quad + \dot{\psi}_C \int_{A_p} m_p (x - x_C)\dot{w} dA_p + \dot{w}_C \int_{A_p} m_p \dot{w} dA_p
\end{aligned} \tag{2.3}
$$

where

$$
M_C = M_f + M_p, \quad I_C = \int_{M_f} (x - x_C)^2 dM_f + \int_{M_p} (x - x_C)^2 dM_p \tag{2.4a,b}
$$

$$
m_p = \sum_{j=-k}^{k} \int_{h_{j-1}}^{h_j} \rho_j dz, \quad I_p = \sum_{j=-k}^{k} \int_{h_{j-1}}^{h_j} \rho_j z^2 dz \tag{2.4c,d}
$$

in which M_f is the total mass of the fuselage, M_p the total mass of the plate, m_p the mass per unit area of plate, ρ_j the mass per unit volume of plate and I_p the mass moment of inertia per unit area of plate. Note that there are $2k$ plies and h_j - h_{j-1} defines the thickness of ply j. For the Cartesian coordinates of Fig. 2.3, the integration over the domain of the plate is given by

$$
\int_{A_p} dA_p = \int_0^s \int_{LE}^{TE} dx dy \tag{2.5}
$$

2.4 System Potential Energy

The potential energy for the wing/fuselage system consists only of the elastic strain energy in the flexible wing. The total strain energy arises from two sources, namely the energy stored during deformation of the plate and also the strain energy induced via piezoelectric actuation. In deriving the total strain energy expressions, we must first examine the form of the strain-displacement relations and the material constitutive equations.

Under the assumption of small displacements, a linear relationship exists between displacements and strains, given by (Ref. 99)

$$\varepsilon_x = \frac{\partial u}{\partial x}, \quad \varepsilon_y = \frac{\partial v}{\partial y}, \quad \varepsilon_z = \frac{\partial w}{\partial z} \tag{2.6a,b,c}$$

$$\gamma_{yz} = \frac{\partial v}{\partial z} + \frac{\partial w}{\partial y}, \quad \gamma_{xz} = \frac{\partial u}{\partial z} + \frac{\partial w}{\partial x}, \quad \gamma_{xy} = \frac{\partial u}{\partial y} + \frac{\partial v}{\partial x} \tag{2.6d,e,f}$$

where the shear strains are recognized as engineering shear strain components. Substitution of Eqs. (2.2) into Eqs. (2.6) leads to the following simplified form

$$\varepsilon_x = z\psi_{x,x}, \quad \varepsilon_y = z\psi_{y,y}, \quad \varepsilon_z = 0 \tag{2.7a,b,c}$$

$$\gamma_{yz} = \psi_y + w_{,y}, \quad \gamma_{xz} = \psi_x + w_{,x}, \quad \gamma_{xy} = z\left(\psi_{x,y} + \psi_{y,x}\right) \tag{2.7d,e,f}$$

where the symbols $,x$ and $,y$ in the subscripts denote partial derivatives with respect to x and y, respectively.

A drawing of the j^{th} generally orthotropic layer is shown in Fig. 2.4.

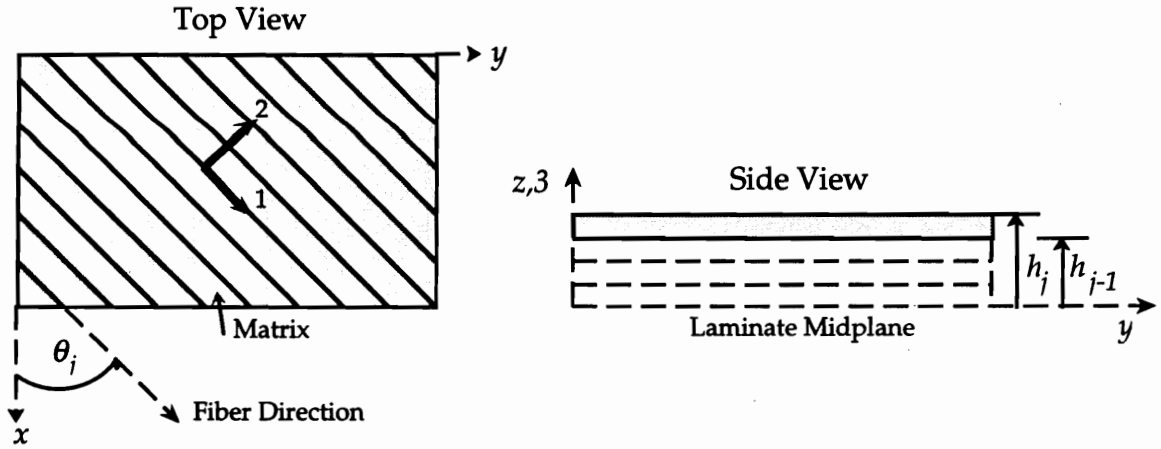

Fig. 2.4 - Composite Layer Nomenclature

Coordinate axes (1,2) are aligned with the principal material directions. The fiber orientation angle, θ_j, is the angle from the plate x axis to the principal fiber direction (1 axis).

From Eq. (2.7c), we conclude that there is no strain through the plate thickness, $\varepsilon_z = \varepsilon_3 = 0$. The constitutive equations in terms of the principal coordinates for the j^{th} layer take the form

$$\begin{bmatrix} \sigma_1 \\ \sigma_2 \\ \tau_{23} \\ \tau_{13} \\ \tau_{12} \end{bmatrix}^j = [Q]^j \begin{bmatrix} \varepsilon_1 \\ \varepsilon_2 \\ \gamma_{23} \\ \gamma_{13} \\ \gamma_{12} \end{bmatrix}^j \tag{2.8}$$

where $[Q]^j$ is the generalized stiffness matrix for the composite material, whose elements are related to the material properties by (Ref. 100)

$$Q_{11}^j = \left(\frac{E_1}{1-\upsilon_{12}\upsilon_{21}}\right)^j, Q_{22}^j = \left(\frac{E_2}{1-\upsilon_{12}\upsilon_{21}}\right)^j, Q_{12}^j = \upsilon_{12}Q_{22}^j \tag{2.9a,b,c}$$

$$Q_{44}^j = G_{23}^j, \; Q_{55}^j = G_{13}^j, \; Q_{66}^j = G_{12}^j \tag{2.9d,e,f}$$

where E_i, G_{im}, and ν_{im} are Young's moduli, shear moduli and Poisson's ratios, respectively.

The wing laminate is assumed to be composed of several plies of varying orientation angle. In order to derive a consistent form of the strain energy for the entire laminate, we must first transform the constitutive equations of each ply to global, xyz, coordinates. To this end, we realize that stress and tensorial strain components transform as 2^{nd} order tensors, or

$$\begin{bmatrix}\sigma_x\\ \sigma_y\\ \tau_{yz}\\ \tau_{xz}\\ \tau_{xy}\end{bmatrix}^j = [T_j]^{-1}\begin{bmatrix}\sigma_1\\ \sigma_2\\ \tau_{23}\\ \tau_{13}\\ \tau_{12}\end{bmatrix}^j, \quad \begin{bmatrix}\varepsilon_x\\ \varepsilon_y\\ \gamma_{yz}/2\\ \gamma_{xz}/2\\ \gamma_{xy}/2\end{bmatrix}^j = [T_j]^{-1}\begin{bmatrix}\varepsilon_1\\ \varepsilon_2\\ \gamma_{23}/2\\ \gamma_{13}/2\\ \gamma_{12}/2\end{bmatrix}^j \tag{2.10a,b}$$

where $\frac{\gamma_{ij}}{2}$ is recognized as tensorial strain, and

$$[T_j] = \begin{bmatrix} \cos^2\theta_j & \sin^2\theta_j & 0 & 0 & \sin 2\theta_j \\ \sin^2\theta_j & \cos^2\theta_j & 0 & 0 & -\sin 2\theta_j \\ 0 & 0 & \cos\theta_j & -\sin\theta_j & 0 \\ 0 & 0 & \sin\theta_j & \cos\theta_j & 0 \\ -\frac{1}{2}\sin 2\theta_j & \frac{1}{2}\sin 2\theta_j & 0 & 0 & \cos 2\theta_j \end{bmatrix} \tag{2.11}$$

Substitution of transformations (2.10) into Eq. (2.8) yields the constitutive equations for the j^{th} ply of composite material in global coordinates, or

$$\begin{bmatrix}\sigma_x\\ \sigma_y\\ \tau_{yz}\\ \tau_{xz}\\ \tau_{xy}\end{bmatrix}^j = [\overline{Q}]^j\begin{bmatrix}\varepsilon_x\\ \varepsilon_y\\ \gamma_{yz}\\ \gamma_{xz}\\ \gamma_{xy}\end{bmatrix}^j \tag{2.12}$$

where $\overline{Q}^j$ is the reduced stiffness matrix for the j^{th} layer, given by

$$[\overline{Q}]^j = [T_j]^{-1}[Q^j][T_j]^{-T} \tag{2.13}$$

Piezoelectric materials have naturally occurring or induced dipoles within their crystalline substructure (Fig. 2.5). When a voltage is applied parallel to the dipole direction, a Poisson-like effect causes either in-plane contraction or expansion depending on the sign of the applied voltage. If patches are mounted symmetrically about the plate mid-plane, applying opposing voltages causes pure bending strain within the host structure. The resultant induced moment

increases with the distance between the patches, thus surface-mounted patches are considered for maximum control authority.

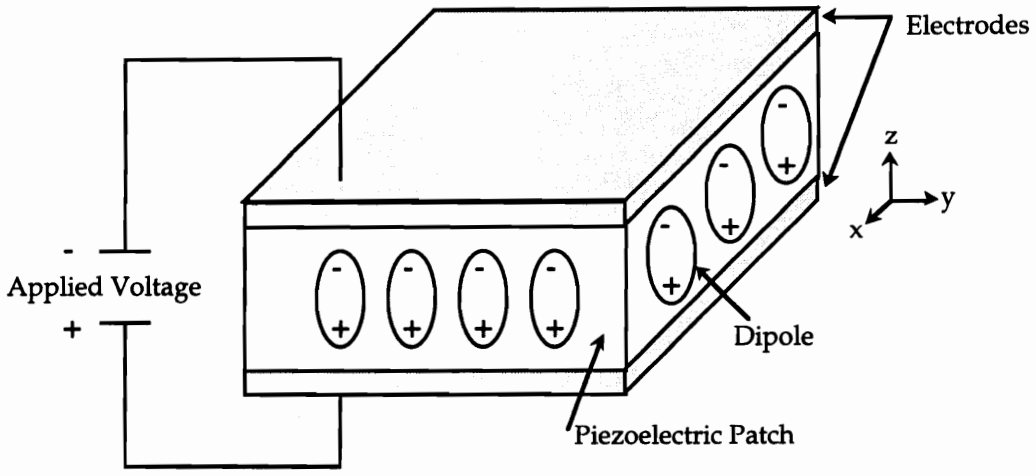

Fig. 2.5 - Piezoelectric Patch Nomenclature

Mathematically, the piezoelectric patches are treated as surface-mounted isotropic plies. The voltage is applied uniformly through the actuator thickness (Fig. 2.5) with electrodes mounted on the patch upper and lower surfaces. Induced strain from bonded piezoelectric actuators is analogous to thermally-induced free strain (Ref. 68). For each patch, the relationship between stress and mechanical strain is given by

$$\begin{Bmatrix} \sigma_x \\ \sigma_y \end{Bmatrix}_p = \begin{bmatrix} Q_{11} & Q_{12} \\ Q_{21} & Q_{22} \end{bmatrix}_p \begin{Bmatrix} \varepsilon_x - \Lambda_x \\ \varepsilon_y - \Lambda_y \end{Bmatrix}_p \tag{2.14}$$

where Λ_x and Λ_y are voltage-induced strains. For an ideal piezoelectric material, in which hysteresis and nonlinear material behavior are neglected, the induced in-plane strains are directly proportional to the voltage applied in the z direction, or

$$\begin{Bmatrix} \Lambda_x \\ \Lambda_y \end{Bmatrix}_p = \begin{Bmatrix} d_{31} \\ d_{32} \end{Bmatrix}_p \frac{V_z(x,y,t)}{t_a} \tag{2.15}$$

in which d_{31} and d_{32} are piezoelectric constants relating voltage applied in the z direction, $V_z(x,y,t)$, to displacement in the x and y directions and t_a is the patch thickness. It should be noted that isotropic patches are not capable of inducing shear strains. The components of the piezoelectric reduced stiffness matrix, Q_p, are given by

$$Q_{p_{11}} = Q_{p_{22}} = \left(\frac{E}{1-\upsilon^2}\right)_p, \quad Q_{p_{12}} = Q_{p_{21}} = \left(\frac{\upsilon E}{1-\upsilon^2}\right)_p \tag{2.16a,b}$$

where, according to the exact constitutive equations, the material properties are those measured under conditions of constant electric field (Ref. 112).

The total laminate strain energy function is derived following the well defined framework of laminated plate theory with first-order shear deformation (Ref. 98). Recall that there are $2k$ plies in the symmetric laminate. The actuators are modeled as symmetric pairs of surface mounted plies divided into m segments distributed on the wing surface (Fig. 2.6).

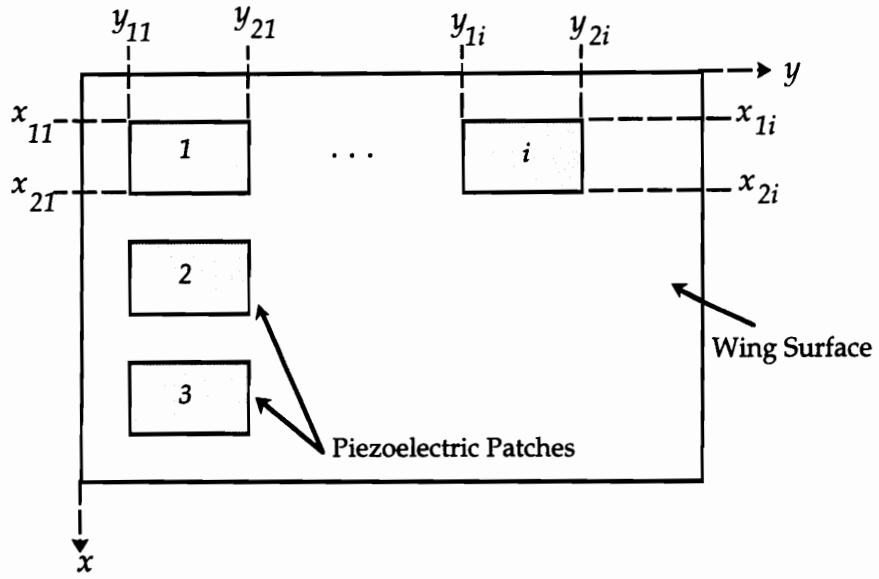

Fig. 2.6 - Spatial Distribution of Actuators

The spatial dependence of the actuation strain is included implicitly through the applied voltage field, which may be expressed in the form

$$V_z(x,y,t) = \sum_{i=1}^{m} V_{zi}(t)\left[u(x-x_{1i}) - u(x-x_{2i})\right]\left[u(y-y_{1i}) - u(y-y_{2i})\right] \equiv \boldsymbol{R}_p^T \boldsymbol{v}_c(t) \quad (2.17)$$

where $u(x - x_1)$ is the spatial unit step function, defined as

$$u(x-x_1) = \begin{cases} 0 & x < x_1 \\ 1 & x \geq x_1 \end{cases} \quad (2.18)$$

and $\boldsymbol{R_p}(x,y)$ and $\boldsymbol{v}_c(t)$ are m-vectors of actuator placement functions and control voltages, respectively.

The strain energy per unit of plate area for a single layer, or its counterpart below the midplane, is given by

$$\hat{V}_j = \tfrac{1}{2}\int_{h_{j-1}}^{h_j}\left[\sigma_x\varepsilon_x + \sigma_y\varepsilon_y + \frac{\tau_{yz}\gamma_{yz}}{2} + \frac{\tau_{xz}\gamma_{xz}}{2} + \frac{\tau_{xy}\gamma_{xy}}{2}\right]dz, \quad j = -k, -k+1, \ldots, k \quad (2.19a)$$

for the laminate, and

$$\hat{V}_p = \tfrac{1}{2}\int_{h_k}^{h_{k+1}} \left[\sigma_x \varepsilon_x + \sigma_y \varepsilon_y\right]_p dz \tag{2.19b}$$

for the actuators. Next, the total strain energy is obtained by adding the strain energy densities of the plate and actuators and integrating over the domain of the plate. Taking advantage of the actuator symmetry, we have

$$V = \int_{A_p} \left[\sum_{j=-k}^{k} \hat{V}_j + 2\hat{V}_p\right] dA_p \tag{2.20}$$

Substitution of the strain-displacement relations, Eqs. (2.7), and the constitutive equations, Eqs. (2.12), (2.14) and (2.15), into Eq. (2.20) yields the total laminate strain energy as a function of the displacement variables, or

$$\begin{aligned} V = \tfrac{1}{2}\int_{A_p} \sum_{j=-k}^{k} \Big\{ \tfrac{1}{3}\left(h_j^3 - h_{j-1}^3\right)\Big[\overline{Q}_{11}^j \psi_{x,x}^2 + \overline{Q}_{22}^j \psi_{y,y}^2 + \overline{Q}_{66}^j \left(\psi_{x,y} + \psi_{y,x}\right)^2 + 2\overline{Q}_{12}^j \psi_{x,x}\psi_{y,y} \\ + 2\overline{Q}_{16}^j \psi_{x,x}\left(\psi_{x,y} + \psi_{y,x}\right) + 2\overline{Q}_{26}^j \psi_{y,y}\left(\psi_{x,y} + \psi_{y,x}\right)\Big] + \left(h_j - h_{j-1}\right)\Big[\overline{Q}_{44}^j \left(\psi_y + w_{,y}\right)^2 \\ + \overline{Q}_{55}^j \left(\psi_x + w_{,x}\right)^2 + 2\overline{Q}_{45}^j \left(\psi_x + w_{,x}\right)\left(\psi_y + w_{,y}\right)\Big]\Big\} dA_p \\ - \int_{A_p} \left(h_{k+1} + h_k\right)\tfrac{1}{2}\Big[\left(Q_{p_{11}} d_{31} + Q_{p_{12}} d_{32}\right) V_z \psi_{x,x} + \left(Q_{p_{12}} d_{31} + Q_{p_{22}} d_{32}\right) V_z \psi_{y,y}\Big] dA_p \end{aligned} \tag{2.21}$$

where the stiffness of the piezoelectric patches has been assumed to be negligible compared to the stiffness of the host structure and only the voltage-induced terms from the piezoelectric strain energy have been retained.

In laminate plate theory, the convention is to express the strain energy function in terms of the displacements and the total laminate extension and bending stiffness coefficients, A_{ab} and D_{ab}, defined as

$$A_{ab} = \sum_{j=-k}^{k} (h_j - h_{j-1}) \overline{Q}_{ab}^{j}, \qquad D_{ab} = \tfrac{1}{3} \sum_{j=-k}^{k} (h_j^3 - h_{j-1}^3) \overline{Q}_{ab}^{j} \tag{2.22a,b}$$

Furthermore, with induced strain actuation, it is convenient to define the piezoelectric stiffness coefficients, given by

$$F_{ab} = \tfrac{1}{2}(h_k + h_{k+1}) Q_{p_{ab}} V_z(x, y, t) \tag{2.23}$$

In general, both the layer heights and the actuation voltages vary along the x and y directions. Therefore, all the above stiffness coefficients are in general functions of both x and y. Using Eqs. (2.22) and (2.23), the total laminate strain energy can be expressed in the compact form

$$\begin{aligned} V = \int_{A_p} \langle \tfrac{1}{2} & \begin{Bmatrix} \psi_{x,x} \\ \psi_{y,y} \\ \psi_{x,y} + \psi_{y,x} \end{Bmatrix}^T \begin{bmatrix} D_{11} & D_{12} & D_{16} \\ D_{12} & D_{22} & D_{26} \\ D_{16} & D_{26} & D_{66} \end{bmatrix} \begin{Bmatrix} \psi_{x,x} \\ \psi_{y,y} \\ \psi_{x,y} + \psi_{y,x} \end{Bmatrix} \\ & + \tfrac{1}{2} \begin{Bmatrix} \psi_y + w_{,y} \\ \psi_x + w_{,x} \end{Bmatrix}^T \begin{bmatrix} A_{44} & A_{45} \\ A_{45} & A_{55} \end{bmatrix} \begin{Bmatrix} \psi_y + w_{,y} \\ \psi_x + w_{,x} \end{Bmatrix} \\ & - \begin{Bmatrix} \psi_{x,x} \\ \psi_{y,y} \end{Bmatrix}^T \begin{bmatrix} F_{11} & F_{12} \\ F_{12} & F_{22} \end{bmatrix} \begin{Bmatrix} d_{31} \\ d_{32} \end{Bmatrix} \rangle dA_p \end{aligned} \tag{2.24}$$

CHAPTER 3

SYSTEM EQUATIONS OF MOTION

3.1 Extended Hamilton's Principle

The objective in this chapter is the derivation of all the differential equations governing the motion of the system shown in Fig. 2.1. To this end, we employ a variational principle known as the extended Hamilton's principle (Ref. 101). One advantage to this approach is that all the system equations of motion can be derived from three scalar functions, the kinetic energy, the potential energy and the virtual work of the nonconservative forces. The formulation is equally applicable to both discrete and distributed systems. Moreover, the extended Hamilton's principle is formulated in terms of generalized coordinates, and thus is invariant with respect to the choice of coordinates.

The extended Hamilton's principle can be written in the form

$$\int_{t_1}^{t_2} (\delta T - \delta V + \delta W)dt = 0, \quad \delta q_i(t_1) = \delta q_i(t_2) = 0, \quad i = 1,2,...,n \tag{3.1}$$

where δT is the variation in the system kinetic energy, δV the variation in system potential energy, δW the virtual work performed by all nonconservative forces present and δq_i the virtual displacement (variation in position without an associated change in time) of the generalized coordinates. Equation 3.1 is derived in Ref. 101 based on D'Alembert's principle and the principle of virtual work. Before proceeding with the equations of motion for the problem at hand, we must first derive an expression for the virtual work done by all nonconservative forces.

3.2 Virtual Work Done by Aerodynamic Forces

The only nonconservative forces acting on the aircraft model of Fig. 2.1 are due to the aerodynamic loading of the wing, namely distributed lift forces and moments. A large amount of research has been carried out towards the goal of accurately modeling unsteady aerodynamic loading for aeroelastic applications. Models range from simple point-function relationships between pressure and wing displacement (Refs. 102-105) to complex exact results based on potential flow theory (Ref. 106). Likewise, models of varying complexity exist for each of the various flight regimes, including subsonic (compressible and incompressible), transonic, supersonic and hypersonic airspeeds.

For the current research effort, the interest lies in modeling the flight of an advanced aircraft configuration typical of next generation fighter aircraft. The wing model under consideration is a thin trapezoidal wing characterized by low to moderate aspect ratio. The flight regime of interest for such a wing is undoubtedly supersonic.

For large Mach numbers, there is a weak memory effect as well as weak three-dimensional effects. These factors suggest the use of an approximate aerodynamic theory known as piston theory (Ref. 105), in which the pressure difference between the upper and lower surfaces of the plate is related to the absolute displacement of the plate. The point relationship is written conveniently in terms of an aerodynamic operator acting on the absolute wing displacement, or

$$\Delta p = -C(x)\left(\frac{\partial}{\partial x}+\frac{1}{U}\frac{\partial}{\partial t}\right)w_p, \quad C(x)=\frac{4q}{M}\left[1+\frac{\gamma+1}{2}M\frac{\partial t_N}{\partial x}\right] \qquad (3.2a,b)$$

where U is the free-stream airspeed, q the free-stream dynamic pressure, M the free-stream Mach number, γ the ratio of specific heats and t_N the plate half-thickness (Ref. 33).

Piston theory has been shown to match experimental results quite well for Mach numbers greater than about 2.5 (Ref. 105). However, the theory can be expected to follow the trends of the exact theory for lower Mach numbers. A major advantage of piston theory is substantial savings in computational effort. The simple point function relationship permits direct solution of the flutter eigenvalue problem instead of the iterative procedures required by more complex theories. A minor drawback of piston theory is the error in pressure predictions near the wing tips, where three-dimensional effects are more pronounced. The feeling is that the computational benefits outweigh the drawbacks of piston theory for the present study. Certainly, piston theory will be sufficient to develop trends through the use of parameter studies with the present model. A complete investigation of a wing would require appropriate aerodynamic theories for all of the aircraft's flight regimes.

As the wing undergoes a virtual displacement, the total virtual work done by the aerodynamic force distribution is given by

$$\delta W = \int_{A_p} \Delta p \delta w_p dA_p = \int_{A_p} \left[\hat{W}\delta w_C + \hat{W}(x - x_C)\delta\psi_C + \hat{W}\delta w\right] dA_p \tag{3.3}$$

in which δw is the virtual transverse elastic displacement of the plate, δw_C and $\delta\psi_C$ are the virtual displacements of the fuselage and

$$\hat{W} = -C(x)\left\{\psi_C + w_{,x} + \frac{1}{U}\left[\dot{w}_C + (x - x_C)\dot{\psi}_C + \dot{w}\right]\right\} \tag{3.4}$$

3.3 System Equations of Motion

In addition to the virtual work expression, the variation in the system kinetic and potential energy expressions are required for the extended Hamilton's principle. The variation in the system potential energy is found by taking the first variation of Eq. (2.24), or

$$\delta V = \int_{A_p} \Bigg\langle \begin{Bmatrix} \delta\psi_{x,x} \\ \delta\psi_{y,y} \\ \delta\psi_{x,y} + \delta\psi_{y,x} \end{Bmatrix}^T \begin{bmatrix} D_{11} & D_{12} & D_{16} \\ D_{12} & D_{22} & D_{26} \\ D_{16} & D_{26} & D_{66} \end{bmatrix} \begin{Bmatrix} \psi_{x,x} \\ \psi_{y,y} \\ \psi_{x,y} + \psi_{y,x} \end{Bmatrix}$$
$$+ \begin{Bmatrix} \delta\psi_y + \delta w_{,y} \\ \delta\psi_x + \delta w_{,x} \end{Bmatrix}^T \begin{bmatrix} A_{44} & A_{45} \\ A_{45} & A_{55} \end{bmatrix} \begin{Bmatrix} \psi_y + w_{,y} \\ \psi_x + w_{,x} \end{Bmatrix}$$
$$- \begin{Bmatrix} \delta\psi_{x,x} \\ \delta\psi_{y,y} \end{Bmatrix}^T \begin{bmatrix} F_{11} & F_{12} \\ F_{12} & F_{22} \end{bmatrix} \begin{Bmatrix} d_{31} \\ d_{32} \end{Bmatrix} \Bigg\rangle dA_p \tag{3.5}$$

Similarly, the variation in the system kinetic energy comes from Eq. (2.3), and is given by

$$\delta T = \left[M_C \dot{w}_C + \int_{A_p} m_p \dot{w} dA_p \right] \delta\dot{w}_C + \left[I_C \dot{\psi}_C + \int_{A_p} m_p (x - x_C) \dot{w} dA_p \right] \delta\dot{\psi}_C$$
$$+ \int_{A_p} \left\{ m_p \left[\dot{w}_C + (x - x_C)\dot{\psi}_C + \dot{w} \right] \delta\dot{w} + I_p \left[\dot{\psi}_x \delta\dot{\psi}_x + \dot{\psi}_y \delta\dot{\psi}_y \right] \right\} dA_p \tag{3.6}$$

From Eqs. (2.2), the generalized coordinates for the system are the two rigid-body displacement variables for the fuselage, w_C and ψ_C, and the three elastic displacements of the plate, w, ψ_x and ψ_y, so that the extended Hamilton's principle takes the form

$$\int_{t_1}^{t_2} (\delta T - \delta V + \delta W) dt = 0, \quad \delta w_C = \delta\psi_C = \delta w = \delta\psi_x = \delta\psi_y = 0 \quad @ \ t_1, t_2 \tag{3.7}$$

Substitution of Eqs. (3.3), (3.4), (3.5) and (3.6) into Eq. (3.7) yields

$$\int_{t_1}^{t_2}\Big\langle\Big[M_C\ddot{w}_C+\int_{A_p}m_p\ddot{w}dA_p\Big]\delta\dot{w}_C+\Big[I_C\ddot{\psi}_C+\int_{A_p}m_p(x-x_C)\ddot{w}dA_p\Big]\delta\dot{\psi}_C$$

$$+\int_{A_p}\Big\{m_p\big[\ddot{w}_C+(x-x_C)\ddot{\psi}_C+\ddot{w}\big]\delta\dot{w}+I_p\big[\ddot{\psi}_x\delta\dot{\psi}_x+\ddot{\psi}_y\delta\dot{\psi}_y\big]\Big\}dA_p$$

$$-\int_{A_p}C(x)\Big\{\psi_C+w_{,x}+\frac{1}{U}\big[\dot{w}_C+(x-x_C)\dot{\psi}_C+\dot{w}\big]\Big\}\big[\delta w_C+(x-x_C)\delta\psi_C+\delta w\big]dA_p$$

$$-\int_{A_p}\begin{Bmatrix}\delta\psi_{x,x}\\ \delta\psi_{y,y}\\ \delta\psi_{x,y}+\delta\psi_{y,x}\end{Bmatrix}^T[D]\begin{Bmatrix}\psi_{x,x}\\ \psi_{y,y}\\ \psi_{x,y}+\psi_{y,x}\end{Bmatrix}+\begin{Bmatrix}\delta\psi_y+\delta w_{,y}\\ \delta\psi_x+\delta w_{,x}\end{Bmatrix}^T[A]\begin{Bmatrix}\psi_y+w_{,y}\\ \psi_x+w_{,x}\end{Bmatrix}dA_p$$

$$+\int_{A_p}\begin{Bmatrix}\delta\psi_{x,x}\\ \delta\psi_{y,y}\end{Bmatrix}^T[F]\begin{Bmatrix}d_{31}\\ d_{32}\end{Bmatrix}dA_p\Big\rangle dt=0 \qquad (3.8)$$

The above expression of the extended Hamilton's principle contains variations of velocities as well as displacements. Before the equations of motion can be derived, it is necessary to transform the integrand so that it contains virtual displacements alone. This is achieved by integrating the terms containing virtual velocities by parts with respect to time, taking into account that the virtual displacements are identically zero at the end points, t_1 and t_2. The result is

$$-\int_{t_1}^{t_2}\Big\langle\Big[M_C\ddot{w}_C+\int_{A_p}m_p\ddot{w}dA_p\Big]\delta w_C+\Big[I_C\ddot{\psi}_C+\int_{A_p}m_p(x-x_C)\ddot{w}dA_p\Big]\delta\psi_C$$

$$+\int_{A_p}\Big\{m_p\big[\ddot{w}_C+(x-x_C)\ddot{\psi}_C+\ddot{w}\big]\delta w+I_p\big[\ddot{\psi}_x\delta\psi_x+\ddot{\psi}_y\delta\psi_y\big]\Big\}dA_p$$

$$+\int_{A_p}C(x)\Big\{\psi_C+w_{,x}+\frac{1}{U}\big[\dot{w}_C+(x-x_C)\dot{\psi}_C+\dot{w}\big]\Big\}\big[\delta w_C+(x-x_C)\delta\psi_C+\delta w\big]dA_p$$

$$+\int_{A_p}\begin{Bmatrix}\delta\psi_{x,x}\\ \delta\psi_{y,y}\\ \delta\psi_{x,y}+\delta\psi_{y,x}\end{Bmatrix}^T[D]\begin{Bmatrix}\psi_{x,x}\\ \psi_{y,y}\\ \psi_{x,y}+\psi_{y,x}\end{Bmatrix}+\begin{Bmatrix}\delta\psi_y+\delta w_{,y}\\ \delta\psi_x+\delta w_{,x}\end{Bmatrix}^T[A]\begin{Bmatrix}\psi_y+w_{,y}\\ \psi_x+w_{,x}\end{Bmatrix}dA_p$$

$$-\int_{A_p}\begin{Bmatrix}\delta\psi_{x,x}\\ \delta\psi_{y,y}\end{Bmatrix}^T[F]\begin{Bmatrix}d_{31}\\ d_{32}\end{Bmatrix}dA_p\Big\rangle dt=0 \qquad (3.9)$$

Normally, the next step in deriving the system equations of motion would involve integration of the terms in Eq. (3.9) containing derivatives with respect to x and y by parts. Then, invoking the fact that the virtual displacements, δw_C, $\delta \psi_C$, δw, $\delta \psi_x$ and $\delta \psi_y$, are independent and arbitrary, we would arrive at a coupled hybrid system of equations consisting of two ordinary differential equations for the rigid-body motions and three partial differential equations governing the elastic plate deformations. However, control of such a hybrid system of equations is not within the state of the art. Indeed, control must be carried out with a finite number of sensors and actuators, whereas a distributed system such as an aircraft wing has an infinite number of degrees of freedom. For control purposes, we require a mathematical model with a finite number of degrees of freedom, which in turn implies discretization in space of the mathematical model (Ref. 71). As it turns out, it is convenient to carry out spatial discretization directly in the extended Hamilton's principle, before the equations are derived. Spatial discretization is achieved through a series expansion of the system displacement variables. Essentially this amounts to truncation of the infinite system degrees of freedom to a finite number. As a result, the three partial differential equations of motion are reduced to a system of ordinary differential equations in terms of a new set of generalized coordinates.

The first two generalized coordinates correspond exactly to the rigid-body degrees of freedom, or

$$w_C(t) = q_1(t), \quad \psi_C(t) = q_2(t) \tag{3.10a,b}$$

On the other hand, the elastic wing displacements are expressed as a series of trial functions multiplied by generalized coordinates, or

$$w(x,y,t)=\sum_{i=3}^{n+2}\phi_i(x,y)q_i(t)\equiv\phi_3^Tq_3$$
$$\psi_x(x,y,t)=\sum_{i=n+3}^{2n+2}\phi_i(x,y)q_i(t)\equiv\phi_4^Tq_4 \qquad (3.11a,b,c)$$
$$\psi_y(x,y,t)=\sum_{i=2n+3}^{3n+2}\phi_i(x,y)q_i(t)\equiv\phi_5^Tq_5$$

where ϕ_i and q_i (i = 3,4,5) are n-vectors of trial functions and generalized coordinates, respectively. The discrete system equations of motion are derived by substitution of Eqs. (3.10) and (3.11) directly into the extended Hamilton's principle, Eq. (3.9). For the integral in Eq. (3.9) to be equal to zero, the integrand must be equal to zero. But, the virtual displacements are arbitrary and independent, so that the equations of motion can be obtained by setting the coefficient of each of the virtual displacements to zero, or

$$M_C\ddot{q}_1+\int_{A_p}\left\{m_p\phi_3^T\ddot{q}_3+C\left(q_2+\phi_{3,x}^Tq_3\right)+\tfrac{c}{U}\left[\dot{q}_1+(x-x_C)\dot{q}_2+\phi_3^T\dot{q}_3\right]\right\}dA_p=0 \qquad (3.12a)$$

$$I_C\ddot{q}_2+\int_{A_p}(x-x_C)\left\{m_p\phi_3^T\ddot{q}_3+C\left(q_2+\phi_{3,x}^Tq_3\right)+\tfrac{c}{U}\left[\dot{q}_1+(x-x_C)\dot{q}_2+\phi_3^T\dot{q}_3\right]\right\}dA_p=0 \qquad (3.12b)$$

$$\begin{aligned}\int_{A_p}\Big\{&m_p\left[\phi_3\ddot{q}_1+(x-x_C)\phi_3\ddot{q}_2+\phi_3\phi_3^T\ddot{q}_3\right]+C\phi_3q_2+\tfrac{c}{U}\left[\phi_3\dot{q}_1+(x-x_C)\phi_3\dot{q}_2+\phi_3\phi_3^T\dot{q}_3\right]\\&+\left[C\phi_3\phi_3^T+A_{44}\phi_{3,y}\phi_{3,y}^T+A_{45}\left(\phi_{3,y}\phi_{3,x}^T+\phi_{3,x}\phi_{3,y}^T\right)+A_{55}\phi_{3,x}\phi_{3,x}^T\right]q_3\\&+\left[A_{45}\phi_{3,y}\phi_4^T+A_{55}\phi_{3,x}\phi_4^T\right]q_4+\left[A_{44}\phi_{3,y}\phi_5^T+A_{45}\phi_{3,x}\phi_5^T\right]q_5\Big\}dA_p=0\end{aligned} \qquad (3.12c)$$

$$\begin{aligned}\int_{A_p}\Big\{&I_p\phi_4\phi_4^T\ddot{q}_4+\left[A_{55}\phi_4\phi_4^T+D_{11}\phi_{4,x}\phi_{4,x}^T+D_{66}\phi_{4,y}\phi_{4,y}^T+D_{16}\left(\phi_{4,x}\phi_{4,y}^T+\phi_{4,y}\phi_{4,x}^T\right)\right]q_4\\&+\left[A_{45}\phi_4\phi_5^T+D_{12}\phi_{4,x}\phi_{5,y}^T+D_{16}\phi_{4,x}\phi_{5,x}^T+D_{26}\phi_{4,y}\phi_{5,y}^T+D_{66}\phi_{4,y}\phi_{5,x}^T\right]q_5\\&+\left[A_{45}\phi_4\phi_{3,y}^T+A_{55}\phi_4\phi_{3,x}^T\right]q_3-\left[d_{31}F_{11}+d_{32}F_{12}\right]\phi_{4,x}\Big\}dA_p=0\end{aligned} \qquad (3.12d)$$

$$\int_{A_p}\Big\{I_p\phi_5\phi_5^T\ddot{q}_5+\Big[A_{44}\phi_5\phi_5^T+D_{22}\phi_{5,y}\phi_{5,y}^T+D_{66}\phi_{5,x}\phi_{5,x}^T+D_{26}\Big(\phi_{5,x}\phi_{5,y}^T+\phi_{5,y}\phi_{5,x}^T\Big)\Big]q_5$$

$$+\Big[A_{45}\phi_5\phi_4^T+D_{12}\phi_{5,y}\phi_{4,x}^T+D_{16}\phi_{5,x}\phi_{4,x}^T+D_{26}\phi_{5,y}\phi_{4,y}^T+D_{66}\phi_{5,x}\phi_{4,y}^T\Big]q_4$$

$$+\Big[A_{44}\phi_5\phi_{3,y}^T+A_{45}\phi_5\phi_{3,x}^T\Big]q_3-\Big[d_{31}F_{12}+d_{32}F_{22}\Big]\phi_{5,y}\Big\}dA_p=0 \qquad (3.12e)$$

Recall that q_3, q_4 and q_5 are n-vectors of generalized coordinates, so that each of Eqs. (3.12) represents n coupled ordinary differential equations. The system equations of motion are expressed in a more convenient fashion through the use of partitioned matrices, as follows:

$$\left[\begin{array}{cc|c|c|c} M_{11} & 0 & M_{13} & 0 & 0 \\ 0 & M_{22} & M_{23} & 0 & 0 \\ \hline M_{31} & M_{32} & M_{33} & 0 & 0 \\ \hline 0 & 0 & 0 & M_{44} & 0 \\ \hline 0 & 0 & 0 & 0 & M_{55} \end{array}\right]\left\{\begin{array}{c} \ddot{q}_1 \\ \ddot{q}_2 \\ \hline \ddot{q}_3 \\ \hline \ddot{q}_4 \\ \hline \ddot{q}_5 \end{array}\right\}+\left[\begin{array}{cc|c|c|c} H_{A_{11}} & H_{A_{12}} & H_{A_{13}} & 0 & 0 \\ H_{A_{21}} & H_{A_{22}} & H_{A_{23}} & 0 & 0 \\ \hline H_{A_{31}} & H_{A_{32}} & H_{A_{33}} & 0 & 0 \\ \hline 0 & 0 & 0 & 0 & 0 \\ \hline 0 & 0 & 0 & 0 & 0 \end{array}\right]\left\{\begin{array}{c} \dot{q}_1 \\ \dot{q}_2 \\ \hline \dot{q}_3 \\ \hline \dot{q}_4 \\ \hline \dot{q}_5 \end{array}\right\}$$

$$+\left[\begin{array}{cc|c|c|c} 0 & K_{A_{12}} & K_{A_{13}} & 0 & 0 \\ 0 & K_{A_{22}} & K_{A_{23}} & 0 & 0 \\ \hline 0 & K_{A_{32}} & K_{A_{33}} & 0 & 0 \\ \hline 0 & 0 & 0 & 0 & 0 \\ \hline 0 & 0 & 0 & 0 & 0 \end{array}\right]\left\{\begin{array}{c} q_1 \\ q_2 \\ \hline q_3 \\ \hline q_4 \\ \hline q_5 \end{array}\right\}+\left[\begin{array}{cc|c|c|c} 0 & 0 & 0 & 0 & 0 \\ 0 & 0 & 0 & 0 & 0 \\ \hline 0 & 0 & K_{33} & K_{34} & K_{35} \\ \hline 0 & 0 & K_{43} & K_{44} & K_{45} \\ \hline 0 & 0 & K_{53} & K_{54} & K_{55} \end{array}\right]\left\{\begin{array}{c} q_1 \\ q_2 \\ \hline q_3 \\ \hline q_4 \\ \hline q_5 \end{array}\right\}=\left\{\begin{array}{c} 0 \\ 0 \\ \hline \mathbf{0} \\ \hline Q_4 \\ \hline Q_5 \end{array}\right\} \qquad (3.13)$$

where M is the symmetric mass matrix having the submatrices

$$M_{11}=M_C,\quad M_{22}=I_C,\quad M_{33}=\int_{A_p}m_p\phi_3\phi_3^T dA_p \qquad (3.14a,b,c)$$

$$M_{13}=\int_{A_p}m_p\phi_3^T dA_p,\qquad M_{23}=\int_{A_p}m_p(x-x_C)\phi_3^T dA_p \qquad (3.14d,e)$$

$$M_{44}=\int_{A_p}m_p\phi_4\phi_4^T dA_p,\qquad M_{55}=\int_{A_p}m_p\phi_5\phi_5^T dA_p \qquad (3.14f,g)$$

K is the symmetric elastic stiffness matrix having the submatrices

$$K_{33}=\int_{A_p}\Big[A_{44}\phi_{3,y}\phi_{3,y}^T+A_{45}\Big(\phi_{3,y}\phi_{3,x}^T+\phi_{3,x}\phi_{3,y}^T\Big)+A_{55}\phi_{3,x}\phi_{3,x}^T\Big]dA_p \qquad (3.15a)$$

$$K_{34} = \int_{A_p} \left[A_{45}\phi_{3,y}\phi_4^T + A_{55}\phi_{3,x}\phi_4^T \right] dA_p, \quad K_{35} = \int_{A_p} \left[A_{44}\phi_{3,y}\phi_5^T + A_{45}\phi_{3,x}\phi_5^T \right] dA_p \qquad (3.15b,c)$$

$$K_{44} = \int_{A_p} \left[A_{55}\phi_4\phi_4^T + D_{11}\phi_{4,x}\phi_{4,x}^T + D_{66}\phi_{4,y}\phi_{4,y}^T + D_{16}\left(\phi_{4,x}\phi_{4,y}^T + \phi_{4,y}\phi_{4,x}^T\right) \right] dA_p \qquad (3.15d)$$

$$K_{45} = \int_{A_p} \left[A_{45}\phi_4\phi_5^T + D_{12}\phi_{4,x}\phi_{5,y}^T + D_{16}\phi_{4,x}\phi_{5,x}^T + D_{26}\phi_{4,y}\phi_{5,y}^T + D_{66}\phi_{4,y}\phi_{5,x}^T \right] dA_p \qquad (3.15e)$$

$$K_{55} = \int_{A_p} \left[A_{44}\phi_5\phi_5^T + D_{22}\phi_{5,y}\phi_{5,y}^T + D_{66}\phi_{5,x}\phi_{5,x}^T + D_{26}\left(\phi_{5,x}\phi_{5,y}^T + \phi_{5,y}\phi_{5,x}^T\right) \right] dA_p \qquad (3.15f)$$

K_A is the nonsymmetric aerodynamic stiffness matrix with submatrices given by

$$K_{A_{12}} = \int_{A_p} C dA_p, \quad K_{A_{13}} = \int_{A_p} C\phi_{3,x}^T dA_p, \quad K_{A_{22}} = \int_{A_p} C(x - x_C) dA_p \qquad (3.16a,b,c)$$

$$K_{A_{23}} = \int_{A_p} C(x - x_C)\phi_{3,x}^T dA_p, \quad K_{A_{32}} = \int_{A_p} C\phi_3 dA_p, \quad K_{A_{33}} = \int_{A_p} C\phi_3\phi_{3,x}^T dA_p \qquad (3.16d,e,f)$$

and H_A is a symmetric aerodynamic damping matrix with submatrices given by

$$H_{11} = \int_{A_p} \frac{C}{U} dA_p, \quad H_{12} = \int_{A_p} \frac{C}{U}(x - x_C) dA_p, \quad H_{13} = \int_{A_p} \frac{C}{U}\phi_3^T dA_p \qquad (3.17a,b,c)$$

$$H_{22} = \int_{A_p} \frac{C}{U}(x - x_C)^2 dA_p, \quad H_{23} = \int_{A_p} \frac{C}{U}(x - x_C)\phi_3^T dA_p, \quad H_{33} = \int_{A_p} \frac{C}{U}\phi_3\phi_3^T dA_p \qquad (3.17d,e,f)$$

The n-vectors of generalized actuator forces, Q_4 and Q_5, have the form

$$Q_4 = \int_{A_p} (d_{31}F_{11} + d_{32}F_{12})\phi_{4,x} dA_p, \quad Q_5 = \int_{A_p} (d_{31}F_{12} + d_{32}F_{22})\phi_{5,y} dA_p \qquad (3.18a,b)$$

where the actuation voltage is included implicitly through the previously defined piezoelectric stiffness coefficients, F_{ab}. It will prove useful to express the generalized actuator forces explicitly in terms of the control voltages. To this end, we introduce Eqs. (2.17) and (2.23) into Eqs. (3.18) and write

$$Q(t)=\left\{\begin{array}{c}0\\0\\\hline 0\\\hline Q_4\\\hline Q_5\end{array}\right\}=\left[\begin{array}{c}0\\0\\\hline 0\\\hline \hat{B}_4\\\hline \hat{B}_5\end{array}\right]v_c(t)\equiv\hat{B}v_c(t) \tag{3.19}$$

where $\hat{B}$ is an actuator participation matrix whose nxm submatrices take the form

$$\begin{aligned}\hat{B}_4&=\tfrac{1}{2}\int_{A_p}(h_{k+1}+h_k)\left(d_{31}Q_{p_{11}}+d_{32}Q_{p_{12}}\right)\phi_{4,x}\boldsymbol{R}_p^T dA_p\\ \hat{B}_5&=\tfrac{1}{2}\int_{A_p}(h_{k+1}+h_k)\left(d_{31}Q_{p_{12}}+d_{32}Q_{p_{22}}\right)\phi_{5,y}\boldsymbol{R}_p^T dA_p\end{aligned} \tag{3.20a,b}$$

The matrix equations of motion represent $3n+2$ ordinary second-order differential equations of motion coupled through the mass, stiffness, aerodynamic stiffness and aerodynamic damping matrices. Both K_A and H_A are airspeed dependent. In addition, the aerodynamic stiffness matrix is nonsymmetric, thus rendering the problem non-self-adjoint (Ref. 97).

The accuracy and convergence of the solution of the governing equations, Eqs. (3.13), depends on the choice of trial functions in the discretization procedure. The nature of the trial functions used in the present application will be discussed in the next chapter. In addition, the accuracy and convergence of the approximate solution will be examined for both the free vibration (*in vacuo*) and flutter eigenvalue problems. In the remainder of this chapter, the system equations will be completed with a derivation of the system output equations, relating voltage measurements from piezoelectric sensors to the dynamic state of the wing.

3.4 Sensor Output Equations

When a piezoelectric patch undergoes deformation, a measurable voltage accumulates within the material. This phenomenon is a result of the polarity of

the crystals within the piezoelectric material and is known as the direct piezoelectric effect. Such voltages are easily measured when piezoelectric patches are equipped with surface mounted electrodes (Fig. 2.5). The deformation of a sensing patch mounted on a host structure, in this case the flexible aircraft wing, is directly related to the deformation of the host. Thus a relationship exists between the voltage output of the sensor and the variables corresponding to the plate deformation.

The piezoelectric sensor and actuator patches are modeled as isotropic surface-mounted plies. The constitutive equations relating an externally applied voltage to stress and strain in the material were introduced Chapter 2 for the derivation of the actuation strain energy. For sensing applications, there is no externally applied voltage and Eqs. (2.14) take the form

$$\begin{Bmatrix} \sigma_x \\ \sigma_y \end{Bmatrix}_p = \begin{bmatrix} Q_{11} & Q_{12} \\ Q_{21} & Q_{22} \end{bmatrix}_p \begin{Bmatrix} \varepsilon_x \\ \varepsilon_y \end{Bmatrix}_p \tag{3.21}$$

where all quantities have been previously defined. In addition, a second set of constitutive equations governs the relationship between stress in the material and electric displacement, defined as the charge per unit area developed under applied stress. When stresses occur primarily in the x-y plane, as in the present case, the only electric displacement and corresponding voltage produced is in the direction normal to the plane. Under the condition of zero external voltage, the relationship between the electric displacement and the stresses in the material is given by

$$D_3 = d_{31}\sigma_x + d_{32}\sigma_y = \begin{Bmatrix} d_{31} \\ d_{32} \end{Bmatrix}^T \begin{Bmatrix} \sigma_x \\ \sigma_y \end{Bmatrix}_p \tag{3.22}$$

where D_3 is the electric displacement and d_{3i} are piezoelectric material constants defined earlier.

It can be shown (Ref. 112) that the use of electrodes on the upper and lower surfaces of a piezoelectric sensor patch for voltage measurement is equivalent to an averaging of the stress (or strains) through the thickness of the material. In terms of the wing layer height notation, the average strain occurs at a height of $z = z_c = \frac{1}{2}(h_k + h_{k+1})$, which is the perpendicular distance from the mid-plane of the wing to the center of the sensor patch. Using this height in the strain displacement relations, Eqs. (2.7a,b), yields the average strains

$$\begin{Bmatrix} \varepsilon_x \\ \varepsilon_y \end{Bmatrix}_p = z_c \begin{Bmatrix} \psi_{x,x} \\ \psi_{y,y} \end{Bmatrix} \tag{3.23}$$

which, when substituted along with Eq. (3.21) into (3.22) relates the electric displacement to the wing displacement variables, or

$$D_3 = z_c \begin{Bmatrix} d_{31} \\ d_{32} \end{Bmatrix}^T \begin{bmatrix} Q_{11} & Q_{12} \\ Q_{21} & Q_{22} \end{bmatrix}_p \begin{Bmatrix} \psi_{x,x} \\ \psi_{y,y} \end{Bmatrix} \tag{3.24}$$

Note that the electric displacement is related not to the plate transverse displacement, but instead to the rotational displacement variables, which under first-order shear deformation theory are independent degrees of freedom. This result parallels the actuator derivation in Chapter 2, where it was pointed out that the net effect of voltage-induced strain was to produce generalized moments acting through the rotational degrees of freedom.

The total charge developed on the surfaces of the sensor element is found through integration of the electric displacement over the element area, or

$$q_s(t) = \int_{patch} D_i n_i dA = \int_{y_1}^{y_2}\int_{x_1}^{x_2} z_c \begin{Bmatrix} d_{31} \\ d_{32} \end{Bmatrix}^T \begin{bmatrix} Q_{11} & Q_{12} \\ Q_{21} & Q_{22} \end{bmatrix}_p \begin{Bmatrix} \psi_{x,x} \\ \psi_{y,y} \end{Bmatrix} dxdy \tag{3.25}$$

and the corresponding voltage measured across the sensor electrodes is given by

$$v_s(t) = \int_{y_1}^{y_2}\int_{x_1}^{x_2} \frac{z_c}{C^s} \begin{Bmatrix} d_{31} \\ d_{32} \end{Bmatrix}^T \begin{bmatrix} Q_{11} & Q_{12} \\ Q_{21} & Q_{22} \end{bmatrix}_p \begin{Bmatrix} \psi_{x,x} \\ \psi_{y,y} \end{Bmatrix} dxdy \tag{3.26}$$

where C^s is the equivalent capacitance of the patch, which depends on the patch area A_a and thickness t_a as well as the permittivity of the piezoelectric material, ξ_{33}^s, according to

$$C^s = \frac{\xi_{33}^s A_a}{t_a} \tag{3.27}$$

The limits of integration in Eqs. (3.25 & 3.26) correspond to patch placement coordinates, and are shown in Fig. 2.6.

Any control design must be based on the discretized system equations of motion. Thus, the sensor output voltage must be expressed in terms of the discrete system generalized coordinates. Introduction of the elastic displacement variable series expansions, Eqs. (3.11b,c), yields the output equation relating the voltage measurement from one patch to the plate generalized coordinates

$$v_s(t) = \int_{y_1}^{y_2}\int_{x_1}^{x_2} \frac{z_c}{C^s} \begin{Bmatrix} d_{31} \\ d_{32} \end{Bmatrix}^T \begin{bmatrix} Q_{11} & Q_{12} \\ Q_{21} & Q_{22} \end{bmatrix}_p \begin{Bmatrix} \phi_{4,x}^T q_4 \\ \phi_{5,y}^T q_5 \end{Bmatrix} dxdy \tag{3.28}$$

where $\phi_4(x,y)$ and $\phi_5(x,y)$ are the vectors of trial functions defined previously. If we consider m sensor patches, the output voltage vector is easily written in the standard output form

$$v_s(t) = \begin{Bmatrix} v_{s1} \\ v_{s2} \\ \vdots \\ v_{sm} \end{Bmatrix} = \left[0 \quad 0 \mid \mathbf{0} \mid \hat{C}_4 \mid \hat{C}_5 \right] \left\{ \begin{array}{c} q_1 \\ \hline q_2 \\ \hline q_3 \\ \hline q_4 \\ \hline q_5 \end{array} \right\} \equiv \hat{C} q(t) \tag{3.29}$$

where $\hat{C}$ is a sensor participation matrix whose m x n submatrices are functions of the piezoelectric material properties, sensor placement and trial functions, with rows given by

$$\begin{aligned} \hat{C}_{4_i} &= \frac{\left(d_{31}Q_{p_{11}} + d_{32}Q_{p_{12}}\right)_i}{C_i^s} \int_{y_1}^{y_2} \int_{x_1}^{x_2} z_{c_i} \phi_{4,x}^T dx_i dy_i \quad i = 1, m \\ \hat{C}_{5_i} &= \frac{\left(d_{31}Q_{p_{12}} + d_{32}Q_{p_{22}}\right)_i}{C_i^s} \int_{y_1}^{y_2} \int_{x_1}^{x_2} z_{c_i} \phi_{5,y}^T dx_i dy_i \quad i = 1, m \end{aligned} \tag{3.30}$$

It is obvious from the nature of the participation matrix that the voltage outputs are mathematically proportional to linear combinations of the plate generalized rotation coordinates.

CHAPTER 4

FREE VIBRATION AND FLUTTER ANALYSIS

In this chapter, we propose to solve the eigenvalue problem associated with Eq. (3.13) first for the case of free vibration (zero airspeed) and also for in-flight conditions. The free vibration eigenvalue problem yields the *in vacuo* natural frequencies and mode shapes of the wing, while the in-flight eigenvalue problem is solved at a series of increasing airspeeds in an effort to determine the flutter airspeed and the flutter mechanism.

In the previous chapter, we derived a discrete system of equations to model a physically distributed wing. The algebraic eigenvalue problem associated with the discrete system is therefore only an approximation. The computational speed and accuracy of the discretized solution depends on the nature of the trial functions used in approximating the continuous elastic displacements, Eq. (3.11).

4.1 Trial Functions

There are generally three classes of functions available for use as trial functions, including *eigenfunctions*, *comparison functions* and *admissible functions*. Eigenfunctions are generated by exact, closed-form solutions of differential eigenvalue problems, and as such they satisfy the governing differential equations as well as all the problem boundary conditions exactly. For realistic continuous systems, very few closed-form eigensolutions exist. A slightly broader class of trial functions which satisfy all the problem boundary conditions, but not necessarily the differential equations, are known as comparison functions (Ref. 97). However, comparison functions are often difficult to generate as natural boundary conditions can be quite complicated.

The broadest class of trial functions, admissible or shape functions, need satisfy only certain differentiability constraints and the problem geometric boundary conditions (Ref. 97). While admissible functions are relatively easy to generate, convergence of approximate solutions in terms of admissible functions sometimes converge very slowly, resulting in increased computation time.

For non-self-adjoint systems, such as the aircraft wing model under consideration, the trial functions are generally from the class of comparison functions (Ref. 97). However, the wing model is subject to natural boundary conditions at the three free edges, which are further complicated by the fact that the leading and trailing edges are functions of both x and y. Hence, comparison functions are not feasible here. Instead, we do the next best thing and choose the trial functions as linear combinations of admissible functions from several different families (Ref. 107). The basic premise behind this approach is that a variety of admissible functions will have a better chance of containing all the characteristics necessary to satisfy the natural boundary conditions and the differential equations to any desired degree of accuracy. As it turns out, combinations of admissible functions have been shown to exhibit faster convergence than both admissible functions from a single family and comparison functions for self-adjoint and non-self-adjoint systems (Refs. 107,108).

For the problem at hand, half of the trial functions are chosen as trigonometric functions and half as power series. In expansion (3.11) the displacement fields are approximated as linear combinations of the trial functions with the generalized coordinates serving as undetermined coefficients. Thus, the trial functions must depend on both x and y, and are assumed to have the form

of products of chordwise functions $X_{k_f}(x)$ and spanwise functions $Y_{l_f}(y)$. There are a total of $3n+2$ trial functions needed for the approximate solution, n functions for each of the three elastic displacements and one for each of the rigid-body modes, namely $\phi_1 = \phi_2 = 1$. The same functions are used for each of the displacement fields and they take the form (Ref. 109)

$$\phi_f(x,y) = X_{k_f}(x)Y_{l_f}(y), \quad 1 \le f \le n \tag{4.1a}$$

where

$$f = i - 2 - n \bullet INT\left(\frac{i-2}{n}\right), \quad i = 3,4,5,\ldots,3n+2 \tag{4.1b}$$

and *INT()* implies truncation to the nearest integer value.

The interest lies in modeling low aspect ratio wings, which in turn implies that chordwise and spanwise modes are of about equal importance. Thus, in determining the order of combination for the functions $X_{k_f}(x)$ and $Y_{l_f}(y)$ into $\phi_f(x,y)$, the desire is to choose the coefficients k_f and l_f such that the spanwise and chordwise functions are about equal in number. The dependence of k_f and l_f on f is given by

$$\begin{aligned} l_f &= f - \tfrac{1}{2}(d^2 - d), && f = 1,2,3,\ldots,\frac{n}{2} \\ l_f &= \tfrac{1}{2}(2f - n - d^2 + d), && f = \frac{n}{2}+1,\frac{n}{2}+2,\ldots,n \\ k_f &= 1 - d - l_f, && f = 1,2,3,\ldots,n \end{aligned} \tag{4.2a,b,c}$$

where

$$\begin{aligned} d &= NINT\sqrt{2f}, && f = 1,2,3,\ldots,\frac{n}{2} \\ d &= NINT\sqrt{2f-n}, && f = \frac{n}{2}+1,\frac{n}{2}+2,\ldots,n \end{aligned} \tag{4.3a,b}$$

In Eqs. (4.2) and (4.3), n is assumed to be an even integer and *NINT()* indicates rounding to the nearest integer value.

Half of the functions $X_{k_f}(x)$ and $Y_{l_f}(y)$ are chosen as segments of sine functions with an appropriate number of zero crossings. The members of the first family of spanwise functions have the form

$$Y_{l_f}(y) = \frac{y}{s}\sin\left[\frac{(2l_f - 1)\pi}{2s}y\right], \quad 0 \le y \le s \tag{4.4}$$

where the sine function has been multiplied by y/s to ensure satisfaction of the geometric boundary conditions at $y=0$, in which s is the semi-span length. For the general trapezoidal wing planform of Fig. 2.3, the leading and trailing edges vary along the y direction. Taking this variation into account, the first family of chordwise functions actually depend on both x and y, and are given by

$$X_{k_f}(x,y) = \sin\left\{\frac{3\pi}{4} + \pi\left(k_f - \frac{3}{2}\right)\left[\frac{x - y\tan\eta_L}{r - y(\tan\eta_L - \tan\eta_T)}\right]\right\}, \quad LE \le x \le TE \tag{4.5}$$

where η_L and η_T are the leading and trailing edge sweep angles, respectively, and r is the wing root length.

The members of the second family of chordwise functions are chosen as terms from a power series, once again shifted to account for leading and trailing edge sweep. In addition, the functions are designed to alternate direction between the leading and trailing edges, resulting in

$$X_{k_f}(x,y) = \left\langle \tfrac{1}{2}\left\{r\left[1 + (-1)^{k_f}\right] - (-1)^{k_f}x + \left[1 + (-1)^{k_f}\right](\tan\eta_T - \tan\eta_L)y\right\}\left[r + (\tan\eta_T - \tan\eta_L)y\right]\right\rangle^{INT\left(\frac{k_f+3}{2}\right)}, \quad LE \le x \le TE \tag{4.6}$$

The second family of spanwise functions is simply

$$Y_{l_f}(y) = \left(\frac{y}{s}\right)^{\left(\frac{l_f+3}{2}\right)}, \qquad 0 \le y \le s \tag{4.7}$$

The complete set of two-dimensional trial functions is expressed in terms of f, k_f and l_f as follows:

$$\begin{aligned}
\phi_f &= \frac{y}{s}\sin ay, \quad f = 3,4,\ldots,\frac{n+2}{2}, \quad k_f = 1 \\
\phi_f &= \frac{xy}{rs}\sin ay, \quad f = 3,4,\ldots,\frac{n+2}{2}, \quad k_f = 2 \\
\phi_f &= \frac{y}{s}\sin ay \sin\left(\frac{b+cx+dy}{r+ey}\right), \quad f = 3,4,\ldots,\frac{n+2}{2}, \quad k_f \ge 3
\end{aligned} \tag{4.8a,b,c}$$

$$\begin{aligned}
\phi_f &= \left(\frac{y}{s}\right)^N, \quad f = \frac{n+4}{2},\ldots,n, \quad k_f = 1 \\
\phi_f &= \frac{x}{r}\left(\frac{y}{s}\right)^N, \quad f = \frac{n+4}{2},\ldots,n, \quad k_f = 2 \\
\phi_f &= My^N\left[\frac{1}{2}(1-Q)+Q\left(\frac{x+py}{r+ey}\right)\right]^A, \quad f = \frac{n+4}{2},\ldots,n, \quad k_f \ge 3
\end{aligned} \tag{4.9a,b,c}$$

where

$$b = \frac{3r\pi}{4}, \quad e = \tan\eta_T - \tan\eta_L \tag{4.10a,b}$$

$$p = -\tan\eta_L, \quad a = \frac{(2l_f-1)\pi}{2s} \tag{4.10c,d}$$

$$c = \pi\left(k_f - \frac{3}{2}\right), \quad d = \pi\left[\frac{3}{4}e + \left(k_f - \frac{3}{2}\right)p\right] \tag{4.10e,f}$$

$$N = \frac{l_f+3}{2}, \quad M = \left(\frac{1}{s}\right)^N \tag{4.10g,h}$$

$$Q = -(-1)^{k_f}, \quad A = INT\left(\frac{k_f+1}{2}\right) \tag{4.10i,j}$$

4.2 State Space Formulation

The natural frequencies and mode shapes, as well as the flutter airspeed of the aircraft wing model, are calculated by solving algebraic eigenvalue problems associated with Eq. (3.13). As it turns out, the solution of the flutter eigenvalue problem requires that the system be cast in first-order form, known as state space form. The system equations of motion are transformed to the state space through introduction of the state vector, $\boldsymbol{x}(t)=\left[\boldsymbol{q}^T(t),\dot{\boldsymbol{q}}^T(t)\right]^T$. The equations of motion in terms of the state vector then take the form

$$\begin{aligned}\dot{\boldsymbol{x}}(t)&=A\boldsymbol{x}(t)+B\boldsymbol{v}_c(t)\\ \boldsymbol{v}_s(t)&=C\boldsymbol{x}(t)\end{aligned} \tag{4.11}$$

where

$$A=\begin{bmatrix}0 & I\\ -M^{-1}(K+K_A) & -M^{-1}H_A\end{bmatrix},\quad B=\begin{bmatrix}0\\ M^{-1}\hat{B}\end{bmatrix},\quad C=\begin{bmatrix}\hat{C} & 0\end{bmatrix} \tag{4.12a,b}$$

are coefficient matrices, $\boldsymbol{v}_c(t)$ is the vector of control voltages and $\boldsymbol{v}_s(t)$ is the output vector of sensor voltage measurements.

4.3 Free Vibration Eigenvalue Problem

Next, we propose to derive the eigenvalue problem associated with the system equations of motion in the form of Eq. (4.11). To this end, we drop the vector of control voltages and specify the time dependence of the state vector. Letting $\boldsymbol{x}(t)=\boldsymbol{X}e^{\lambda t}$, we arrive at the standard algebraic eigenvalue problem, or

$$A\boldsymbol{X}=\lambda\boldsymbol{X} \tag{4.13}$$

the solution of which consists of the system eigenvalues, λ, and corresponding eigenvectors, $\boldsymbol{X}$. Because the state matrix A is not symmetric, the eigenvalues are generally complex, taking the form

$$\lambda = \alpha \pm i\omega \tag{4.14}$$

with the real part indicating aerodynamic damping and the imaginary part the corresponding frequency.

For the free-vibration case, the system is conservative and the corresponding eigenvalue problem can be written in terms of real, symmetric matrices. Setting K_A, H_A and v_c equal to zero in Eq. (3.13), the equations of motion take the form

$$M\ddot{q} + Kq = 0 \tag{4.15}$$

where M is symmetric and positive definite and K is symmetric and positive semidefinite. The eigenvalue problem for Eq. (4.15) is arrived at in the usual manner, assuming harmonic time dependence for the configuration vector, $q(t) = \varphi e^{i\omega t}$, and has the standard form

$$\omega^2 M\varphi = K\varphi \tag{4.16}$$

in which the frequencies, ω, and corresponding eigenvectors, φ, are real quantities. Alternatively, if the first order form of Eq. (4.13) is used, the eigenvalues, λ, are pure imaginary, occurring in complex conjugate pairs.

To demonstrate the convergence and accuracy of the approximate solution, natural frequencies were calculated for two different models using increasing numbers of trial functions. The dimensions and material properties for the two models are given in Appendix A. The first model is a rectangular steel plate cantilevered along one edge, for which an exact solution is available (Ref. 110). The results are shown in Fig. 4.1 for the first three natural frequencies of the plate.

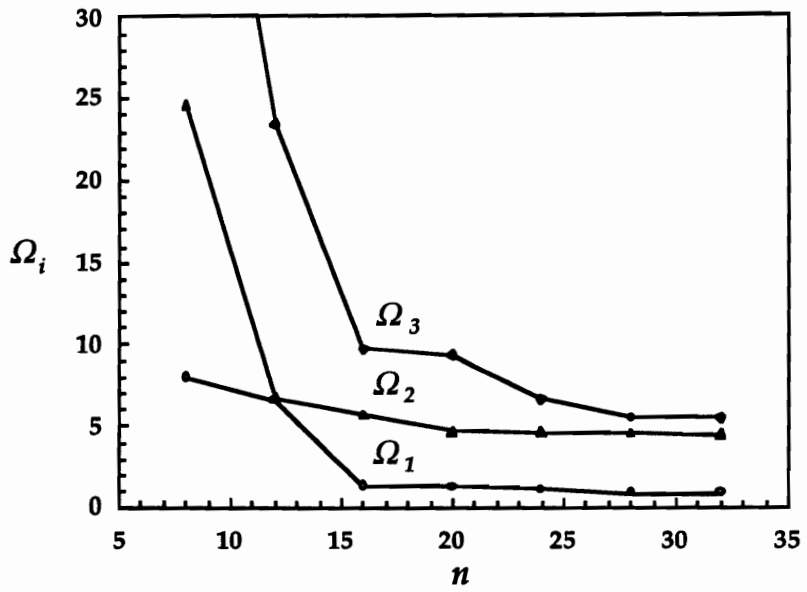

Fig. 4.1 - Nondimensional Natural Frequencies Versus Number of Trial Functions for Steel Cantilever Rectangular Plate

In Fig. 4.1, the frequency has been nondimensionalized according to

$$\Omega = \omega A_p \left[\frac{\rho}{E(2t_N)^2} \right]^{\frac{1}{2}} \tag{4.17}$$

where A_p is the plate area, E the Young's modulus, ρ the plate mass density and t_N the plate half-thickness. One can observe the nature of the admissible function approximation in Fig. 4.1. With just a few terms in the series expansions, the approximate solution vastly overpredicts the plate natural frequencies. However, as more terms are added to the expansions, the trial functions result in better approximation of both the natural boundary conditions and the differential equations. Thus, the calculated natural frequencies are seen to converge rather quickly. Table 4.1 shows a comparison between the three lowest computed and exact values of the nondimensional natural frequencies.

Table 4.1 - Nondimensional Natural Frequencies of Rectangular Steel Cantilever Plate

i	Computed Ω_i	Exact Ω_i
1	0.8808	0.8366
2	4.442	4.355
3	5.418	5.219

As can be concluded, the agreement is reasonably good considering the complexity of the model.

A study of the convergence properties of the second model, a graphite/epoxy forward-swept wing model, is shown in Fig. 4.2, where the natural frequencies correspond to the first five flexible modes of the wing. The rigid-body modes have zero frequency and converge immediately. The results in Fig. 4.2 indicate that we have good convergence for the first five flexible modes if twenty terms are used in each of the series expansions, Eqs. (3.11).

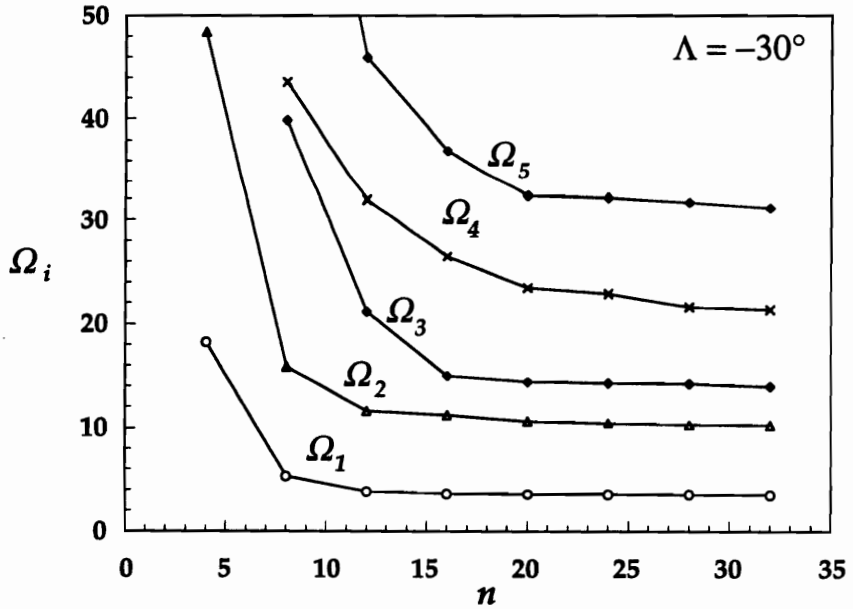

Fig. 4.2 - Nondimensional Natural Frequencies Versus Number of Trial Functions for Graphite/Epoxy Wing

4.4 Open-Loop Flutter Analysis

Flutter analysis consists of solving the eigenvalue problem associated with the airspeed-dependent state matrix A for a series of increasing airspeeds. As mentioned previously, for nonzero airspeeds the real parts of the eigenvalues indicate the amount of aerodynamic damping. For a stable system, each of the eigenvalues must have a negative real part. The first airspeed for which one of the system eigenvalues exhibits a zero real part is known as the open-loop flutter speed, the flight speed at which the system becomes unstable.

As an example, the flutter analysis was carried out for the graphite/epoxy wing model with 30° forward sweep and a fullspan aspect ratio of 3. The results are shown in Figs. 4.3 and 4.4, where the dynamic pressure has been nondimensionalized according to

$$\bar{q} = \frac{2qA_p^2}{E(2t_N)^4} = \frac{\rho_{air}U^2A_p^2}{E(2t_N)^4} \tag{4.18}$$

in which ρ_{air} is the air density and U the free stream airspeed; all other quantities have been defined previously. In Fig. 4.3, we see that the rigid-body pitch mode takes on a nonzero frequency that tends to increase with increasing dynamic pressure. Simultaneously, the frequency of the first flexible bending mode decreases. The damping associated with the rigid-body pitch and the first flexible bending modes is shown in Fig. 4.4. The pitch mode becomes more stable with increasing dynamic pressure, while simultaneously the first flexible bending mode tends toward instability. Hence, the flutter mechanism for this forward-swept wing configuration is clearly a coalescence of the rigid-body pitch and first flexible bending modes, known as *body-freedom flutter*.

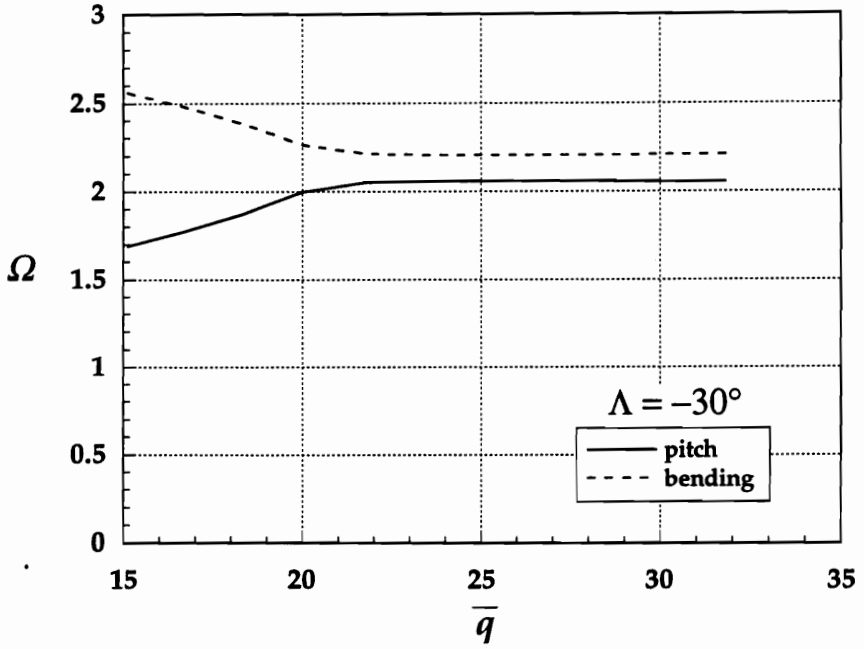

Fig. 4.3 - Pitch and Bending Frequencies Versus Nondimensional Dynamic Pressure for Forward-Swept Wing

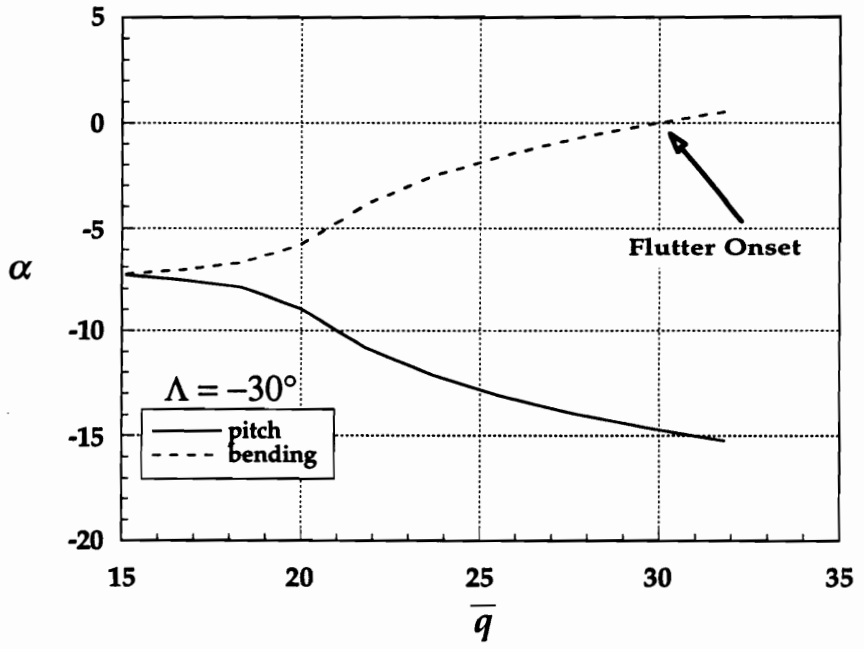

Fig. 4.4 - Eigenvalue Real Part Versus Nondimensional Dynamic Pressure for Forward-Swept Wing

As a further illustration of the capabilities of the aircraft wing model, a flutter investigation was carried out for the same graphite/epoxy forward-swept wing with the rigid-body degrees of freedom removed. The results are shown in Figs. 4.5 and 4.6. As the dynamic pressure is increased, the frequency of the first bending mode decreases until it eventually goes to zero (Fig. 4.5). At the same time, the real part of the eigenvalue crosses into the unstable region (Fig. 4.6). This behavior is known as *static divergence*, a special case of instability which occurs at zero frequency. Comparing Figs. 4.4 and 4.6, we see that the model predicts a higher instability speed when the body freedoms are removed. Thus, for this wing configuration, body-freedom flutter is the most critical aeroelastic instability. This finding follows the trends discovered by other researchers (Refs. 45-47) and demonstrates the necessity of including rigid-body motions in models of free-flying aircraft.

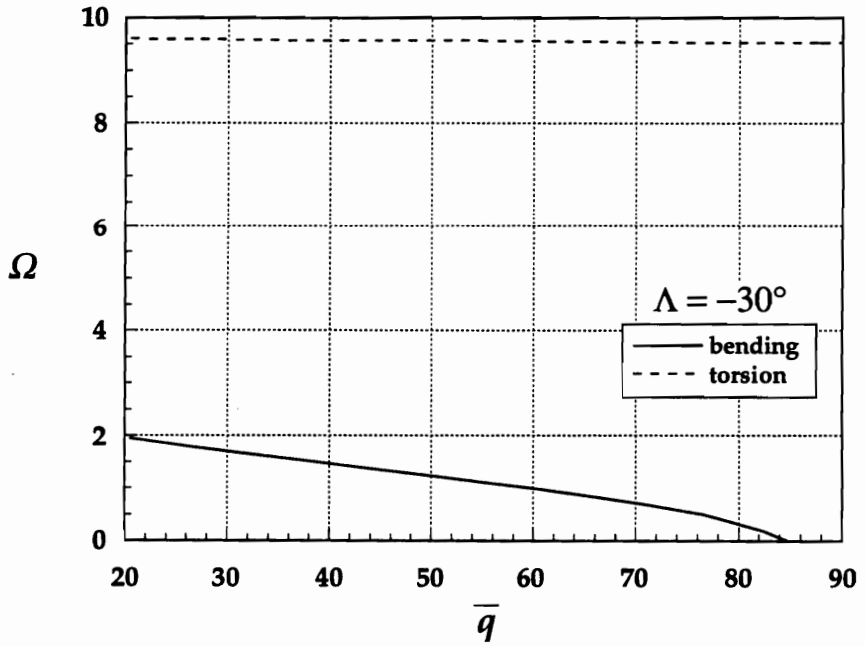

Fig. 4.5 - Nondimensional Frequencies Versus Nondimensional Dynamic Pressure for Clamped, Forward-Swept Wing

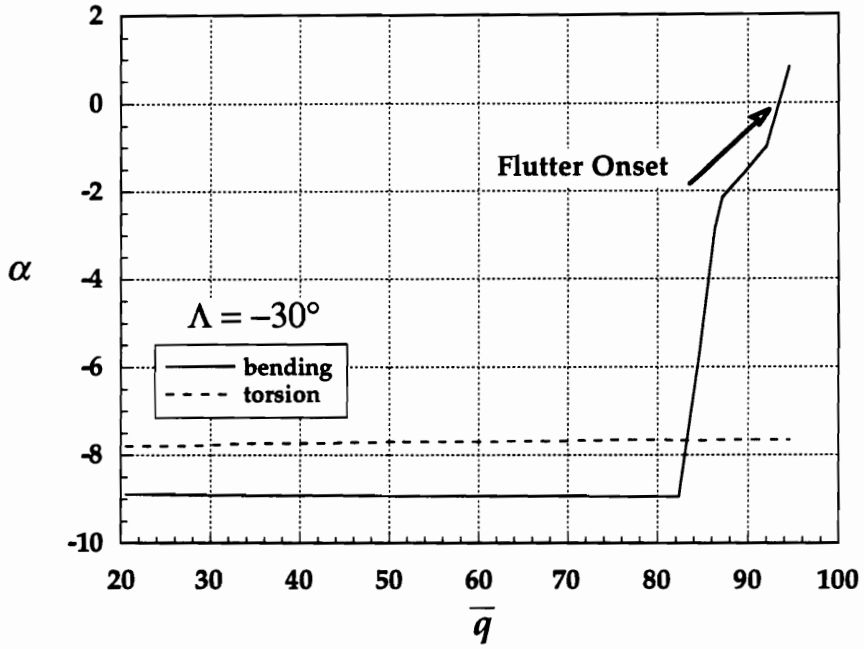

Fig. 4.6 - Eigenvalue Real Part Versus Nondimensional Dynamic Pressure for Clamped, Forward-Swept Wing

A third flutter investigation was carried out for the same flexible wing model, only in an aft-swept configuration (Λ = +30°). Nondimensional frequencies for the rigid-body pitch and first two flexible modes are shown as functions of nondimensional dynamic pressure in Fig. 4.7. For this configuration, the rigid-body pitch frequency changes only slightly with increasing dynamic pressure. On the other hand, the frequencies of the two flexible modes coalesce as the dynamic pressure increases. The damping values associated with the same three modes are shown in Fig. 4.8. Once again, as the frequencies coalesce one of the modes becomes more stable while the other one tends towards instability. The flutter mechanism for this aft-swept design is known as classical *bending-torsion flutter*. It occurs at dynamic pressures significantly higher than those corresponding to the forward-swept counterpart discussed earlier.

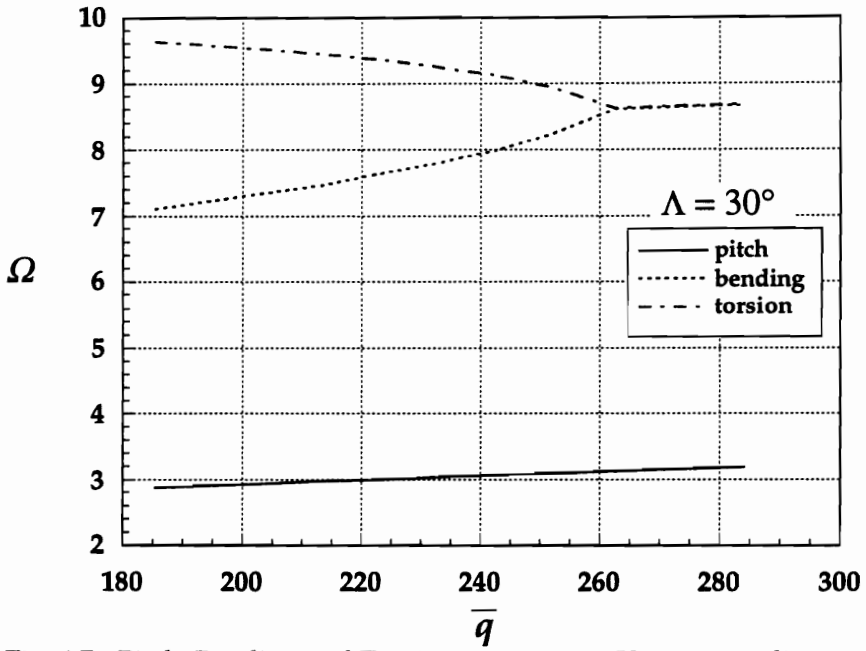

Fig. 4.7 - Pitch, Bending and Torsion Frequencies Versus Nondimensional Dynamic Pressure for Aft-Swept Wing

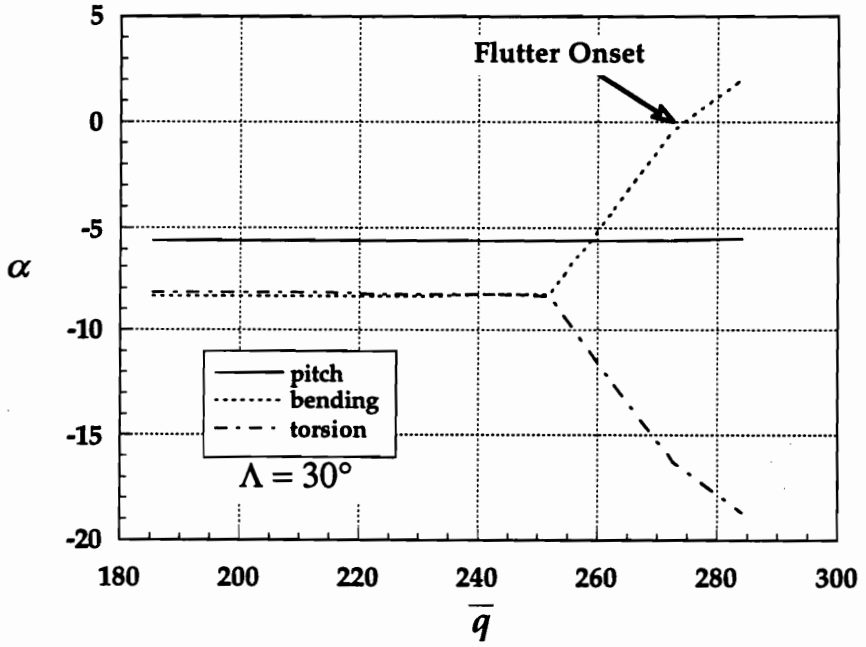

Fig. 4.8 - Eigenvalue Real Part Versus Nondimensional Dynamic Pressure for Aft-Swept Wing

Bending and torsion motions are coupled for swept-wing configurations. When a wing is swept back, the coupling tends to reduce the effective angle of attack of the wing, resulting in attenuated loading of the wing surface known as *wash-out*. It is a well-documented fact that wash-out delays the onset of divergence, which is replaced by body-freedom flutter in the present model, so that it is usually not the most critical instability for aft-swept wings. On the other hand, forward sweep causes adverse coupling between bending and torsion, known as *wash-in*, which tends to amplify the aerodynamic loading on the wing and significantly reduce the airspeed at which instability occurs.

It will prove useful to examine the effects of variation in wing parameters such as sweep angle on both flutter airspeed and flutter mechanism. In the interest of generality, both fixed wing and free-flying configurations were included as well as aerodynamic theories including (quasi-steady) and excluding (quasi-static) aerodynamic damping terms. The results, shown in Table 4.2, are useful for establishing trends and determining the most critical configurations.

Table 4.2 - Effects of Sweep Angle on Nondimensional Flutter Dynamic Pressure for Several Aircraft Models

	$\bar{q}_F$			
	FREE WING		FIXED WING	
Λ	quasi-static	quasi-steady	quasi-static	quasi-steady
-45°	7.38_{BFF}	12.11_{BFF}	16.9_{D}	17.6_{D}
-30°	21.3_{BFF}	30.1_{BFF}	94.3_{D}	93.2_{D}
-15°	99.2_{BFF}	147.8_{BFF}	551.8_{D}	641.3_{D}
0°	614.7_{BT}	635.7_{BT}	876.1_{BT}	887.9_{BT}
15°	382.4_{BT}	401.8_{BT}	522.7_{BT}	546.9_{BT}
30°	253.6_{BT}	274.5_{BT}	323.1_{BT}	347.3_{BT}
45°	203.8_{BT}	219.7_{BT}	220.2_{BT}	229.9_{BT}

BFF = body-freedom flutter, BT = classical bending-torsion flutter, D = static divergence

As seen in Table 4.2, forward-swept wing configurations result in drastically lower flutter dynamic pressures than their aft-swept counterparts. Also, when the wings are swept forward, the flutter mechanism is divergence for the fixed wing configuration and body-freedom flutter when rigid-body motions are modeled. Furthermore, the flutter dynamic pressures predicted for the fixed wing model are higher at each sweep angle (forward or aft) than for the free wing configuration. Thus, the need to include rigid-body motions in flutter modeling is once again justified.

Several interesting trends are discovered when we compare results using quasi-static and quasi-steady piston theory aerodynamic approximations. The quasi-static results are generated by omitting the virtual work terms containing derivatives with respect to time (Eq. 3.4), or consequently, eliminating the aerodynamic damping matrix in Eqs. (3.13 & 4.12a). Referring again to Table 4.2, we see that the inclusion of aerodynamic damping tends to increase the dynamic pressure at which flutter occurs. The most dramatic increases occur when body-freedom flutter is the critical instability. Furthermore, the increase in flutter speed is generally smaller for the fixed wing model and for both models in aft-swept positions.

Intuitively, one might expect aerodynamic damping terms to help stabilize a vibrating aircraft wing. However, as Dowell has pointed out (Ref. 102) this is not always the case. In fact, Dowell has shown that elimination of aerodynamic damping in a simple two degree-of-freedom model of a typical section wing resulted in a higher flutter airspeed. It should be pointed out that Dowell suggests this phenomena could be a characteristic of this specific model. In the present study, only one configuration, the fixed wing with 30° aft sweep,

demonstrated the same trends reported by Dowell. All other configurations experienced flutter at a lower airspeed when aerodynamic damping was not included.

The question of whether or not aerodynamic damping should be included in flutter modeling has been the subject of much debate in the past. Various models include either aerodynamic or structural damping, neither or both. One could make the argument that we have neglected structural damping in the present model and thus we should also neglect aerodynamic damping for the sake of consistency. We choose simply to investigate both possibilities.

When aerodynamic damping is neglected from the flutter modeling, the results provide insight into the true nature of the flutter mechanism. A comparison of flutter results for the 30° forward-swept G/E wing model using quasi-steady and quasi-static piston theory are shown in Figs. 4.9 and 4.10.

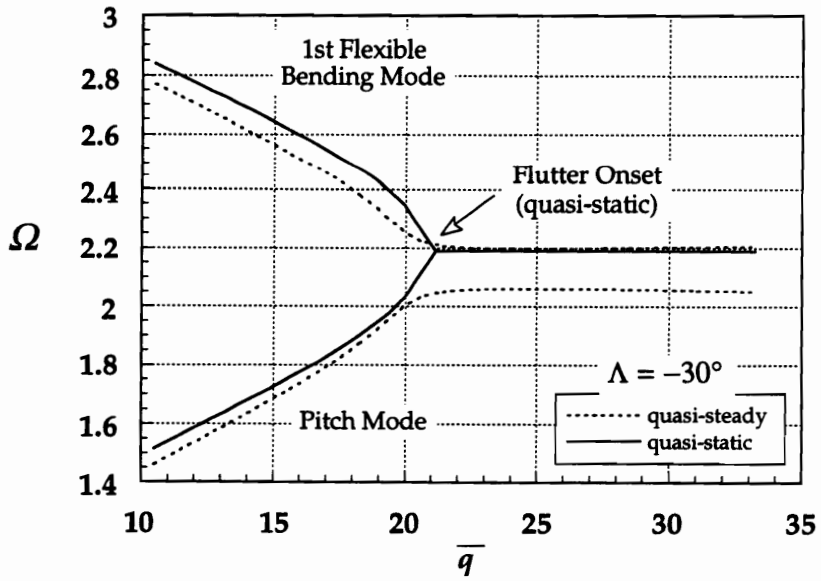

Fig. 4.9 - Effects of Aerodynamic Damping on Flutter Analysis

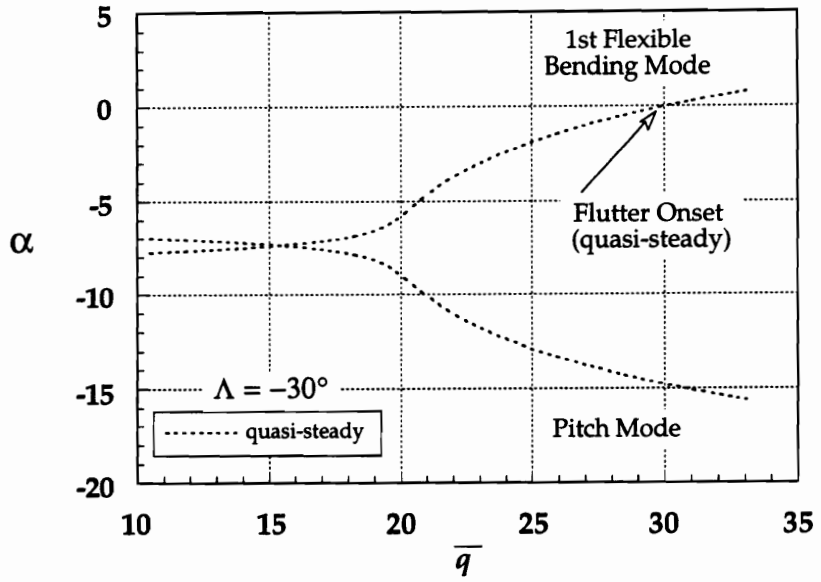

Fig. 4.10 - Effects of Aerodynamic Damping on Flutter Analysis

The flutter mechanism for this sweep angle is body-freedom flutter. With damping neglected, the aircraft pitching and wing bending modes are neutrally stable until the frequencies of the two modes coalesce (Fig. 4.9). On the other hand, we see that exact coalescence never occurs under the quasi-steady assumption. Instead, as the frequencies of the two modes converge, we begin to see adverse effects on the damping of the flexible mode (Fig. 4.10).

Since flutter occurs even when aerodynamic damping is excluded from the model, it is obvious that the phenomena is triggered by the effects of aerodynamic forces on the overall system stiffness matrix. The changes seen in modal damping when quasi-steady theory is used are a *result* of the frequency driven interaction between the two modes. Thus, altering the system stiffness matrix seems to be a logical approach to controlling or avoiding body-freedom flutter.

Certainly, one might attempt to control flutter by introducing additional damping into the system through the use of active controls. In fact, this approach has received much attention in the past (Refs. 13 - 31). However, in light of the above discussion, this approach seems tantamount to operating on the symptom instead of the disease. Instead, we propose that a more direct route to flutter control should include some means of altering the system frequencies. As pointed out in the Introduction, engineers have controlled different types of flutter in the past by adding stiffeners to wings and/or changing the mass distribution, both of which are passive means of altering the modal frequencies. A different approach to control of body-freedom flutter, namely, the use of active controls to alter wing bending frequencies (instead of damping) and delay interaction with the rigid-body pitch mode is explored in Chapter 5. However, first a method is developed in which only the model information pertinent to flutter analysis and control is retained in a reduced-order set of governing equations.

4.5 Modal Flutter Approximation

In the previous sections, the ability to accurately model three different flutter phenomena was demonstrated. The results indicate that only the first few modes participate in any of the flutter mechanisms, suggesting that a useful model need contain only the information pertinent to a few of the lower frequency modes. Also, due to the nature of the discretization process, the higher frequency modes are not accurate.

Significant savings in computation time may be achieved by eliminating the higher frequency modes from the model used for flutter analysis. Even with the rather complex trial functions used in this effort, the size of the system matrix

in Eq. (4.13) grows quite large before convergence of the first few free vibration frequencies is achieved, reaching 124 x 124 when twenty terms are used in each series expansion. As a result, the flutter solution is computationally expensive, especially considering that the eigenvalue problem is solved at each in a series of airspeeds. One method of reducing the large order of the system equations of motion is through *modal analysis* (Ref. 101), in which free vibration results are used to approximate the behavior of the system under aerodynamic loading.

Modal analysis is based on the assumption that the system response to external loading, in this case aerodynamic loading, can be represented by a small number N_f of the lower frequency free vibration modes. Mathematically, this assumption is equivalent to a truncated modal expansion given by

$$q(t) = \sum_{i=1}^{N_f} \varphi_i \eta_i \equiv \Phi_f \eta \tag{4.19}$$

where $\eta(t)$ is an N_f-vector of modal, or *natural*, coordinates and Φ_f is a matrix of the first N_f eigenvectors from the free vibration eigenvalue problem, Eq. (4.16). The eigenvectors are orthogonal, satisfying the relationships:

$$\Phi_f^T M \Phi_f = I, \qquad \Phi_f^T K \Phi_f = \Omega_f^2 \tag{4.20a,b}$$

in which I is the identity matrix and Ω_f is a diagonal matrix of the first N_f system natural frequencies. Substitution of Eq. (4.19) into Eqs. (3.13) and (3.29) and pre-multiplying by Φ_f^T yields the N_f equations of motion governing the modal coordinates, which are written as

$$\begin{aligned} &\ddot{\eta} + \overline{H}_A \dot{\eta} + \left[\Omega_f^2 + \overline{K}_A\right]\eta = \overline{B} v_c(t) \\ &v_s(t) = \overline{C}\eta(t) \end{aligned} \tag{4.21a,b}$$

where $\overline{H}_A = \Phi_f^T H_A \Phi_f$ is the modal aerodynamic damping matrix, $\overline{K}_A = \Phi_f^T K_A \Phi_f$ the modal aerodynamic stiffness matrix, $\overline{B} = \Phi_f^T \hat{B}$ the modal actuator participation matrix and $\overline{C} = \hat{C}\Phi_f$ the modal sensor participation matrix.

As in Section 4.3, the flutter eigenvalue problem associated with Eq. (4.21a) must be solved in the state space. Thus, we introduce the modal state vector, $\bar{x} = \begin{bmatrix} \eta^T & \dot{\eta}^T \end{bmatrix}^T$, and let $\bar{x}(t) = \overline{X} e^{\lambda t}$ to obtain the modal approximation to the flutter eigenvalue problem in the form

$$\begin{bmatrix} 0 & I \\ -(\Omega_f^2 + \overline{K}_A) & -\overline{H}_A \end{bmatrix} \overline{X} = \lambda \overline{X} \tag{4.22}$$

where $\overline{K}_A$ and $\overline{H}_A$ are still implicitly airspeed dependent.

A comparison of flutter results for the 30° forward-swept G/E wing using full-order, eight and four mode modal approximations is shown in Table 4.3.

Table 4.3 - Comparison of Modal and Full-Order Flutter Solutions

model	q_F (psi) quasi-static	q_F (psi) quasi-steady	CPU Time* (sec)
full-order	8.5986	12.378	125.0
8 mode	8.6034	12.384	2.76
4 mode	8.6154	12.424	1.41

* Flutter Solution in MATLAB® for 20 Airspeeds on a Power Macintosh® 9500

It can be seen that there is excellent agreement between the full-order and the approximate modal solutions, even when only four modes (two rigid + two flexible) are retained in the modal expansion. In addition, there is significant savings in computation time required for the modal approximation. The four mode solution is nearly ninety times faster than the full-order solution.

Computation speed is of particular interest if the model is eventually to be used as part of an overall design optimization package. In light of the above

comparison, we conclude that the modal flutter approximation does indeed capture all the necessary characteristics needed to accurately model the flutter mechanism. For these reasons, the reduced-order model will be utilized in the remainder of this study. In particular, the model will be used in the next chapter as a tool for investigating the feasibility of several control strategies aimed at increasing the aircraft flutter airspeed.

CHAPTER 5

FLUTTER SUPPRESSION METHODOLOGIES

In the previous chapters, a mathematical aircraft fuselage/wing model was developed as a useful tool intended for predesign stage of aircraft development. The versatility and usefulness of the model for investigating various aircraft configurations and their respective flutter mechanisms have been demonstrated in Chapter 4. In this chapter, the intent is to utilize this model in an investigation of strategies for increasing the flutter speed of a given aircraft configuration. Although the model is highly simplified compared to an actual aircraft configuration, the goal is to develop unique and novel flutter suppression approaches and to demonstrate trends which may carry over into the next design phase. Control designs will be demonstrated for the case of body-freedom flutter, as this was shown in Chapter 4 to be the most critical flutter mechanism for free flying forward-swept wing aircraft.

5.1 Control of Body-Freedom Flutter

In Chapter 4, the critical flutter mechanism for a graphite/epoxy wing in a 30° forward-swept configuration was shown to be body-freedom flutter. Body-freedom flutter involves a coalescence or merging of frequencies of the rigid-body pitch mode and the first flexible wing bending mode. The wing bending frequency decreases while at the same time the pitch mode takes on a nonzero frequency and increases with increasing airspeed. After the coalescence of the frequencies, the aerodynamic damping of the flexible mode tends towards the region of instability (see Figs. 4.3 & 4.4). If aerodynamic damping is not included in the model, then the point of coalescence defines the point of flutter onset (Fig. 4.9). The governing mechanism of this instability, frequency coalescence,

suggests a novel approach to flutter suppression. The basic premise is that delaying the frequency coalescence will delay the onset of instability, or flutter, to higher airspeeds, thus enlarging the aircraft's flight envelope.

Several possibilities exist for delaying coalescence of the aircraft's pitching and wing bending frequencies. From the flight control designer's point of view, the logical choice would be to control the predominantly rigid-body mode of the aircraft, thus altering the frequency of the pitch motion and delaying coalescence. However, for reasons stated in the literature review, solutions involving additional control surfaces or the use of pre-existing ailerons and flaperons are not desirable here, since these structures are often dedicated to other control objectives. From the aeroelastician's viewpoint, the more desirable approach to controlling body-freedom flutter would be to actuate the aeroelastic mode consisting mainly of flexible wing bending. Indeed, the present model, with surface mounted piezoelectric sensors and actuators is ideally suited for an investigation of the latter approach.

A hypothetical approach to increasing aircraft flutter speed is demonstrated in Fig. 5.1. For simplicity, aerodynamic damping has been neglected in the hypothetical flutter analysis. However, we recall that frequency coalescence triggers flutter whether or not damping is included. The idea is that delaying the onset of flutter to higher airspeeds simply amounts to widening the gap between the first wing flexible bending mode and the pitch mode. If we consider the zero airspeed, or free-vibration case, this simply amounts to finding a way of increasing the first natural frequency of the flexible wing. The frequency of the pitch mode will always be zero at zero airspeed. Thus, theoretically, increasing the frequency of the flexible wing bending mode will

cause the coalescence event (q_F^* on the graph) to occur at a higher airspeed. This is not an entirely new concept, as investigators have been adding stiffeners to wings for years to achieve the same effect. However, in the present study we are trying to avoid the undesirable weight gain typically associated with such solutions. Two techniques for increasing the frequency of the wing's first flexible bending mode will be investigated in the remainder of this chapter, namely composite material tailoring and active control via induced-strain sensors and actuators.

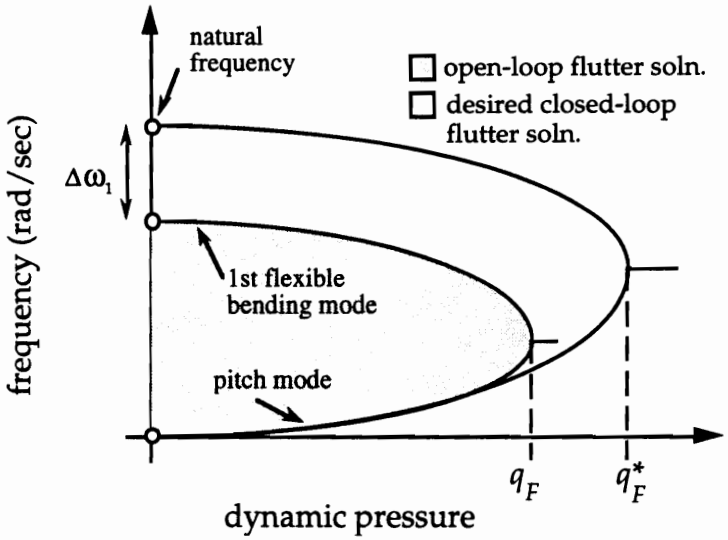

Fig. 5.1 - Hypothetical Effects of Frequency Increase on Flutter Solution

5.2 Suppression of Body-freedom Flutter Via Composite Tailoring

Composite tailoring is a method in which the aeroelastic characteristics of a wing are altered through the use of advanced composite materials. The unique directional stiffness properties of filamentary composites allow the aeroelastician to tailor the stiffness (and thus the bending frequencies) of an aircraft wing. Certainly, composite tailoring is not a new concept in the control of aeroelastic instabilities. As mentioned in the literature review, composite tailoring has been

used to alleviate divergence problems associated with clamped wings for many years (Refs. 34 - 40). Weisshaar *et al.* (Ref. 46) have also investigated the effects of composite tailoring on body-freedom flutter with positive results for some aircraft configurations.

In the present study, composite tailoring is used simply as a passive means of widening the gap between the first wing flexible bending mode and the aircraft pitch mode. As an example of this strategy, composite tailoring is carried out for the $[0/-45/+45/0]_s$ graphite/epoxy 30° forward-swept wing discussed previously. In Fig. 5.2, we have a plot of the variation of the two lowest wing natural frequencies as the ply angle of the outside layer is swept from -80° to 80°. All angles are measured with respect to the midchord sweep angle, with the convention that a positive angle indicates forward sweep.

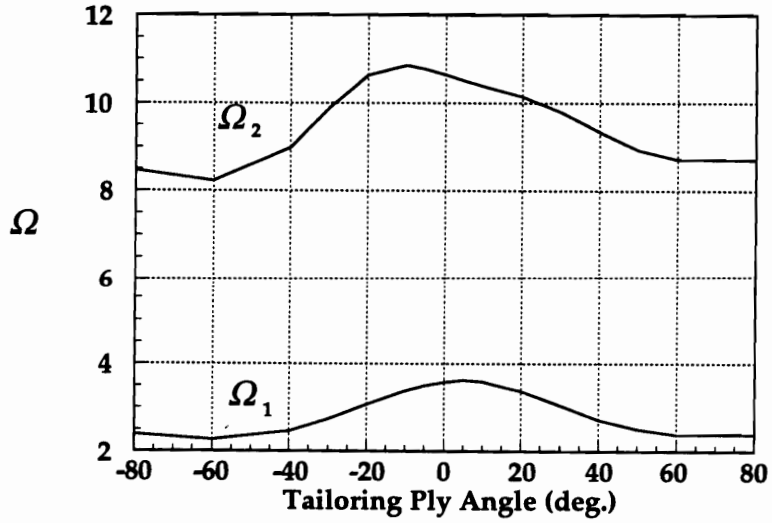

Fig. 5.2 - Nondimensional Frequency vs Tailoring Ply Angle

For this forward-swept wing, a tailoring angle placing the graphite fibers slightly aft of the midchord produces the maximum frequency for the first flexible mode. We recall that the aircraft pitch mode natural frequency is

identically zero. Theoretically, the ply angle producing the maximum value of the lowest wing bending frequency will produce the highest flutter airspeed.

A plot of the flutter dynamic pressure variation with the tailoring angle is shown in Fig. 5.3. As expected, the maximum flutter dynamic pressure occurs in the vicinity of the maximum first bending mode frequency. However, dynamic pressure is maximized when the fibers are swept slightly forward of the midchord instead of slightly aft. Clearly there are more subtle effects of composite tailoring on the body-freedom flutter mechanism than mere frequency separation. The amount of bending-twist coupling is altered as well by fiber positioning, thus affecting the amount of wash-in and ultimately the flutter airspeed. Indeed, in Fig. 5.2, we see that a slight forward sweep of the tailoring fibers tends to stiffen the wing torsionally, thus reducing the increase in effective angle of attack caused by bending.

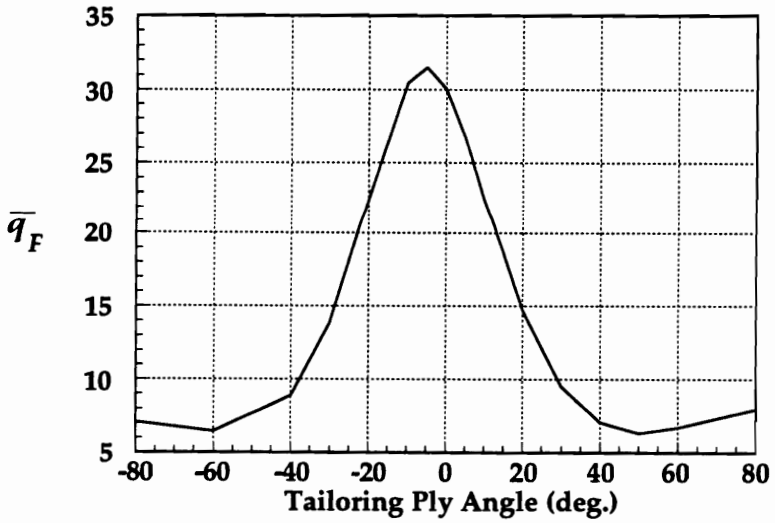

Fig. 5.3 - Nondimensional Flutter Dynamic Pressure vs Tailoring Ply Angl

This numerical example is certainly a simplest case scenario, demonstrating the usefulness of the composite tailoring layer as a passive design

tool for maximizing the body-freedom flutter speed of a particular aircraft configuration. Certainly, the concept can be carried further by utilizing all of the ply angles as design variables as part of a larger multi-objective wing optimization procedure.

5.3 Active Control for Flutter Suppression

In the previous section, a passive method was used to demonstrate that an increase in the first bending frequency of a forward-swept wing was sufficient to cause a significant increase in the airspeed at which body-freedom flutter occurs. Similar changes in modal frequencies can also be achieved through the use of active control methods, in particular feedback of measurements or estimates of modal position variables. A straightforward technique for altering the dynamic characteristics of the wing, known as direct output feedback, will be investigated for the remainder of this chapter.

Direct output feedback is a control method in which sensor output signals are multiplied by an appropriate set of gains and used to drive the system actuators. This type of procedure has received widespread use in the past, for example, Refs. 113 & 114, where outputs from velocity sensors are fed back to collocated actuators for control of vibration in flexible spacecraft. An extensive bibliography on the subject is contained in Ref. 71. For the case at hand, the aircraft wing structure is equipped with piezoelectric patches for both sensing and actuation. The sensor output voltages were shown in Chapter 3 to be proportional to system displacement variables. Thus, feedback of sensor voltages amounts to position feedback and presents a means of altering the modal frequencies of the flexible wing.

One may be wary of using a reduced-order model for control design, due to a problem known as control spillover (Ref. 71), in which control energy may excite unmodeled or unretained modes, causing instabilities. However, in the proposed design, spillover does not pose a threat to system stability. Since we are feeding back position measurements, at most spillover can effect only the frequencies of higher modes. Thus destabilization, which would imply adversely affecting the damping of unmodeled modes, is not a possibility. Also, control spillover has been shown to have minimal effects in configurations where sensors and actuators are collocated, as in the present model.

5.3.1 Collocated Position Feedback

The control design is based on the reduced-order modal system equations developed in Chapter 4. For simplicity, the modal equations of motion are re-introduced here, as

$$\begin{aligned} &\ddot{\eta} + \overline{H}_A \dot{\eta} + \left[\Omega_f^2 + \overline{K}_A\right]\eta = \overline{B} v_c(t) \\ &v_s(t) = \overline{C}\eta(t) \end{aligned} \tag{5.1}$$

where $\eta(t)$ is the vector of modal displacement variables, Ω_f the matrix of modal frequencies, $\overline{K}_A$ and $\overline{H}_A$ the modal aerodynamic stiffness and damping matrices, respectively, $\overline{B}$ the modal actuator participation matrix, $\overline{C}$ the modal sensor participation matrix and $v_c(t)$ and $v_s(t)$ the vectors of control input and sensor output voltages, respectively. Our primary goal is to increase the frequency of the first flexible wing bending mode. This opens up the prospect of designing a very simple output feedback control law based on the system equations of motion without aerodynamics, or

$$\ddot{\eta} + \Omega_f^2 \eta = \overline{B} v_c(t) \tag{5.2}$$

For position feedback, the vector of sensor output voltages are multiplied by a gain matrix to produce the sensor input voltages, or

$$v_c(t) = Gv_s(t) = G\overline{C}\eta(t) \tag{5.3}$$

and the resulting closed-loop system of equations (without aerodynamics) is given by

$$\ddot{\eta} + \left[\Omega_f^2 - \overline{B}G\overline{C}\right]\eta = \mathbf{0} \tag{5.4}$$

It can be shown that the closed-loop system of equations remains self-adjoint, *i.e.*, $\overline{B}G\overline{C}$ is symmetric, as long as the gain matrix is chosen to be symmetric. The proof follows from similarities in the participation matrices, as a result of using piezoelectric patches for both sensing and actuation, and is included in Appendix C. This result is expected, as position feedback cannot introduce any energy dissipation into the system.

The question remains as to the choice of the gain matrix G. One method, referred to as collocated position feedback (CPF), is to feed each sensor output voltage back only to the collocated actuator. The gain matrix in this case is diagonal, taking the form

$$\begin{Bmatrix} v_{c1} \\ v_{c2} \\ \vdots \\ v_{cm} \end{Bmatrix} = \begin{bmatrix} g_1 & & & 0 \\ & g_2 & & \\ & & \ddots & \\ 0 & & & g_m \end{bmatrix} \begin{Bmatrix} v_{s1} \\ v_{s2} \\ \vdots \\ v_{sm} \end{Bmatrix} \tag{5.5}$$

where m is the number of collocated sensor/actuator pairs. The individual gains are chosen essentially by a trial and error process in order to produce the desired increases in the system first natural frequency. This process is equivalent to most

classical control approaches, where gains are selected to satisfy various design criteria based on the closed-loop system eigenvalues or response. An ad hoc approach has also been developed to generate gains producing desired changes in the system natural frequencies. The approach is based on symbolic calculation of the matrix $\overline{B}G\overline{C}$, and is possible when a low number of modes is retained in the reduced-order model.

5.3.2 Independent Modal Space Control

Another option for selecting the gain matrix in Eq. (5.3) is to design the control law in the modal space, a process known as independent modal space control, IMSC (Ref. 71). This design is based on the modal equations, Eqs. (5.1a) rewritten in the following form:

$$\ddot{\eta}_i + w_i^2 \eta_i = Z_i(t) \qquad i = 1,2,\ldots,N_f \tag{5.6}$$

where $\boldsymbol{Z}(t)$ is the vector of modal control forces, which for the purpose of position feedback are proportional to the modal position coordinates, or

$$\boldsymbol{Z}(t) = \hat{G}\eta(t) \qquad \hat{G} = diag(\hat{g}_k), \quad k = 1,2,\ldots,m \tag{5.7}$$

Modal gain selection is now simply a matter of choosing the desired increase or decrease in each modal frequency independently, since the closed-loop modal equations remain independent, and take the form

$$\ddot{\eta}_i + (w_i^2 - \hat{g}_i)\eta_i = 0 \qquad i = 1,2,\ldots,N_f \tag{5.8}$$

If we desire to change only the first wing natural frequency, then only the first modal gain must be nonzero. The question remains as to the relationship between the modal gain matrix $\hat{G}$ and the actual gain matrix G, since for actual implementation we know the control law must take the form of Eq. (5.3). The

modal control forces are related to the actual control voltages by an N_f x m modal participation matrix, or

$$\mathbf{Z}(t) = \overline{B}\, v_c(t) \tag{5.9}$$

The actual control voltages are found by inverting Eq. (5.9). Assuming that the inverse exists, the implications of which will be discussed shortly, substitution of the modal control law into the result yields the vector of control voltages, given by

$$v_c(t) = \overline{B}^{-1}\hat{G}\eta(t) \tag{5.10}$$

Similarly, the sensor output vector is directly related to the modal position vector through the m x N_f modal sensor participation matrix according to

$$v_s(t) = \overline{C}\,\eta(t), \qquad \eta(t) = \overline{C}^{-1} v_s(t) \tag{5.11a,b}$$

Assuming that the inverse in Eq. (5.11b) exists, the final relationship between the actual control and output voltages is found by substitution of this equation into Eq. (5.10) with the result

$$v_c(t) = \overline{B}^{-1}\hat{G}\overline{C}^{-1} v_s(t) = G v_s(t) \tag{5.12}$$

Examining the form of Eq. (5.12), one can conclude that the gain matrix relating sensor outputs to actuator inputs is symmetric but no longer diagonal. In other words, we now have cross-feedback in which the signal from each sensor is multiplied by gains and fed back to all of the actuators.

We now return to the conditions under which the two inverses in Eq. (5.12) exist. First of all, for both inverses to exist, the matrices must be square, implying that N_f = m, or that the number of modes retained in the

truncated system of modal equations must equal the number of sensor/actuator pairs. Furthermore, for $\overline{B}^{-1}$ to exist, the participation matrix $\hat{B}$ must be non-singular, a condition analogous to a statement of modal controllability. For the problem at hand, the modal equations are controllable via piezoelectric actuation as long as only the flexible modes are retained in the modal system of equations. Similarly, the inverse matrix $\overline{C}^{-1}$ exists under the condition of modal observability which is indeed met for the flexible modes when using piezoelectric sensors. Thus, the above restrictions imply that the control gains may be designed using IMSC as long as the design is based on a modal system of equations (zero airspeed) retaining as many flexible degrees of freedom as sensor/actuator pairs.

It should be pointed out that both the CPF and IMSC control techniques are modal methods, as they are both based on the system modal equations. The difference lies in the closed-loop equations, which are coupled using CPF, Eq. (5.4), and independent under IMSC, Eq. (5.8). In the following section, numerical results are presented for control designs based on both methods.

5.4 Numerical Examples

Two control laws were designed for the $[0/-45/+45/0]_s$ graphite/epoxy wing in a 30° forward-swept configuration. Four modes were retained in the reduced-order model. A test configuration was chosen with four piezoceramic pairs (Fig. 5.4), the dimensions, exact placement locations and material properties of which are given in Appendix B. It was demonstrated in Chapter 4 that body-freedom flutter is the most critical instability for this configuration. Open-loop flutter occurs at a nondimensional dynamic pressure given by $\bar{q} = 30$, at which point the first bending mode becomes unstable (Fig. 4.4).

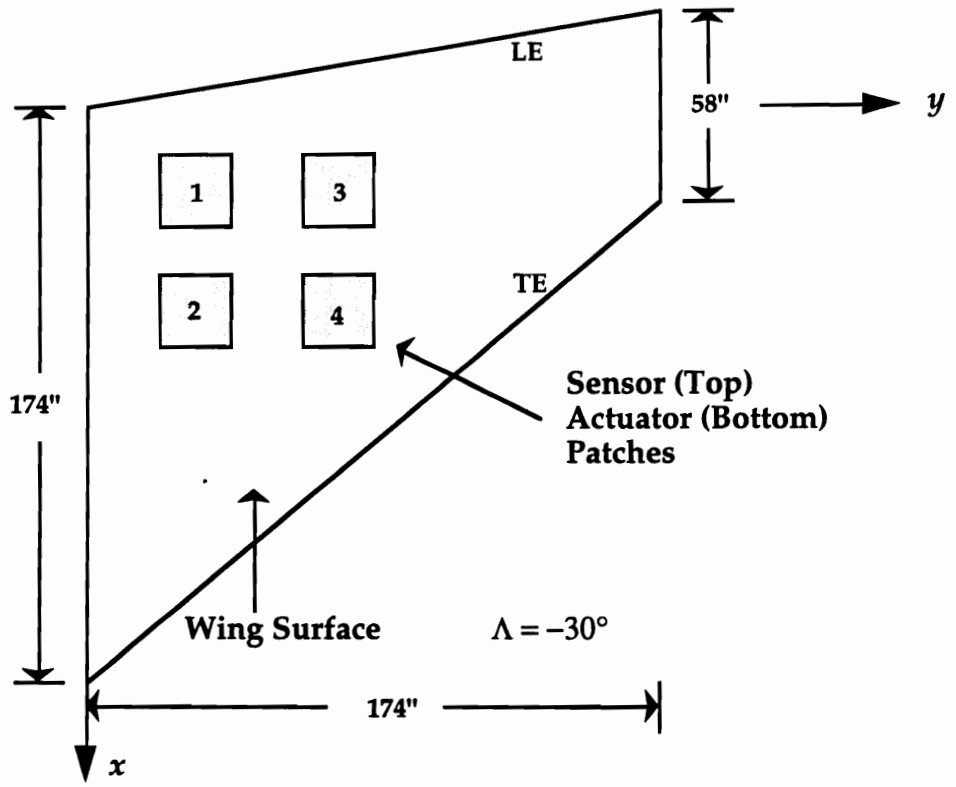

Fig. 5.4 - Graphite/Epoxy FSW Model with Four Surface-Mounted Sensors and Actuators

Gain matrices were chosen using the CPF and IMSC methods outlined in the previous sections, with a goal of increasing the zero-airspeed frequency of the first flexible mode by approximately ten percent. The resulting gain matrices are shown in Table 5.1. The gains generated using IMSC are generally larger in magnitude than those chosen using CPF. This result is expected, since the above choice of modal gain matrix has essentially placed additional constraints on the closed-loop equations, prescribing that all modal frequencies except the first flexible mode remain unchanged. On the other hand, the CPF gain matrix in Table 5.1 resulted in a decrease of approximately two percent in the frequency of the second flexible mode.

Table 5.1 - Output Feedback Gain Matrices

CPF				IMSC							
G				$\hat{G}$				G			
-31.2	0	0	0	-600	0	0	0	-.01	-.17	-.82	.82
0	-12.6	0	0	0	0	0	0	-.17	-7.15	-33.4	33.2
0	0	37.0	0	0	0	0	0	-.82	-33.4	-155.9	154.9
0	0	0	39.9	0	0	0	0	.82	33.2	154.9	-153.9

Results from flutter analysis of the closed-loop system are shown in Figs. 5.5 and 5.6. The open-loop flutter analysis from Chapter 4 is included in these graphs for comparison. A plot of nondimensional frequency versus nondimensional dynamic pressure is shown in Fig 5.5. It is obvious from this plot that the increased frequency of the flexible mode in the closed-loop systems has indeed delayed the onset of frequency coalescence as predicted.

Since aerodynamic damping is included in the model, we must look to the real part of the eigenvalues to determine the onset of flutter (Fig. 5.6). In this figure, we see that flutter occurs at $\bar{q}$ = 42 and 44 for the collocated feedback and IMSC control laws, respectively. This represents increases of 40% and 46% in flutter dynamic pressure over the uncontrolled aircraft.

The differences in damping between the closed-loop and open-loop cases is not a direct result of position feedback. Indeed, it is not possible to alter modal damping characteristics directly without velocity feedback. Instead, the flexible bending mode remains stable at higher airspeeds as a result of the delayed interaction between the two modes achieved through position feedback. These findings support earlier arguments that frequency coalescence is indeed the true triggering mechanism for body-freedom flutter.

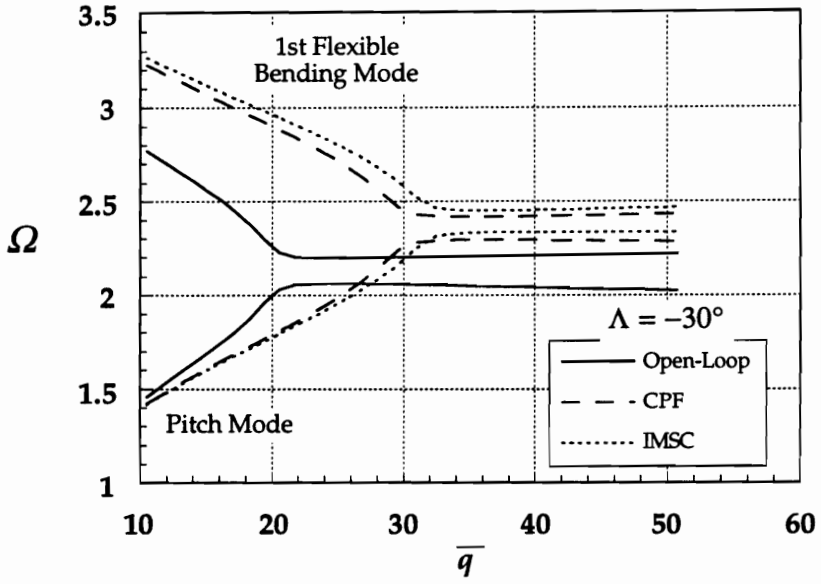

Fig. 5.5 - Comparison of Open and Closed-Loop Flutter Solutions

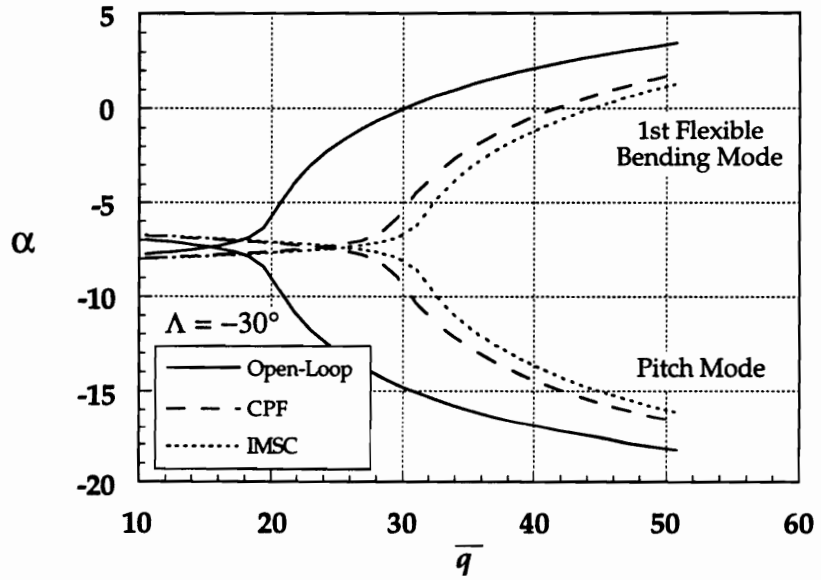

Fig. 5.6 - Comparison of Open and Closed-Loop Flutter Solutions

5.5 Gust Response Simulations

When using piezoelectric materials for control applications, care must be taken to keep the applied voltages well below the depoling voltage of the material, at which point the desirable properties of the material are destroyed.

The closed-loop performance of the system must be evaluated through numerical simulation. One such method of evaluating a design is calculation of the flexible wing response to gusts, pockets of turbulent air encountered during normal level flight conditions.

Calculation of gust response can be a very computationally intensive task, depending on assumptions made about the gust profile and the aerodynamic theory used. Consideration of wing flexibility complicates modeling further. To simplify calculations, in the case at hand, gust loading is considered equivalent to an impulsive external disturbance acting on the mathematical model,

$$M\ddot{q} + H_A\dot{q} + [K + K_A]q = Q_g\delta(t) \tag{5.13}$$

or in its modal counterpart,

$$\ddot{\eta} + \overline{H}_A\dot{\eta} + \left[\Omega_f^2 + \overline{K}_A\right]\eta = \Phi_f^T Q_g\delta(t) \tag{5.14}$$

where Q_g is an intensity vector for the turbulent disturbance and $\delta(t)$ is the Dirac delta function. It can be shown (Ref. 115) that the net effect of such an impulsive force is to cause a finite change in the modal velocities, given by

$$\dot{\eta}(0^+) = \Phi_f^T Q_g \tag{5.15}$$

without a corresponding change in modal displacements. The response is then calculated by choosing a flight speed and solving the closed-loop equations of motion in state space form:

$$\begin{aligned} \frac{d}{dt}\begin{Bmatrix}\eta\\ \dot{\eta}\end{Bmatrix} &= \begin{bmatrix} 0 & I \\ -(\Omega_f^2 + \overline{K}_A - \overline{B}G\overline{C}) & -\overline{H}_A \end{bmatrix}\begin{Bmatrix}\eta\\ \dot{\eta}\end{Bmatrix} \\ v_s(t) &= \begin{bmatrix}\overline{C} & 0\end{bmatrix}\begin{Bmatrix}\eta\\ \dot{\eta}\end{Bmatrix} \end{aligned} \tag{5.16a,b}$$

with the initial conditions given by Eq. (5.15). In light of the piston theory aerodynamic approximation used in the present aircraft model, this highly simplified approach to gust response seems appropriate. Better approximation to gust response would require a significantly more complex aerodynamic theory.

Gust response calculations for the uncontrolled aircraft of Fig. 5.4 are shown in Figs. 5.7 and 5.8, which show the variation with time of voltage output from sensors 1 and 4 at two different nondimensional dynamic pressures. The lower dynamic pressure, $\bar{q}$= 23.6 in Fig. 5.5, corresponds to an airspeed 20% below the open-loop flutter speed, while the higher dynamic pressure, $\bar{q}$= 37.9, corresponds to an airspeed 25% above the open-loop flutter speed. Recall that the output voltages are proportional to generalized elastic displacement variables of the flexible wing. Below the flutter speed, the gust disturbance results in low amplitude vibration which is quickly damped out. However, above the open-loop flutter speed the catastrophic nature of the flutter event is obvious, as a small disturbance results in wing vibration that quickly grows over time.

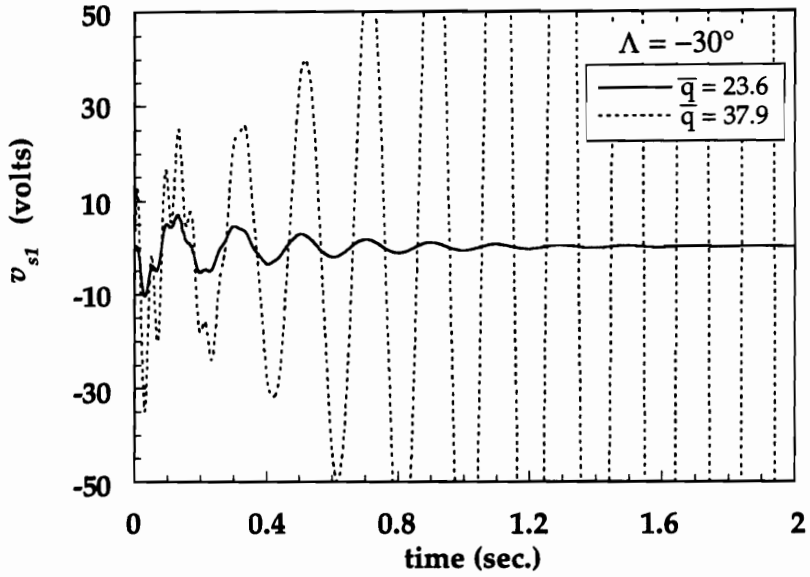

Fig. 5.7 - Open-Loop Gust Response: Sensor 1 Output

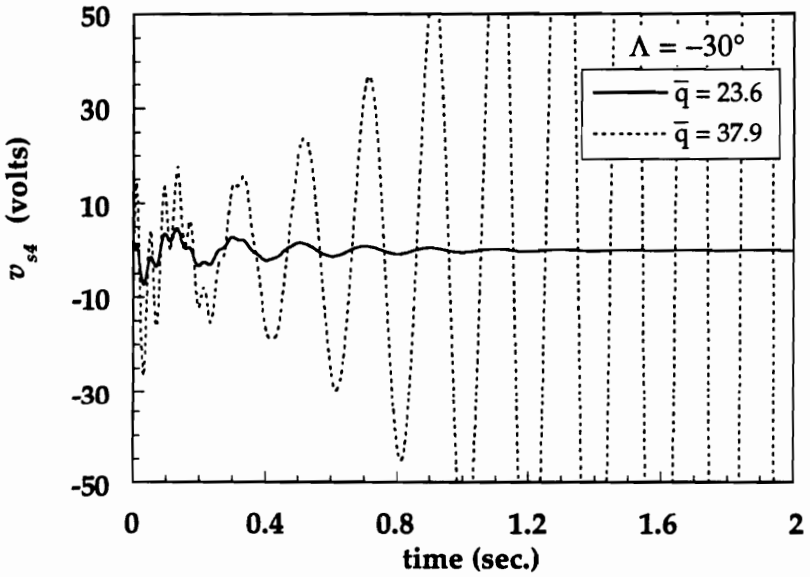

Fig. 5.8 - Open-Loop Gust Response: Sensor 4 Output

Simulations of the closed-loop system at the previously unstable dynamic pressure, $\bar{q} = 37.9$, are shown in Figs. 5.9 and 5.10. Both control designs use four actuator/sensor pairs as described in Section 5.4. Contributions from both the first and second flexible bending modes are present in the sensor output signals

in these graphs. The vibration of the second mode, which is heavily damped at this airspeed, dies out after the first few cycles of the response. The first bending mode, albeit lightly damped at this airspeed, remains stable as a result of the active induced-strain control laws.

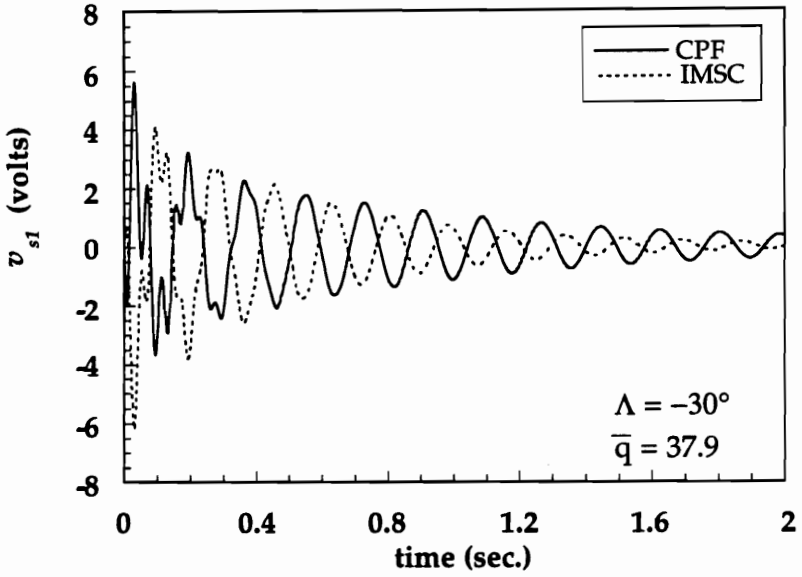

Fig. 5.9 - Closed-Loop Gust Response: Sensor 1 Output

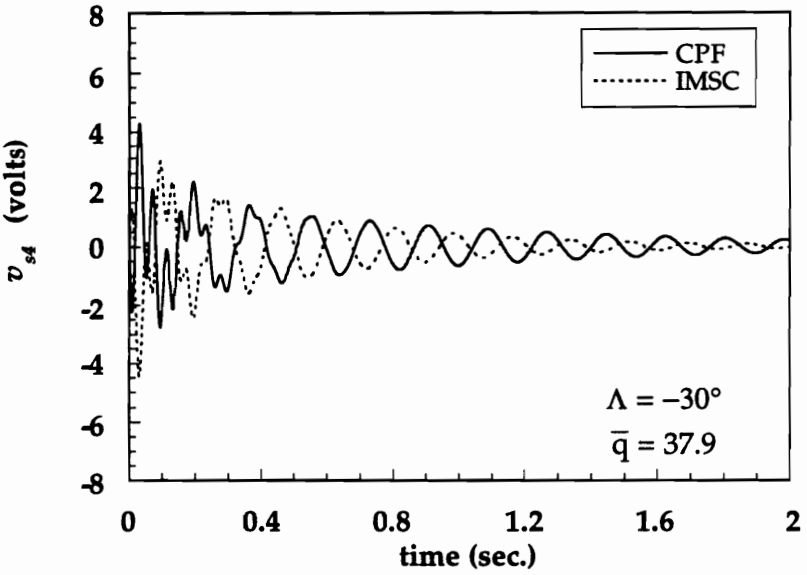

Fig. 5.10 - Closed-Loop Gust Response: Sensor 4 Output

The input signals to actuators 1 and 4 at the same dynamic pressure are shown in Figs. 5.11 and 5.12, respectively. As a result of the symmetry of the patch locations, the input signal to patch 2 was very similar to the input for patch 1 and likewise input signal 3 closely resembled input signal 4 (see Fig. 5.4).

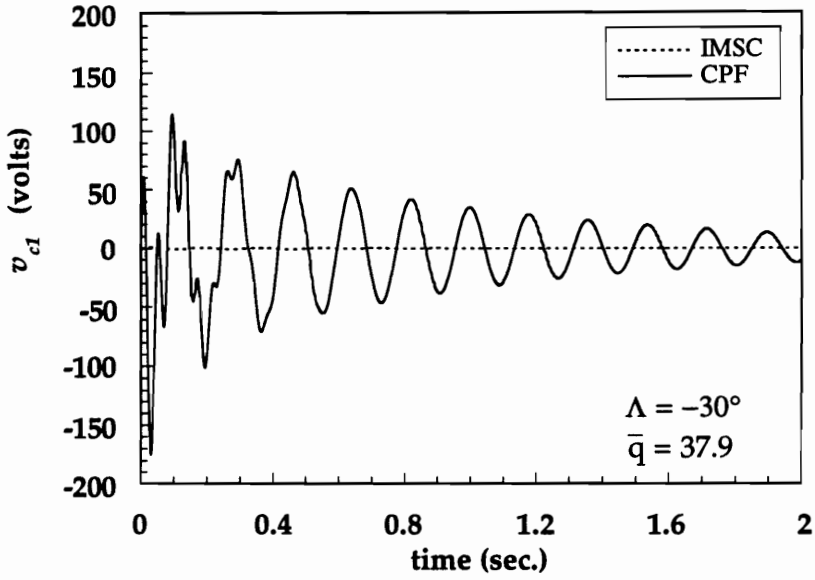

Fig. 5.11 - Closed-Loop Gust Response: Actuator 1 Input

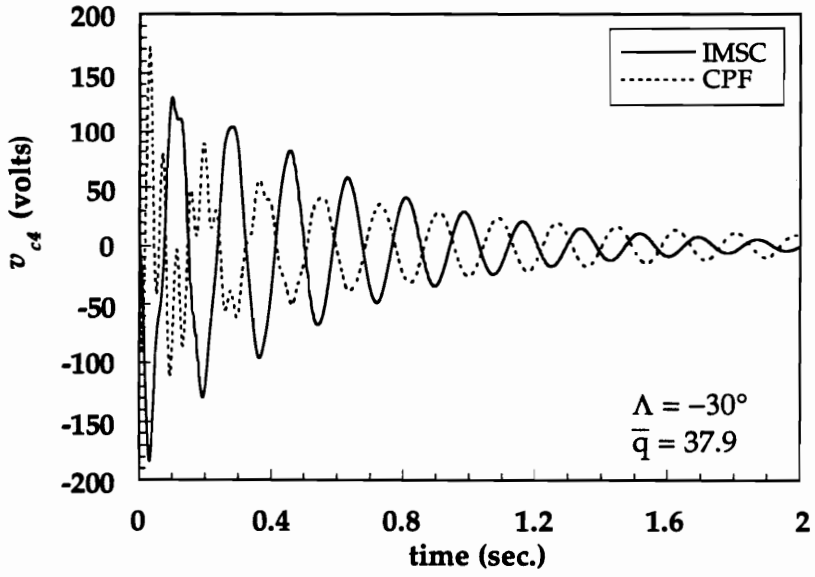

Fig. 5.12 - Closed-Loop Gust Response: Actuator 4 Input

The first important feature of the actuator signals is that the voltage limits, roughly ± 170 volts, are well under the depoling voltage of 250 volts for this actuator configuration. Secondly, an interesting difference between the collocated feedback and IMSC designs is evident when the input signals to actuators 1 and 4 (or 2 and 3) are compared. The collocated output feedback control design tends to use each of the four actuators in roughly equal proportions. This behavior follows directly from the fact that the four gains chosen in the feedback gain matrix had generally the same magnitude (Table 5.1). On the other hand, with the IMSC control law in place, the input to actuator 4 is of much higher magnitude than the input to actuator 1. This behavior suggests that actuator placement location 4 is a more effective location for altering the frequency of the first flexible bending mode. We recall that the IMSC modal gain matrix was chosen to produce a desired change in the system behavior, namely, a change in the frequency of the first wing bending mode. The actual gain matrix calculation introduces information about actuator and sensor participation, through Eq. (5.12), and thus essentially "chooses" the most effective actuator(s) for the task. For the case at hand, actuator 1 is not needed to produce the required performance.

5.6 Conclusions and Comments

In this chapter, two simple, effective strategies have been demonstrated for increasing the body-freedom flutter airspeed of an aircraft with forward-swept wings. Aeroelastic tailoring is a passive approach in which composite laminate ply angles are varied to maximize the wing first bending natural frequency. Results indicate that fiber orientation affects not only the frequency separation between the first bending mode and the aircraft pitch mode, but also

the amount of bending-twist coupling in the wing. Both of these factors must be considered to derive the greatest benefit from tailoring techniques.

Piezoelectric patches were shown to be viable alternatives to conventional control surfaces for active flutter control. Their light weight makes them ideal for use in modern aircraft designs. Two straightforward direct output feedback control laws were formulated based on the hypothesis that dynamic stiffening of the wing first bending frequency would deter the coalescence event (and thus flutter) to higher airspeeds. Collocated position feedback and independent modal space control laws were designed to increase the natural frequency of a model's first flexible mode by 10%. The effectiveness of these strategies was verified through closed-loop solutions of the flutter eigenvalue problem, where the CPF and IMSC control laws produced 40% and 46% increases in the nondimensional flutter dynamic pressure, respectively. One advantage to these control strategies is that the control laws are airspeed independent. Furthermore, since only position feedback is used, no problems with control or observation spillover are expected. In future work, consideration should be given to the practical implementation concerns such as the effects of signal noise on closed-loop performance, although piezoelectric sensors typically exhibit low noise-to-signal ratios. Certainly, the simulations contained herein constitute a basis for experimental investigation.

A few comments should be made with respect to gain selection. One of the major goals of the study was to prove that rigid-body control was not necessary to positively alter an aircraft's body-freedom flutter airspeed. Thus, no provisions were made for rigid-body actuation. Instead, control was carried out using a smart-structure approach, with piezoelectric sensors and actuators,

leaving the wing control surfaces free for use in attaining other flight performance goals. While the gains in this study were not chosen to satisfy any optimality conditions, the resulting control laws are practical, easily implemented and produce the desired closed-loop system performance. Furthermore, it was shown that the IMSC control design tends to choose effective patch locations, since actuator and sensor participation information is used in the calculation of the actual gain matrix. It should be noted that there are routines available for choosing output feedback gains in a mathematically optimal sense (Ref. 116).

In Chapter 5, the benefits of using composite tailoring and active control for flutter suppression were demonstrated when applied separately to an advanced aircraft configuration. Based on the results, one can certainly envision that the greatest benefits may be reaped through a combination of the two approaches, taking full advantage of wing flexibility, active control technology and advanced composite materials. A multi-objective design package might include design variables such as wing sweep, ply orientation angles and control gains with objectives such as maximizing the flutter dynamic pressure of a minimum weight design. Furthermore, actuator number and placement as well as constraints on maximum closed-loop output voltages under the action of external disturbances and/or constraints on control gain magnitudes should be considered. Such a complex optimization package is beyond the scope of this project. However, the mathematical model developed during this research effort is a tool well suited for use at the predesign stage of aircraft development, allowing complete generality in two-dimensional composite wing geometry and including all the features essential for modeling various flutter mechanisms. In addition, the reduced-order form of the governing equations is particularly well

suited to optimization routines, which typically require system analysis at many consecutive iterations.

REFERENCES

1. Collar, A. R., "The Expanding Domain of Aeroelasticity," *The Journal of the Royal Aeronautical Society*, Vol. 50, June, 1946, pp. 613-636.

2. Garrick, I. E., and Reed, W. H. III, "Historical Development of Aircraft Flutter," *Journal of Aircraft*, Vol. 18, No. 11, November 1981, pp. 897-912.

3. Collar, A. R., "Aeroelasticity - Retrospect and Prospect," *The Journal of the Royal Aeronautical Society*, Vol. 63, January, 1959, pp. 1-15.

4. Accidents Investigation Subcommittee, "Report on Puss Moth Accidents," British Aeronautical Research Council R. & M. 1699, 1936.

5. NACA Subcommittee on Vibration and Flutter, "A Survey and Evaluation of Flutter Research and Engineering," NACA RM-56112, 1956.

6. Temple, G. and Jahn, H. A., "Flutter at Supersonic Speeds," British Aeronautical Research Council R. & M. 2140, 1945.

7. Garrick, I. E. and Rubinow, S. I., "Flutter and Oscillating Air Force Calculations for an Airfoil in a Two-Dimensional Supersonic Flow," NACA Rept. 846, 1946.

8. von Baumhauer, A. G. and Koning, C., "On the Stability of Oscillations of an Airplane Wing," NACA TM-223, 1923.

9. Zahm, A. F. and Bear, R. M., "A Study of Wing Flutter," NACA Rept. 285, 1926.

10. Roger, K. L., Hodges, G. E. and Felt, Larry, "Active Flutter Suppression–A Flight Test Demonstration," *Proceedings of the 15th AIAA/ASME/SAE Structures, Structural Dynamics and Materials Conference*, Las Vegas, Nevada, April 17 - 19, 1974.

11. O'Connell, R. F. and Messina, A. F., "Development of an Active Flutter Margin Augmentation System for a Commercial Transport," *Journal of Guidance and Control*, Vol. 3, No. 4, July 1980, pp. 352-360.

12. Foss, R. L. and Lewolt, J., "Use of Active Controls for Fuel Conservation of Commercial Transports," AIAA Paper No. 77-1220, August 1977.

13. Triplett, W. E., Kappus, H. P. F. and Landey, R. J., "Active Flutter Suppression Systems for Military Aircraft - A Feasibility Study," AFFDL-TR-72-116, Feb. 1973.

14. Sensburg, O., Honlinger, H., Noll, T. E. and Huttsell, L. J., "Active Flutter Suppression on an F-4F Aircraft," *Journal of Aircraft*, Vol. 19, No. 5, 1982, pp. 354-359.

15. Hwang, C., Johnson, E. H. and Pi, W. S., "Recent Development of the YF-17 Active Flutter Suppression System," *Journal of Aircraft*, Vol. 18, No. 7, 1981, pp. 537-545.

16. Visor, O. E. and Sevart, F. D., "Preliminary Design Study of Flutter Suppression Control System for BQM-34E/F Drone Aircraft with a Supercritical Wing - Final Report," NASA CR-143208, 1978.

17. Nissim, E., "Comparative Study Between Two Different Active Flutter Suppression Systems," *Journal of Aircraft*, Vol. 15, No. 12, Dec. 1978, pp. 843-848.

18. Newsom, J. R., "Control Law Synthesis for Active Flutter Suppression Using Optimal Control Theory," *Journal of Guidance and Control*, Vol. 2, No 5, 1979, pp. 388-394.

19. Mahesh, J. K., Stone, C. R., Garrard, W. L. and Dunn, H. J., "Control Law Synthesis for Flutter Suppression Using Linear Quadratic Gaussian Theory," *Journal of Guidance and Control*, Vol. 4, No. 4, July 1981, pp. 415-422.

20. Mukhopadhyay, V., Newsom, J. R. and Abel, I., "Reduced-Order Optimal Feedback Control Law Synthesis for Flutter Suppression," *Journal of Guidance and Control*, Vol. 5, No. 4, July 1982, pp. 389-395.

21. Newsom, J. R., "A Method for Obtaining Practical Flutter Suppression Control Laws Using Results of Optimal Control Theory," NASA TP-1471, 1979.

22. Mukhopadhyay, V., Newsom, J. R. and Abel, I., "A Method for Obtaining Reduced-Order Control Laws for High-Order Systems Using Optimization techniques, NASA TP-1876, 1981.

23. Abel, I., Perry, B. III and Murrow, H. N., "Two Synthesis Techniques Applied to Flutter Suppression on a Flight Research Wing," *Journal of Guidance and Control*, Vol. 1, No. 5, Sept., 1978, pp. 340-346.

24. Newsom, J. R., Abel, I. and Dunn, H. J., "Application of Two Design Methods for Active Flutter Suppression and Wind Tunnel Test Results, NASA TP-1653, 1980.

25. Nissim, E., "Design of Control Laws for Flutter Suppression Based on the Aerodynamic Energy Concept and Comparisons with Other Design Methods," AIAA Paper 89-1212, April 1989.

26. Perry, B. III, Cole, S. R. and Miller, G. D., "A Summary of the Active Flexible Wing Program," *Proceedings of the AIAA Dynamics Specialist Conference*, Dallas Texas, April 16 - 17, 1992, pp. 1-10. (AIAA 92-2080-CP).

27. Buttrill, C., Bacon, B., Heeg, J., Houck, J. and Wood, D., "Simulation and Model Reduction for the AFW Program," *Proceedings of the AIAA Dynamics Specialist Conference*, Dallas Texas, April 16 - 17, 1992, pp. 11-19. (AIAA 92-2081-CP).

28. Mukhopadhyay, V., "Flutter Suppression Digital Control Law Design and Testing for the AFW Wind-Tunnel Model," *Proceedings of the AIAA Dynamics Specialist Conference*, Dallas Texas, April 16 - 17, 1992, pp. 156-161. (AIAA 92-2095-CP).

29. Waszak, M. R. and Srinathkumar, S., "Flutter Suppression for the Active Flexible Wing: Control System Design and Experimental Validation," *Proceedings of the AIAA Dynamics Specialist Conference*, Dallas Texas, April 16 - 17, 1992, pp. 138-145. (AIAA 92-2097-CP).

30. Christhilf, D. M. and Adams, W. M. Jr., "Multifunction Tests of a Frequency Domain Based Flutter Suppression System," *Proceedings of the AIAA Dynamics Specialist Conference*, Dallas Texas, April 16 - 17, 1992, pp. 146-155. (AIAA 92-2096-CP).

31. Klepl, M. J., "A Flutter Suppression System Using Strain Gages Applied to Active Flexible Wing Technology: Design and Test," *Proceedings of the AIAA Dynamics Specialist Conference*, Dallas Texas, April 16 - 17, 1992, pp. 162-171. (AIAA 92-2098-CP).

32. Diederick, F. W. and Budiansky, B., "Divergence of Swept Wings," NACA TN-1680, 1948.

33. Bisplinghoff, R. L. and Ashley, H., *Principles of Aeroelasticity*, New York, Dover Publications, Inc., 1975.

34. Krone, N. J. Jr., "Divergence Elimination with Advanced Composites," AIAA Paper No. 75-1009, August, 1975.

35. Krone, N. J. Jr., "Forward Swept Wing Flight Demonstrator," AIAA Paper No. 80-1882, August, 1980.

36. Spacht, G., "The Forward Swept Wing: A Unique Design Challenge," AIAA Paper No. 80-1885, August, 1980.

37. Weisshaar, T. A., "Aeroelastic Tailoring of Forward Swept Composite Wings," AIAA Paper No. 80-0795, May, 1980.

38. Lerner, E. and Markowitz, J., "An Efficient Structural Resizing Procedure for Meeting Static Aeroelastic Design Objectives," AIAA Paper No. 78-0471, April, 1978.

39. Triplett, W. E., "Aeroelastic Tailoring Studies for Fighter Aircraft Design," AIAA Paper No. 79-0725, April, 1979.

40. Weisshaar, T. A., "Aeroelastic Tailoring - Creative Use of Unusual Materials," AIAA Paper No. 87-0976, April, 1987.

41. Sherrer, V. C., Hertz, T. J. and Shirk, M. H., "Wind Tunnel Demonstration of Aeroelastic Tailoring Applied to Forward Swept Wings," *Journal of Aircraft*, Vol. 18, No. 11, pp. 976-983.

42. Hertz, T. J., Shirk, M. H., Ricketts, R. H. and Weisshaar, T. A, "On the Track of Practical Forward-Swept Wings," *Astronautics & Aeronautics*, Vol. 20, Jan. 1982, pp. 40-53.

43. Hollowell, S. J. and Dugundji, J., "Aeroelastic Flutter and Divergence of Stiffness Coupled, Graphite/Epoxy Cantilevered Plates," *Journal of Aircraft*, Vol. 21, No. 1, Jan., 1984, pp. 69-76.

44. Lottati, I., "Flutter and Divergence Aeroelastic Characteristics for Composite Forward Swept Cantilevered Wing," *Journal of Aircraft*, Vol. 22, No. 11, Nov., 1985, pp. 1001-1007.

45. Miller, G. D., Wykes, J. H. and Brosnan, M. J., "Rigid-Body Structural Mode Coupling on a Forward Swept Wing Aircraft," *Journal of Aircraft*, Vol. 20, No. 8, August, 1983, pp. 696-702.

46. Weisshaar, T. A., Zeiler, T. A., Hertz, T. J. and Shirk, M. H., "Flutter of Forward Swept Wings, Analysis and Tests," AIAA Paper No. 82-0646, May, 1982.

47. Frazer, R. A. and Duncan, W. J., "Wing Flutter as Influenced by the Mobility of the Fuselage," British Aeronautical Research Council, R. & M. 1207, 1929.

48. Broadbent, E. G., "Some Considerations of the Flutter Problems of High Speed Aircraft," *Proceedings of the 2nd International Aircraft Conference*, New York, 1949, pp. 556-581.

49. Gaukroger, D. R., "Wind Tunnel Test on the Symmetric and Antisymmetric Flutter of Swept-back Wings," British Aeronautical Research Council R. & M. 2911, 1955.

50. Gaukroger, D. R., "Wind Tunnel Flutter Tests on Model Delta Wings Under Fixed and Free-Root Conditions," British Aeronautical Research Council R. & M. 2911, 1955.

51. Gaukroger, D. R., "Wing Flutter," *AGARD Manual on Aeroelasticity*, Part V, Chapter 2, 1960.

52. Cunningham, H. J. and Lundstrom, R. R., "Description and Analysis of a Rocket-Vehicle Experiment on Flutter Involving Wing Deformation and Body Motions," NACA TN 3311, January, 1955.

53. Weisshaar, T. A. and Zeiler, T. A., "Dynamic Stability of Flexible Forward Swept Wing Aircraft," *Journal of Aircraft*, Vol. 20, No. 12, Dec., 1983, pp. 1014-1020.

54. Griffin, K. E. and Eastep, F. E., "Active Control of Forward Swept Wings with Divergence and Flutter Aeroelastic Instabilities," AIAA Paper No. 81-0637, April, 1981.

55. Chipman, R. R., Zislin, A. M. and Waters, C., "Active Control of Aeroelastic Divergence," AIAA Paper No. 82-0684, May, 1982.

56. Noll, T. E., Eastep, F. E. and Calico, R. A., "Active Suppression of Aeroelastic Instabilities on a Forward-Swept Wing," *Journal of Aircraft*, Vol. 21, No. 3, March, 1984, pp. 202-208.

57. Zeiler, T. A. and Weisshaar, T. A., "Integrated Aeroservoelastic Tailoring of Lifting Surfaces," *Journal of Aircraft*, Vol. 25, No. 1, January, 1988, pp. 76-83.

58. Kehoe, M. W., Laurie, E. J. and Bjarke, L. J., "An In-Flight Interaction of the X-29A Canard and Flight Control System," AIAA Paper No. 90-1240-CP, May, 1990.

59. Gupta, K. K., Brenner, M. J. and Voelker, L. S., "Integrated Aeroservoelastic Analysis Capability with X-29A Comparisons," *Journal of Aircraft*, Vol. 26, No. 1, January, 1989, pp. 84-90.

60. Heeg, J., "An Analytical and Experimental Investigation of Flutter Suppression Via Piezoelectric Actuation," AIAA Paper No. 92-2106-CP, April, 1992.

61. Crawley, E. F. and de Luis, J., "Use of Piezoelectric Actuators as Elements of Intelligent Structures," *AIAA Journal*, Vol. 25, No. 10, Oct., 1987, pp. 1373-1385.

62. Crawley, E. F. and de Luis, J., "Use of Piezo-ceramics as Distributed Actuators in Large Space Structures," *Proceedings of the 26th AIAA/ASME/ASCE Structures, Structural Dynamics and Materials Conference*, Orlando, FL, April, 1985, pp. 126-133.

63. Crawley, E. F. and Anderson, E. H., "Detailed Models of Piezoceramic Actuation of Beams," AIAA Paper No. 89-1388-CP.

64. Fanson, J. L. and Caughey, T. K., "Positive Position Feedback Control for Large Space Structures," AIAA Paper No. 87-0902.

65. Dimitriadis, E. K., Fuller, C. R. and Rogers, C. A., "Piezoelectric Actuators for Distributed Vibration Excitation of Thin Plates," *Transactions of the ASME*, Vol. 113, 1991, pp. 100-107.

66. Lee, C. K., "Theory of Laminated Piezoelectric Plates for the Design of Distributed Sensors/Actuators. Part I: Governing Equations and Reciprocal Relationships," *Journal of the Acoustical Society of America*, Vol. 87, No. 3, 1990, pp. 1144-1158.

67. Crawley, E. F. and Lazarus, K. B., "Induced Strain Actuation of Isotropic and Anisotropic Plates," *AIAA Journal*, Vol. 29, No. 6, 1990, pp. 944-951.

68. Wang, B. and Rogers, C. A., "Laminate Plate Theory for Spatially Distributed Induced Strain Actuators," *Journal of Composite Materials*, Vol. 25, No. 4, 1991, pp. 433-452.

69. Lee, C. K., Chiang, W. W. and O'Sullivan, T. C., "Piezoelectric Modal Sensors and Actuators Achieving Critical Active Damping on a Cantilever Plate," AIAA Paper No. 89-1390-CP.

70. Lee, C. K., Chiang, W. W. and O'Sullivan, T. C., "Piezoelectric Strain Rate Sensor and Actuator Designs for Active Vibration Control," AIAA Paper No. 91-1064-CP.

71. Meirovitch, L., *Dynamics and Control of Structures*, Wiley Interscience, New York, 1990.

72. Dosch, J. J., Inman, D. J. and Garcia, E., "A Self-sensing Piezoelectric Actuator for Collocated Control," *Journal of Intelligent Material Systems and Structures*, Vol. 3, 1992, pp. 166-185.

73. Garcia, E. and Inman, D. J., "Advantages of Slewing an Active Structure," *Journal of Intelligent Material Systems and Structures*, Vol. 1, 1991, pp. 261-272.

74. Tani, J., Chonan, S., Liu, Y., Takahashi, F., Ohtomo, K. and Fuda, Y., "Digital Active Vibration Control of a Cantilever Beam with Piezoelectric Actuators," *ASME International Journal, Series III*, Vol. 34, No. 2, 1991, pp. 168-175.

75. Garcia, E., Dosch, J. J. and Inman, D. J., "The Application of Smart Structures to the Vibration Suppression Problem," *Journal of Intelligent Material Systems and Structures*, Vol. 3, 1992, pp. 659-667.

76. Poh, S. and Baz, A., "Active Control of a Flexible Structure Using a Modal Positive Position Feedback Controller," *Journal of Intelligent Material Systems and Structures*, Vol. 1, 1990, pp. 273-288.

77. Baz, A. and Poh, S., "Performance of an Active Control System with Piezoelectric Actuators," *Journal of Sound and Vibration*, Vol. 126, No. 2, 1988, pp. 327-343.

78. Baz, A. and Poh, S., "Experimental Implementation of the Modified Independent Modal Space Control Method," *Journal of Sound and Vibration*, Vol. 139, No. 1, 1990, pp. 133-149.

79. Bailey, T. and Hubbard, J. E., "Distributed Piezoelectric-Polymer Active Vibration Control of a Cantilever Beam," *Journal of Guidance and Control*, Vol. 8, No. 5, 1985, pp. 605-611.

80. Tzou, H. S., "Integrated Sensing and Adaptive Vibration Suppression of Distributed Systems," *Proceedings of the ASME Annual Winter Meeting*, Nov. 27 - Dec. 2, 1988, pp. 51-58.

81. Librescu, L., Meirovitch, L. and Song, O., "Integrated Structural Tailoring and Adaptive Control of Advanced Flight Vehicle Structural Vibration," AIAA Paper No. 93-1697-CP.

82. Lazarus, K. B. and Crawley, E. F., "Mutivariable High-Authority Control of Plate-Like Active Structures," AIAA Paper No. 92-2529-CP.

83. Ehlers, S. M. and Weisshaar, T. A., "Static Aeroelastic Behavior of an Adaptive Laminated Piezoelectric Composite Wing," AIAA Paper No. 90-1078-CP.

84. Ehlers, S. M. and Weisshaar, T. A., "Effect of Adaptive Material Properties on Static Aeroelastic Control," AIAA Paper No. 92-2526-CP.

85. Lazarus, K. B., Crawley, E. F. and Bohlmann, J. D., "Static Aeroelastic Control Using Strain Actuated Adaptive Structures," *Journal of Intelligent Material Systems and Structures*, Vol. 2, No. 3, July, 1991, pp. 386-410.

86. Lazarus, K. B., Crawley, E. F. and Lin, C. Y., "Fundamental Mechanisms of Aeroelastic Control with Control Surface and Strain Actuation," AIAA Paper No. 91-0985-CP.

87. Scott, R. C. and Weisshaar, T. A., "Controlling Panel Flutter Using Adaptive Materials," *Proceedings of the 32nd AIAA/ASME/ASCE/AHS/ASC Structures, Structural Dynamics and Materials Conference*, Baltimore, MD, April 8-10, 1991, pp. 2218-2229.

88. Lai, Z., Zhou, R. C., Xue, D. Y., Huang, J. and Chuh, M., "Suppression of Nonlinear Panel Flutter at Elevated Temperature with Piezoelectric Actuators," AIAA Paper No. 93-1698-CP.

89. Nam, C., Kim, W. and Oh, S., "Active Flutter Suppression of Composite Plates with Piezoelectric Actuators," AIAA Paper No. 94-1745-CP.

90. Mindlin, R. D., "Influence of Rotatory Inertia and Shear on Flexural Motions of Isotropic Elastic Plates," *Journal of Applied Mechanics*, June, 1945, pp. 69-77.

91. Reissner, E., "The Effect of Transverse Shear Deformation on the Bending of Elastic Plates," *Journal of Applied Mechanics*, March, 1951, pp. 31-38.

92. Whitney, J. M. and Pagano, N. J., "Shear Deformation in Heterogeneous Anisotropic Plates," *Journal of Applied Mechanics*, December, 1970, pp. 1033-1036.

93. Bowlus, J. A., Palazotto, A. N. and Whitney, J. M., "Vibration of Symmetrically Laminated Rectangular Plates Considering Shear Deformation and Rotatory Inertia," *AIAA Journal*, Vol. 25, No. 11, 1987, pp. 1500-1511.

94. Karpouzian, G. and Librescu, L., "Comprehensive Model of Anisotropic Composite Aircraft Wings Suitable for Aeroelastic Analysis," *Journal of Aircraft*, Vol. 31, No. 3, 1994, pp. 703-712.

95. Birman, V. and Librescu, L., "Supersonic Flutter of Shear Deformable Laminated Composite Flat Panels," *Journal of Sound and Vibration*, Vol. 139, No. 2, 1990, pp. 265-275.

96. Giles, G. L., "Further Generalization of an Equivalent Plate Representation for Aircraft Structural Analysis," *Journal of Aircraft*, Vol. 26, No. 1, 1989, pp. 67-74.

97. Meirovitch, L., *Computational Methods in Structural Dynamics*, Sijthoff & Noordhoft, The Netherlands, 1980.

98. Whitney, J., *Structural Analysis of Laminated Anisotropic Plates*, Technomic Publishing, Lancaster, PA, 1987.

99. Timoshenko, S. P. and Goodier, J. N., *Theory of Elasticity*, MCGraw-Hill Publishing, New York, 1987.

100. Jones, R. M., *Mechanics of Composite Materials*, Hemisphere Publishing, New York, 1975.

101. Meirovitch, L., *Analytical Methods in Vibrations*, Macmillan Publishing Co., New York, 1967.

102. Dowell, E. H., *A Modern Course in Aeroelasticity*, Kluwer Academic Publishers, The Netherlands, 1989.

103. Lighthill, M. J., "Oscillating Airfoils at High Mach Number," *Journal of the Aeronautical Sciences*, Vol. 20, No. 6, 1953, pp. 402-406.

104. Landahl, M. T., "Unsteady Flow Around Thin Wings at High Mach Numbers," *Journal of the Aeronautical Sciences*, Vol. 24, No. 1, 1957, pp. 33-38.

105. Ashley, H. and Zartarian, G., "Piston Theory - A New Aerodynamic Tool for the Aeroelastician," *Journal of the Aeronautical Sciences*, Vol. 23, No. 12, 1956, pp. 1109-1118.

106. Garrick, I. E. and Rubinow, S. I., "Flutter and Oscillating Air Force Calculations for an Airfoil in a Two-Dimensional Supersonic Flow," NACA Rept. No. 846, 1946.

107. Meirovitch, L. and Kwak, M. K., "Convergence of the Classical Rayleigh-Ritz Method and the Finite Element Method," *AIAA Journal*, Vol. 28, No. 8, 1990, pp. 1509-1516.

108. Hagedorn, P., "The Rayleigh-Ritz Method With Quasi-Comparison Functions in Non-Self-Adjoint Problems," *Journal of Vibration and Acoustics*, Vol. 115, July 1993, pp. 280-284.

109. Meirovitch, L. and Seitz, T. J., "Structural Modeling for Optimization of Low Aspect Ratio Composite Wings," *Journal of Aircraft*, Vol. 32, No. 5, 1995.

110. Blevins, R. D., *Formulas for Natural Frequency and Mode Shape*, Van Nostrand Reinhold, New York, 1979.

111. Kwakernaak, H. and Sivan, R., *Linear Optimal Control Systems*, Wiley-Interscience, New York, 1972.

112. Lee, C. K., "Piezoelectric Laminates: Theory and Experiments for Distributed Sensors and Actuators," *Intelligent Structural Systems*, Kluwer Academic Publishers, The Netherlands, 1992, pp. 75 -167.

113. Balas, M. J., "Direct Output Feedback Control of Large Space Structures," *Journal of Astronautical Sciences*, Vol. 27, No. 2, 1979, pp. 157 - 180.

114. Balas, M. J., "Direct Velocity Feedback Control of Large Space Structures," *Journal of Guidance and Control*, Vol. 2, No. 3, 1979, pp. 252 - 253.

115. Meirovitch, L., *Elements of Vibration Analysis*, McGraw-Hill, Inc., New York, 1986.

116. Levine, W. S. and Athens, M., "On the Determination of the Optimal Constant Output Feedback Gains for Linear Multivariable Systems," *IEEE Transactions on Automatic Control*, Vol. AC-15, No. 1, February, 1979, pp. 44-48.

117. Ha, S. K., Keilers, C. and Chang, F., "Finite Element Analysis of Composite Structures Containing Distributed Piezoceramic Sensors and Actuators," *AIAA Journal*, Vol. 30, No. 3, March, 1992, pp. 772-780.

APPENDIX A - MODEL DATA

Table A.1 - Example Wings

	Steel Plate	G/E Wing
Area (in^2)	4204.8	40320
Taper Ratio	1	.333
Aspect Ratio	5	3
Fuselage Weight (lb)	_	18000
Fuselage Pitch Inertia ($lb\text{-}in\text{-}sec^2$)	_	5.0e7
Ply Layup (deg. AFT of midchord)	_	$[0/+45/-45/0]_S$
Material	S	$[GE/GE/GE/C]_S$
Layer 1 Thickness (in)		
Root	.25	.05
Tip	.25	.03
Layer 2 Thickness (in)		
Root	-	.05
Tip	-	.03
Layer 3 Thickness (in)		
Root	-	.05
Tip	-	.03
Layer 4 Thickness (in)		
Root	-	2.5
Tip	-	1.0

Table A.2 - Material Properties

	Steel (S)	Graphite/Epoxy (GE)	Core (C)
E_1 (psi)	3.0e7	2.1e7	100
E_2 (psi)	3.0e7	1.7e6	100
ν_{12}	.3	.017	.3
ν_{21}	.3	.210	.3
G_{13} (psi)	1.15e7	6.5e5	30
G_{23} (psi)	1.15e7	6.5e5	30
G_{12} (psi)	1.15e7	6.5e5	30
ρ ($lb\text{-}in^{-3}$)	.283	.054	.00116

APPENDIX B

PIEZOELECTRIC MATERIAL PROPERTIES

Table B.1 - Test Wing Piezo Patch Locations*

Patch #	x_1	y_1	x_2	y_2
1	10.0"	20.0"	15.0"	25.0"
2	25.0"	20.0"	30.0"	25.0"
3	10.0"	35.0"	15.0"	40.0"
4	25.0"	35.0"	30.0"	40.0"

* Refer to Figs. 2.6 & 5.4 for nomenclature

Table B.2 - Physical Properties of PZT G1195 Piezoceramic Patch*

Patch Thickness (in.)	
t_a	0.05
Piezoelectric Const. (in./Volt)	
$d_{31} = d_{32}$	7.51×10^{-9}
Young's Modulus (psi.)	
E	9.1×10^6
Poisson Ratio	
ν	0.3
Electrical Permittivity (Farad/in.)	
ξ_{33}^s	3.81×10^{-10}
Depoling Field (Volt/in.)	
E_{max}	15.2×10^3

* Taken from Ref. 117

APPENDIX C

SYMMETRY PROOF FOR $\overline{B}G\overline{C}$

The proof is provided for the case of a single input, single output (SISO) system, but it can be easily extended to multi-input, multi-output (MIMO) systems. We begin by defining piezoelectric actuator constant μ_a and sensor constant μ_s, as follows:

$$\begin{aligned} \mu_a &= z_c\left(d_{31}Q_{p_{11}} + d_{32}Q_{p_{12}}\right) = z_c\left(d_{31}Q_{p_{12}} + d_{32}Q_{p_{22}}\right) \\ \mu_s &= \frac{z_c}{C^S}\left(d_{31}Q_{p_{11}} + d_{32}Q_{p_{12}}\right) = \frac{z_c}{C^S}\left(d_{31}Q_{p_{12}} + d_{32}Q_{p_{22}}\right) \end{aligned} \tag{C.1a,b}$$

where z_c is the patch midplane height defined in Section 3.4 and the second term in each definition is an expression of patch isotropy. Inserting definition (C.1a) into Eq. (3.20) and considering the form of the actuator placement function (Eq. 2.17), we can rewrite the actuator participation submatrices (which are column vectors for the SISO case) as:

$$\hat{B}_4 = \mu_a \int_{y_1}^{y_2}\int_{x_1}^{x_2} \phi_{4,x}\, dxdy \equiv \mu_a \hat{I}_4\,,\ \hat{B}_5 = \mu_a \int_{y_1}^{y_2}\int_{x_1}^{x_2} \phi_{5,y}\, dxdy \equiv \mu_a \hat{I}_5 \tag{C.2a,b}$$

where ϕ_4 and ϕ_5 are the vectors of trial functions. Similarly, the sensor participation submatrices, Eqs. (3.30), are reduced to row vectors, which can be rewritten in the form:

$$\hat{C}_4 = \mu_s \int_{y_1}^{y_2}\int_{x_1}^{x_2} \phi_{4,x}^T\, dxdy \equiv \mu_s \hat{I}_4^T\,,\ \hat{C}_5 = \mu_s \int_{y_1}^{y_2}\int_{x_1}^{x_2} \phi_{5,y}^T\, dxdy \equiv \mu_s \hat{I}_5^T \tag{C.3a,b}$$

Now we can rewrite the actual participation matrices or their modal counterparts in the simplified form given by

$$\hat{B} = \mu_a \hat{I} \quad or \quad \overline{B} = \mu_a \Phi_f^T \hat{I} \quad , \hat{C} = \mu_s \hat{I}^T \quad or \quad \overline{C} = \mu_s \hat{I}^T \Phi_f \tag{C.4a,b}$$

where

$$\hat{I} = \begin{Bmatrix} 0 \\ \hline 0 \\ \hline 0 \\ \hline \hat{I}_4 \\ \hline \hat{I}_5 \end{Bmatrix} \tag{C.5}$$

Finally, to show symmetry, we have

$$\overline{B} G \overline{C} = \mu_a \mu_s \Phi_f^T \hat{I} G \hat{I}^T \Phi_f \tag{C.6}$$

and

$$\left[\overline{B} G \overline{C}\right]^T = \overline{C}^T G^T \overline{B}^T = \mu_a \mu_s \Phi_f^T \hat{I} G^T \hat{I}^T \Phi_f \tag{C.7}$$

Thus, the matrix $\overline{B} G \overline{C}$ is symmetric under the restriction that the output feedback gain matrix G is symmetric. For the SISO case, the gain matrix consists of a single scalar and this condition is automatically satisfied. As a result, output feedback of system displacement measurements does not destroy symmetry of the closed-loop stiffness matrix. *Q.E.D.*

VITA

The author was born to Bonnie J. and Wayne L. Morris on May 26, 1968 in New Castle, Pennsylvania. He received the Bachelor of Science degree in Aerospace Engineering from The Pennsylvania State University in May 1990, graduating "With High Distinction." His engineering experience includes two years of work towards an undergraduate thesis at The Applied Research Laboratory in State College, Pennsylvania, and one summer as a Graduate Research Fellow in the Vibrations and Acoustics branch of the Flight Dynamics Lab at Wright-Patterson Air Force Base in Dayton, Ohio. In August 1990 he continued his education at the Virginia Polytechnic Institute and State University, where he received the Master of Science degree in Engineering Mechanics in December 1992, with a Master's Thesis entitled *Optimal State Estimation for the Optimal Control of Far-Field Acoustic Radiation Pressure from Submerged Plates.* From January 1992 to the present, he has remained at Virginia Tech as a research assistant to Dr. Leonard Meirovitch, working towards the Doctor of Philosophy degree in Engineering Mechanics. During this time he has also enjoyed the opportunity to work with students, teaching sophomore level dynamics for a semester as well as leading supplementary help sessions for the same course during three semesters.

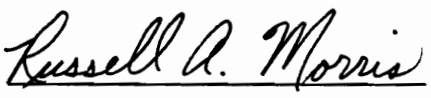

Russell A. Morris